UNIVERSITY OF SOUTHAMPTON

Unsteady Aerodynamics Using High-Order Methods

By

Prithiraj Bissessur

Doctor of Philosophy

SCHOOL OF ENGINEERING SCIENCES

February 2007

This Thesis has been completed as a requirement for a higher degree of the University of Southampton

To my family and
the memory of my
grandparents

UNIVERSITY OF SOUTHAMPTON

ABSTRACT

FACULTY OF ENGINEERING
SCHOOL OF ENGINEERING SCIENCES

Doctor of Philosophy

Unsteady Aerodynamics Using High-Order Methods

by Prithiraj Bissessur

Unsteady flows occur in many applications of engineering interest. One category of unsteady flows occur as self-sustaining oscillatory fluid motion, such as the flow over rectangular cavities. There has been a significant amount of research performed on this topic over the years, both experimentally and numerically. The unsteady flow over rectangular cavities is the case study in this research.

In this work, a generic numerical solver is developed and written to predict the near-field aerodynamics of unsteady fluid motions at low Mach numbers. High order numerical schemes are employed to this effect. The Detached Eddy Simulation (DES) method is considered for the turbulence modelling part. At the start of this project, the combination of high order Computational Aeroacoustics (CAA) numerical schemes, non-reflecting boundary conditions and DES constituted a state of the art approach to the simulation of unsteady compressible flow phenomena at low Mach numbers.

In the numerical study of 2D cavities, a number of cases with different length-to-depth (L/D) ratios were considered. Under the same flow conditions, the relation of the L/D to the radiated sound in the farfield is sought. It is found that the nature of the flow interaction with the downstream corner, which changes with L/D, dictates the directivity and amplitude of the sound field observed at a far distance from the source.

To gain more insight into the topology of 3D cavity flows, an experimental study using non-intrusive measurement techniques is outlined. This explains the work performed on 3D cavities with different spanwise dimensions. A detailed flow visualisation of the meanflow patterns in various measurements planes describes the presence of strong 3D features. In particular, the symmetrical flow behaviours at relatively large width-to-depth (W/D) ratios of 3 and 2 are highlighted. This provides the justification to employ a symmetry condition in the 3D DES study.

Therefore, the final case study is based on the numerical simulation of a 3D cavity geometry where only half of the cavity if simulated. The observations from the 2D simulations and the experimental work provided a basis of the expectations of this test case. Again, a correlation between the near-field aerodynamics and the farfield sound is sought. The 3D cavity showed (as in the 2D cases) a preferred directivity in the farfield.

Acknowledgements

I am grateful to my supervisor, Professor Xin Zhang for his patience and invaluable guidance during the course of this project.

I would also like to thank Dr. Xiaoxian Chen, Dr. Graham Ashcroft and Dr. Kenji Takeda for their help and assistance during the early stages of the project. Their contribution to the high order flow solver described in this work is gratefully acknowledged.

To Simon, whom as my office mate had to endure my musical taste. Thanks to Ajay, Mahbs, Shu and Abdul for making my time in Southampton truly memorable.

Special thanks to Miss Sonya Davy for having accommodated me for three years. I am grateful for her friendship and support during the course of my project.

Finally, thanks to my parents and my aunts, Tina and Bo, for their eternal belief in me and to Katarina for her support and understanding in the final stages of this work.

Contents

List of Tables

List of Figures

Nomenclature

a	Speed of sound
C_p	Pressure coefficient, $(p - p_\infty)/\frac{1}{2}\rho_\infty U_\infty^2$
c_p	Specific heat coefficient at constant pressure
c_v	Specific heat coefficient at constant volume
e	Specific internal energy
e_t	Specific total energy
f	Frequency
G	Generic Green's function
G_0	Free space Green's function
$H()$	Heaviside function
J	Jacobian
k	Specific turbulent kinetic energy
M	Mach number
p	Static pressure
Pr	Prandtl number
Pr_T	Turbulent Prandtl number
q_x, q_y, q_z	Heat flux in Cartesian coordinate system
R	Universal gas constant

Re	Reynolds number
St	Strouhal number
t	Time
T	Temperature, unless otherwise stated
T_{ij}	Lighthill stress tensor
u, v, w	Cartesian coordinate velocity components
u_i	Cartesian velocity components $(u_1, u_2, u_3) \equiv$(u,v,w)
U, V, W	Contravariant velocity components
L	Cavity length
D	Cavity depth
W	Cavity width or span
$\mathbf{v}$	Velocity vector

Greek Symbols:

α	Phase lag in the Rossiter equation
ρ	Fluid density
δ	Boundary layer thickness
δ_{ij}	Kronecker delta function
$\delta()$	Dirac delta function
δ^*	Displacement thickness
μ	Fluid molecular viscosity
ν	Kinematic viscosity, $\nu = \mu/\rho$
τ_w	Wall shear stress
τ_{ij}	Viscous stress tensor
ξ, η, ζ	Orthogonal curvilinear coordinate
ϕ	Generic field notation
θ	Momentum thickness

κ	Wavenumber
$\kappa_x, \kappa_y, \kappa_z$	Directional wavenumbers in Cartesian space
σ_i	Root-mean-square of the velocity fluctuation $u_i^{'}$
Π	LES filter function
$\underline{\Delta}$	Filter width

Superscripts:

$\overline{()}$	Time averaged quantity
$\widetilde{()}$	Favre averaged quantity
$()^*$	Dimensional quantity
$()'$	Fluctuation quantity
$\overline{\overline{()}}$	Filtered quantity

Subscripts:

$()_0$	Reference quantity
$()_\infty$	Free stream quantity
$()_t$	Total stagnation condition
$()_T$	Turbulent quantity

Symbols:

<>	Time averaged quantity

Abbreviations:

CAA	Computational AeroAcoustics
CFD	Computational Fluid Dynamics
CFL	Courant-Friedrichs-Levy criterion (or Courant number)
DFT	Discrete Fourier Transform
DRP	Dispersion Relation Preserving
SPL	Sound Pressure Level, decibels (dB)
MPI	Message Passing Interface
FW-H	Ffwocs Williams and Hawkings
FFT	Fast Fourier Transform
PIV	Particle Image Velocimetry
POD	Proper Orthogonal Decomposition
DNS	Direct Numerical Simulation
DES	Detached Eddy Simulation
LES	Large Eddy Simulation
RANS	Reynolds Averaged Navier-Stokes
CCD	Charged Coupled Device
2D	Two-dimensional
3D	Three-dimensional
RK	Runge-Kutta
LDDRK	Low Dispersion and Dissipation Runge-Kutta
S-A	Spalart-Allmaras One Equation Turbulence Model

Chapter 1

Introduction

1.1 Motivation

Cavity noise appears in large number of applications where a cutout of some description is subjected to an oncoming flow. When the conditions are right, self-sustained oscillations can occur inside the cavity where undesirable effects such as vibrations (fluid-structure interaction), noise generation, increase in drag and a change in the thermal transfer characteristics can arise.

The presence of a cavity creates large fluctuations in pressure, density or velocity, thereby giving rise to an intense acoustic radiation. The first experimental investigations into cavity flows were in the years $1950 - 1960$ [1, 2]. These were primarily dedicated to military aircraft with bomb bays, which, when open resembled rectangular cavities. The cavities thus studied were of large physical dimension and the flow speeds were in the high subsonic or supersonic regimes. In the $1970's$ there was an apparent need to consider lower flow speeds where it was identified that aircraft landing gear wheel wells during take-off and landing were similar, in generic terms, to rectangular cavities [2, 3].

The range of applications extends to flows that incur large amplitude oscillations in reso-

nant systems such as the multi-stage compressor arrangement in the combustion chamber of jet engines. The resonance mechanism here is a function of geometric parameters and can be classed as a Helmholtz resonator [4, 5].

In non-aeronautical applications, cavities are also present, i.e. rail wagons (where the gap between carriages form a rather large cavity) and door cavities in the automobile applications. The aeroacoustic oscillations created in such applications can be a significant detriment to the comfort of passengers as well as a nuisance to the surrounding environment. The variety of applications and the complexity of the phenomena involved have inspired quite a number of experimental, theoretical and more recently computational investigation into cavity flow physics. Most research tends to focus on the flow characteristics and acoustics. However, recently a new trend has been set into devising methods for the active or passive control of cavity noise [6, 7, 8]. In the following sections, the terminologies associated with cavity flows are explained and the relevant experimental, theoretical and computational work over the years is reviewed.

1.2 Cavity Terminology

A generic rectangular cavity can be characterised by its length L, depth D and span W. These notations are shown in Figure 1.1, where a 2D cavity is represented. While the geometry is simple as shown in Figure 1.1, the underlying physics of the flow over such arrangements is complex. Cavity flows have been observed to exhibit flow phenomena rich in unsteady fluid dynamics, flow-acoustic interaction and flow-acoustic resonance. It is no trivial task to classify the flow regimes that can be observed over cavities. The important parameters that can influence the flow regime observed are the inflow speed U_∞, the incoming boundary layer momentum thickness θ, the ambient fluid parameters such as the air density ρ_∞, the ambient speed of sound a_∞ and the basic geometric parameters of the cavity, L, D and W.

A first classification of the cavity flow problem is formed using basic geometric param-

eters. The ratios length to the depth and the length to width of the cavity are therefore critical. Roshko [9] observed that the L/D has a strong influence over the nature of the flow. Four basic types of cavity flow regimes observed in experimental studies [10, 11] are the open, closed, transitional-open and transitional closed. In the open flow regime as shown in Figure 1.3(a), the shear layer across the cavity opening bridges the leading and trailing edge corners. The flow is dominated by a main large-scale re-circulating structure within the cavity. The static pressure distribution is characterised by a single minimum corresponding to the centre of the flow recirculation. This type of flow regime is generally observed for cavities of $L/D \leq 6$ up to a maximum of $L/D \leq 8$ at subsonic and transonic speeds. The second type of cavity flow is the closed flow regime which concerns cavities termed as 'shallow'. This characteristics of this flow regime is shown in Figure 1.4(a). In this case the shear layer re-attaches somewhere along the cavity floor and separates again as the flow passes the trailing edge corner. Two distinct re-circulating zones are observed, one upstream and the other downstream of the re-attachment and separation zone on the cavity floor. The static pressure along the cavity floor in this case is characterised by a strong adverse pressure gradient as shown in Figure 1.4(a). The occurrence of this flow regime is largely influenced by the flow Mach number. For subsonic and transonic speeds, this flow regime can be observed for L/D values between 9 and 15. At supersonic speeds, the closed flow regime is observed for $L/D \geq 13$. The flow regime that falls between open and closed is termed transitional. Figure 1.3(b) shows the characteristic transitional-open cavity flow. The static pressure distribution along the floor is mainly uniform in the forward portion but increases towards the aft portion of the cavity. The fourth cavity flow regime is the transitional-closed flow shown in Figure 1.4(b). In this case, the static pressure experiences a continuous increase over most of the floor. Another important geometrical parameter is the ratio of length-to-width which defines 3D cavities. For $L/W \leq 1$, the shear layer has been found to exhibit more or less a 2D behaviour, whereas for $L/W > 1$, three dimensional effects come into play as shown by Maull and East [12]. Thus for relatively shallow cavities of $L/D \geq 4$ and $L/W > 1$, 3D effects were observed at low speeds [12].

The type of flow regime largely influences the nature of the unsteady flow in and around the cavity. Closed cavity flows often display broadband pressure fluctuations whereas open cavity flows are typified by highly periodic flow phenomena. To determine the influence of the cavity depth on the flow characteristics one must consider the ratio D/δ_0, where δ_0 is the thickness of the oncoming boundary layer. Below a certain value of D/δ_0 the frequency of the oscillations is minimised. On the other hand, as shown by Kuo *et al* [13], the re-circulation region inside the cavity can modulate the path and behaviour of the shear layer. The transition from an open cavity to a closed cavity depends on the flow Mach number as shown by Tracy and Plentovich [14]. Sarohia [15] defined a non-dimensional length, $(L/\delta_0)\sqrt{Re_{\delta_0}}$, where L is the length of the cavity and Re_{δ_0} is the Reynolds number based on the boundary layer thickness. For laminar flow over a cavity, this non-dimensional length is independent of the normalised depth D/δ_0 for $D/\delta_0 \geq 2$. It is also found that if the non-dimensional minimum length is below a value of 0.29×10^3 no cavity oscillation occurs [15].

The nature of the oscillations that may develop in an open cavity flow regime is dependent on the value of L/D. For cavities where L/D are small, transverse standing waves are present and the such cavities are classed as 'deep'. For values L/D which are sufficiently large, longitudinal standing waves are observed and such cavities are termed as 'shallow'. Generally, cavities are classed as 'deep' when $L/D < 1$ and classed as 'shallow' when $L/D > 1$. Therefore, a second classification of the cavity flow problem is based on the characteristics of the oscillations which occur. For this purpose, three distinct classes of interactions between the flow and the cavity have been identified:

- Dynamic (hydrodynamic or aerodynamic)
- Resonant (acoustic)
- Elastic (fluid-structure)

Dynamic interaction comes from the instability waves developing in the shear layer which get amplified by a feedback mechanism. The acoustic resonance is the type of mechanism

associated with the compressibility of the of the fluid (standing waves inside the cavity and Helmholtz type resonator). The elastic interaction is a fluid-structure interaction and has to do with the elastic deformation of solid surfaces. The current study is limited in scope to the dynamic and acoustic phenomena only.

1.3 Review of Experimental and Theoretical Work

The experimental work of Roshko [9] and that of Karamcheti [16] in 1955 constituted the first substantial investigation into cavity flow physics and the subsequent noise radiation. In particular, Roshko highlighted the importance of the geometrical parameters on the meanflow. For shallow cavities at low Mach numbers, a main vortical region with secondary re-circulating regions in the corner (Moffatt eddies) is observed. The main conclusion from this study is that the drag on the cavity is directly related to the stagnation pressure occurring on the downstream wall when the shear layer impinges on it.

On the other hand, the work carried out by Karamcheti was the first attempt to consider the radiated noise and remains to this day as one of the rare references where the influence of the meanflow on the sound field is clearly illustrated. It was noted that the directivity of the radiation was towards the leading edge for high Mach numbers. The primary reason for this is due to the convection of the acoustic waves by the meanflow. In his study, the influence of the nature (laminar or turbulent) of the oncoming boundary layer was also investigated. It was observed that the peaks in the spectra of the pressure fluctuations were more intense when the incident boundary layer was laminar and more broadband for a turbulent one.

Plumblee *et al* [17] investigated the acoustic resonance phenomenon. The authors showed that when a deep cavity was excited by an oncoming freestream, the acoustic resonance modes were those corresponding to the depth modes. For shallow cavities the predominant modes came from the longitudinal modes. The authors also postulated that the turbulent fluctuations that are of a broadband nature constitute the primary excitation mech-

anism of the acoustic modes related to the cavity geometry. However, this observation contradicts the observation that for the laminar case, the acoustic field is more intense.

In 1963, Maull and East [12], performed an experimental investigation to demonstrate the 3D nature of the flow inside the cavity. Cellular re-circulating structures were observed for certain spanwise length W of the cavity. The existence of these structures and an odd or even number of cells is directly related to the size of the primary vortex in the streamwise direction. The cellular structures are visible at low speeds but can also appear at high speeds. It was concluded that 3D effects can also play an important of role on the oscillations and hence the acoustic field.

In 1964, Rossiter [18] studied cavity flows in the L/D range from 1 to 10 and at Mach numbers ranging from 0.4 to 1.2. This study provided the first satisfactory explanation of the aerodynamic coupling that produces self-sustained oscillations. It was concluded that the periodic pressure fluctuations might be attributed to an acoustic resonance within the cavity and is very similar to the 'edge-tone' excitation. Rossiter observed large-scale vortical structures in the shear layer that span the cavity opening. For a cavity of length L, the convection velocity of the large scale vortical structure is U_c and thus the convective time scale is L/U_c. In a free shear layer, the convection speed is anywhere between $0.4U_c$ to $0.6U_c$. With this information, a plot of Strouhal number ($St = fL/U_\infty$), where f is the periodic shedding frequency, against Mach number (M) gives a direct empirical formula which relates St, M and n (the integer number of large scale vortical structures in the shear layer). When a vortex impinges on the aft cavity wall, acoustic waves are generated and propagate upstream of the cavity and reach the leading edge in time L/a_0, where a_0 is the speed of sound inside the enclosure which, at low Mach numbers, can be assumed equal to the freestream sound speed a_∞. The amplitude of the periodic shedding gets amplified by this process.

$$\frac{n}{f} = \frac{L}{U_c} + \frac{L}{a_\infty} \tag{1.1}$$

L/D	α
4	0.25
6	0.38
8	0.54
10	0.58

Table 1.1: α for various L/D.

Rearranging equation (1.1) gives

$$St = \frac{fL}{U_\infty} = \frac{n}{\frac{U_\infty}{U_c} + M_\infty} \tag{1.2}$$

When the impingement of the vortical structure occurs, there is a phase lag between the the emission of acoustic waves. Similarly, there is a phase lag between the arrival of a pressure wave at the leading edge and the roll-up of a new vortex. Thus equation (1.2) is re-written as,

$$St = \frac{fL}{U_\infty} = \frac{n - \alpha}{\frac{1}{\kappa} + M_\infty} \tag{1.3}$$

Where α is the phase lag and κ is the ratio of the freestream velocity to the mean convection velocity. Usually, α is taken as 0.25. Table 1.1 gives values of α for a range of L/D from 4 to 10.

Although the Rossiter formula, equation (1.3), is a popular model for predicting cavity oscillations, it does not take into account the characteristics of the oncoming boundary layer, the acoustic resonance modes and the influence of the cavity depth D, all of which can significantly modify the properties of the flow if self-sustained oscillations occur and implicitly infers that the feedback mechanism is of an acoustic nature.

Another investigation by East (1966) [19] explored the response of deep cavities and showed that the shear layer oscillations can be the result of two distinct mechanisms: a feedback system as described by Rossiter and another due to the resonant acoustic modes

as described by Plumblee *et al* [17]. At high Mach numbers, the aeroacoustic feedback predominates and the Rossiter formula is applicable but at low Mach numbers, the two mechanisms co-exist. When the fundamental frequencies of the acoustic modes and the oscillation modes coincide, a double resonance effect is produced that amplifies the amplitude of the shear layer oscillation.

Heller *et al* [20] accounted for the local variation of the speed of sound in the cavity and extended the Rossiter results to high Mach numbers above Mach 1.2. At such speeds, the speed of sound inside the cavity can no longer be taken as equal to the freestream value but is determined by the local static temperature, thus

$$\frac{a_{cavity}}{a_\infty} = \sqrt{1 + r\frac{\gamma - 1}{2}M_\infty^2} \tag{1.4}$$

where r is the thermal recovery factor

$$r = \frac{T_c - T_\infty}{T_0 - T_\infty} \tag{1.5}$$

where T_c is the temperature in the cavity and T_0 is the stagnation temperature. At high Mach numbers, $r \simeq 1$. Substituting equation (1.4) into the Rossiter formula (1.3) gives,

$$St = \frac{fL}{U_\infty} = \frac{n - \alpha}{\frac{1}{\kappa} + \frac{M_\infty}{\sqrt{1 + r\frac{\gamma-1}{2}M_\infty^2}}} \tag{1.6}$$

Bilanin and Covert [21] modelled analytically the shear layer spanning the cavity opening as a vortex sheet. Their model gives an analytical expression for the two semi-empirical constants in the Rossiter formulation but unfortunately the frequencies were poorly predicted. The poor predictive performance of the model arises from the fact that the shear layer is assumed to be an infinitely thin vortex sheet. Tam and Block [22] included the effects of the oncoming boundary layer thickness in their analysis. The introduction of

parameters such as L/D and the non dimensional length as defined by Sarohia [15] enabled them to improve on the Bilanin and Covert model. The Tam and Block model takes into account the aeroacoustic coupling but cannot predict the acoustic depth modes that occur at low speeds.

On the other hand, Heller and Bliss [23] consider the fluid injection and ejection at the trailing edge corner of the cavity as the primary effect to the resulting oscillations. In their study, the downstream edge was substituted by a pseudo-piston. The mass addition and removal creates pressure fluctuations that travel upstream in the cavity and thereby further amplify the vortices that are shed at the leading corner. In this manner the cavity acoustic wave generated is coupled with the motion of the shear layer and thus completing the feedback loop.

In 1987, Gharib and Roshko [24] conducted an experimental investigation into an axisymmetric cavity flow where the transition of the shear layer oscillation modes to a new regime was found. Under the condition that the oncoming boundary layer was thin, the shear layer resembled the wake pattern behind a bluff body. This regime was appropriately termed a 'wake-mode' type oscillation. In this case the cavity flow undergoes alternating filling and emptying phases in a manner that is indicative of an absolute instability as shown by Theofilis *et al* [25]. This gives a large increase in the drag of the cavity and is mainly observed for shallow cavities. Deep cavities tend to behave in a more quiescent fashion and this type of oscillation is termed the 'shear-layer' mode regime, i.e. the Rossiter modes.

In a series of experiments by Plentovich [26, 11] and Tracy and Plentovich [14, 27], detailed static pressure data have been compiled for 3D cavities at subsonic and transonic speeds and high Reynolds numbers in order to characterise the flow field. The cavity L/D ratio ranges from 4.4 to 20.0 in the experiments and W/D between 1.0 and 4.5. A wide range of flow speeds have been investigated, and the flow Reynolds number varied from 1.0×10^6 to 1.0×10^8. Both static coefficients of pressure as well as the fluctuating sound pressure levels inside the cavity were measured.

In 1996, Ahuja and Mendoza [28] delivered a comprehensive database on the influence of various parameters such as L/D, L/W, the oncoming boundary layer properties and temperature effects on the oscillations occurring in the cavity. This study is one of the rare cases where there is an attempt to relate the far-field directivity to the near-field flow physics (near-field pressure fluctuations). Also, to characterise the 3D effects, the authors studied the effect of varying the cavity span W. For $L/W < 1$, the behaviour of the radiated noise was found to be that of a 2D cavity.

Particle Image Velocimetry (PIV) investigations enabled the near-instantaneous velocity field of cavity flows to be recorded. PIV measurements of the turbulent flow over a cavity were carried out by Lin and Rockwell [29]. Kuo *et al* [13] recently used the same technique to study the effect of modifying the base of the cavity (i.e. replacing the floor with a slope) on the flow.

1.4 Dynamic Oscillations and the Feedback Mechanism

Since the edge-tone phenomenon was observed by Sondhaus in 1854, self-sustained oscillations have been noted for a large number of flows where the shear layer strikes an obstacle. Rockwell and Naudascher [30] have compiled a comprehensive collection from the literature on these types of flows.

Self-sustained oscillations occur in the presence of a chain of events that are the necessary conditions for the flow instability to self-sustain,

- The feedback process takes place when perturbations at the cavity trailing edge due to the impingement of the large scale vortical structures are propagated upstream to the leading edge corner. This region of the flow is particularly sensitive to disturbances as the boundary layer separates there (receptivity process).
- Fluctuations of vorticity occur in the shear layer close to the separation point.

- These perturbations convectively amplify across the cavity mouth.
- New perturbations at the downstream cavity edge are formed by the impingement of the shear layer fluctuations against the solid boundary. These perturbations travel upstream thus closing the feedback loop.

Experimental investigations into cavity flows under varying conditions have shown that the disturbances that propagate upstream are either acoustic or aerodynamic in nature. At high speeds, when the characteristic acoustic wavelength λ is of the same order as the length scale, L, it is important to take into account the speed of sound to determine the retarded time between the impact zone and the separation zone. Powell [31] showed that there is an acoustic radiation towards the upstream region and suggested that simple acoustic sources be used to model the acoustic feedback. For flows at very low Mach numbers, the feedback process is instantaneous and occurs in the vicinity of the acoustic source. The feedback process is essentially of an aerodynamic nature. However, there is always an influence of the coherent vortical structures on the upstream flow. This has also been observed in flow without obstacles at both low and high Mach numbers. The question thus arising is to what extent an obstacle modifies the arrangement of the coherent structures of the flow to lead to a feedback process. In the cavity case, the distribution of coherent structures is of a deterministic nature due to the fact that there is more or less a constant phase lag between the shedding of a new vortex and the impingement of another on the aft wall.

It is useful to examine the cavity feedback process using elementary control theory. With reference to Figure 1.2, let $u_i(s)$ be the random fluctuation of the oncoming boundary layer at the cavity leading edge. This fluctuation is selectively amplified with convection in the shear layer, so that at the downstream cavity edge the fluctuation has grown into $u_o(s)$. This process is represented by $H(s)$ in Figure 1.2. The impingement of $u_o(s)$ on the downstream cavity edge creates a feedback pressure $p(s)$ that travels upstream. The generation of the pressure wave is represented by $p(s)$ in Figure 1.2. As the pressure wave crosses the upstream shear layer, it excites a velocity disturbance $u_d(s)$ due to the shear

layer receptivity $R(s)$. The disturbance $u_d(s)$ adds to any $u_i(s)$ thus closing the feedback loop.

As identified by Rossiter [18], the necessary condition for a limit cycle to self-sustain is that $H(s)$ x $p(s)$ x $R(s) = 1$. Recently Rowley *et al* [32] suggested that certain cavity flow oscillations occur not as self-sustained instabilities but as lightly damped oscillations. These require a constant input $u_i(s)$ from the turbulent structures in the oncoming boundary layer.

1.4.1 Vorticity fluctuations

The conversion of pressure fluctuations reaching the separation point into vorticity has been studied by Morkovin and Paranjape [33]. It was found that the transverse pressure gradient plays an important role in this conversion process (receptivity). Moreover, the authors suggested that the periodic motion of the disturbances enables the conversion of an essentially irrotational disturbance field (pressure fluctuations) to a rotational disturbance field (vorticity fluctuations). Linear stability analysis of nearly parallel flows can thus be adapted to account for the thickening of the shear layer. The frequency of the self-sustained oscillations lies in the region where the growth rate of these disturbances across the mouth of the cavity is positive.

1.4.2 Creation of disturbances at the aft corner

Where the large scale vortical structures impinge on the rear cavity edge, their deformation creates fluctuating forces on the downstream edge. Rockwell and Knisely [34] identified three ways in which these structures strike the trailing edge wall:

- Complete destruction, where there is a total breakdown of the large eddies.
- Partial destruction, where upon impact, the large vortices form smaller eddies which

spill inwards and outwards.

- The large scale vortices simply go around the corner and out of the cavity

For thin and turbulent oncoming boundary layers, none of these three types of deformation is predominant and there is more or less a random combination of these events. These are probably at the source of high and low frequencies in the sound power spectrum. The main re-circulation region can also modify the shear layer trajectory and determine where it strikes the aft wall, as shown by Kuo *et al* [13]. This effect is neglected in all the models relating to cavity flow oscillations and could potentially explain the variable way in which the shear layer interacts with the aft wall. All three types of deformation mentioned can be the source of the pressure fluctuations that subsequently travel upstream to further excite the shear layer and self-sustain the cavity flow instability.

1.5 Review of Computational Work

The first Computational Fluid Dynamics (CFD) simulations on cavity flows were performed by Hankey and Shang [35]. They used the Cebeci-Smith RANS model with the McCormack scheme on a 2D cavity of $L/D = 2.25$ at Mach 1.5. The simulations compared favourably to the observations by Heller and Bliss [23]. Cavity flow simulations using RANS methods became popular in the 1990's and were mostly validated with surface pressure distributions around the cavity walls. Tam *et al* [36] studied the influence of the turbulence models and showed that the results were sensitive to the model used due to inherent dissipative nature of most models. This was confirmed by Slimon *et al* [37]. The predictive ability of the RANS approach on a self-sustained cavity flow problem is severely limited by the inability of the turbulence model to reproduce the significant effects that the instability loop has on the mean flow, such as the non-linear shear layer time-mean growth rate and the time-mean recirculation flow pattern in the enclosure. This turned the direction of the CFD community towards time-resolved methods for cavity flows.

The first 3D computations were performed by Rizetta [38] using an unsteady RANS approach with the Baldwin-Lomax turbulence model. The advantage of RANS turbulence closure methods is that they are relatively easy to add to most CFD codes and provide a means to study the effect of varying the cavity geometry on the flow behaviour (passive control). Kim [39] replaced the cavity floor by a porous wall and obtained the same trends as observed in the corresponding experiments. Baysal [40] replaced the trailing edge corner by a ramp and Zhang *et al* [41] modified the geometry at the leading edge. Sinha *et al* [42, 43] used the $k-\varepsilon$ model and a one equations Large Eddy Simulation (LES) approach with wall functions to perform 3D unsteady simulations. Soemarwoto *et al* [44] used a $k-\omega$ turbulence model to compute the flow over a 3D cavity of $L/D = 4.5$ at a Mach number of 1.2. The aim was to study the effect of replacing the trailing edge corner by a 45 degree ramp.

Direct Numerical Simulations (DNS) of cavity flows have also been tackled, for instance the calculation performed by Kestens [45] at low Reynolds numbers on 2D cavities for the study of open or closed flow oscillation control. A 3D simulation on a deep cavity of $L/D = 0.42$ and $L/W = 2$ at a Mach number of 0.8 was performed by Sagaut [46]. This simulation was at a low Reynolds number but was adequate to show 3D effects.

1.5.1 Supersonic simulations

The acoustic radiation arising from the supersonic flow over a cavity consists of a family of unsteady shock waves as described by Heller and Delfs [47]. Given the intensity of the shock waves, a conventional second-order accurate CFD simulation is sufficient to obtain the radiated pressure field. Moreover, these pressure waves cannot travel upstream of the flow. Numerous compressible unsteady RANS simulations have given a radiated sound field as those visualised experimentally. For example, Zhang *et al* [48, 49, 50, 51] have used an unsteady RANS method with a modified $k-\omega$ model to take into account compressibility effects. The numerical results are in good agreement (at Mach numbers of 1.5 and 2.5) with their own experiments [41]. Rona and Dieudonné [52] computed a

laminar 2D cavity ($L/D = 3$) flow at Mach 1.5. In an attempt to investigate the cavity flow instability, the authors concluded that the dominant cavity oscillation mode, which characterises the flow instability, is of a flow-resonant nature. In another study, Rona and Brooksbank [53] performed a POD analysis of the turbulent flow over a 2D cavity of $L/D = 3$ at Mach 1.5. In this study a simple low order model representing the cavity flow instability was developed. The control of such flow instabilities was thus studied numerically by Rona [54]. In this study, blowing was applied at the cavity leading edge. The unsteadiness of the pressure field was reduced and subsequently disrupted the formation of the feedback loop.

1.5.2 Subsonic simulations

The first 2D laminar simulations in the subsonic regime leading to the radiated acoustic field were performed by Colonius [55] and Shieh and Morris [56] in 1999 for Reynolds numbers based on the depth D ($Re_D \simeq 5000$). These are in effect DNS computations (no turbulence model) using Computational Aeroacoustics (CAA) algorithms and non-reflecting boundary conditions. In the study by Colonius *et al* [57, 55], a transition in the flow regime is depicted, notably, there is a change from the classical Rossiter oscillation modes (shear layer mode) to the wake mode regime. This confirmed the observations by Gharib and Roshko [24] for shallow cavities with thin oncoming boundary layers. Shieh and Morris [58] applied the developments in CAA to the unsteady RANS methodology for high Reynolds ($Re_D \simeq 10 \times 10^5$) number simulations. In this study the Spalart-Allmaras one-equation turbulence model was hybridised to give a coupled RANS/LES technique called Detached Eddy Simulation (DES) for accurately resolving the separation regions in the flow. The transition from the shear layer mode to the wake mode is still observed. Ashcroft *et al* [59, 60] used and unsteady RANS method with the $k-\omega$ model for a door cavity problem and the results were in good agreement with the measurements taken by Henderson [61].

In 2002, Gloerfelt *et al* [62] performed 2D and 3D LES computations over cavities of

various geometries. In shallow cavities, the transition to the wake mode is still observed and in the highly 3D case ($L/W > 1$), the oscillations were observed to be quite random thus showing that the coherence of the self-sustained oscillations is somewhat affected in the 3D case. For cavities of larger span W, the self-sustained oscillations had a nearly 2D behaviour.

The LES computation for the compressible flow over a deep cavity was performed by Larchevêque *et al* [63]. An accurate prediction of the peak levels of the fundamental frequency and its first harmonics was achieved relative to the available experimental data. In another study by Larchevêque *et al* [64], the simulation of the flow over weapons bays was performed. This study highlighted the existence of both transverse strong acoustic modes and vortical structures. The approach employed by these authors highlights a trend in the use of LES for the numerical simulation of flow over cavities.

1.6 Objectives and Scope of the Present Study

The present study is part of on-going research to further the current understanding into cavity flow oscillations. The aerodynamics of the flow is complex and, although quite a few theoretical and experimental as well as numerical studies have been performed, the analysis is yet to be completed.

The state-of-the-art when the author undertook this research was a lack of understanding of broadband cavity noise. Therefore the objective of the author's research was to understand the basic physics of the broadband cavity noise generation mechanism and to accurately predict the sound pressure levels of the flow-induced cavity noise with the use of CFD/CAA methodologies. In this approach, CFD simulations were used to predict the unsteady flow field and the acoustic radiation simultaneously. The direct computation of the sound field implies that there are no heuristic assumptions in the acoustic model. Algorithms involving low dispersion and dissipation errors are used to maintain accuracy. Boundary conditions are critical such that they must not allow physical and numerical

reflections back into the computational domain. In addition to the computational work, wind tunnel testing using PIV was used to observe and record the flow patterns in 3D cavities of varying L/W. An experimental database was assembled that can be used for the purpose of validating numerical work as well as to provide the cavity research community with a comprehensive set of data.

1.7 Structure of the Thesis

This thesis comprises of three parts. Part 1 spans Chapters 1 to 3 and constitutes the introductory chapters. In Chapter 1, a literature review is outlined. Chapter 2 provides an overview of the mathematical and numerical models employed in the present work. In Chapter 2 the governing equations are outlined and the numerical implementation is discussed both in terms of the spatial and temporal discretisation requirements. Boundary conditions, namely, non-reflecting buffer zone type inflow/outflow conditions are highlighted. In Chapter 3, a mesh sensitivity study is performed on a 2D cavity case. This Chapter focuses mainly on the aerodynamic flow field and the results from two simulations are presented.

Part 2 focuses on 2D cavity flows and comprises of Chapter 4 alone. The aerodynamic and acoustic field of 2D cavities of various L/D are examined. The results from the simulations are presented separately for the aerodynamic and the acoustic analyses, where the latter is obtained from the FW-H integral method.

With the increase in computing power and enhanced numerical methods, more sophisticated and larger computations have been performed [64]. However, at the start of the current study, the effort represented the first attempt involving both near-field and far-field computation using high order schemes. In the studies by Shieh and Morris [56, 58], 2D DES calculations were performed to resolve the near-field flow. The far-field acoustic analysis was not undertaken. Therefore, in this study, the far-field radiation pattern is investigated in relation to the flow over 2D cavities.

Part 3 examines 3D cavity flows using experimental and computational methods. This analysis spans Chapters 5 and 6. In Chapter 5 low speed 3D cavity flows of W/D ratios of 3, 2, 1.5, 1 and 0.5 are investigated using PIV and oil flow visualisation. In Chapter 6, the numerical investigation of a 3D cavity is presented. The geometry and flow conditions in this case are not part of the experimental database. It is nonetheless a useful analysis as it relates to the compressible subsonic flow over a 3D rectangular cavity. The resulting aerodynamic field is presented and the acoustic field is analysed using the FW-H integral method.

1.8 Chapter 1 Figures

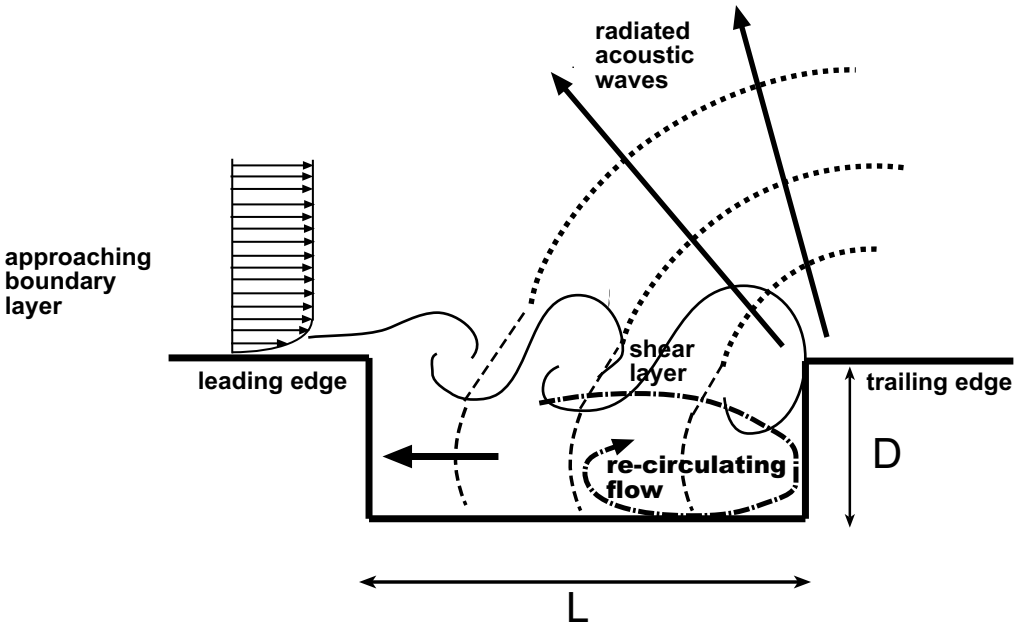

Figure 1.1: Schematic of flow over a cavity.

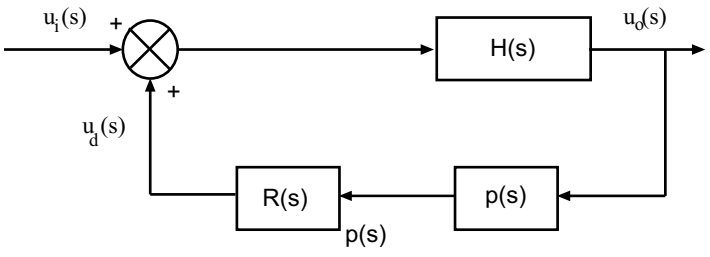

Figure 1.2: Schematic of cavity flow feedback loop.

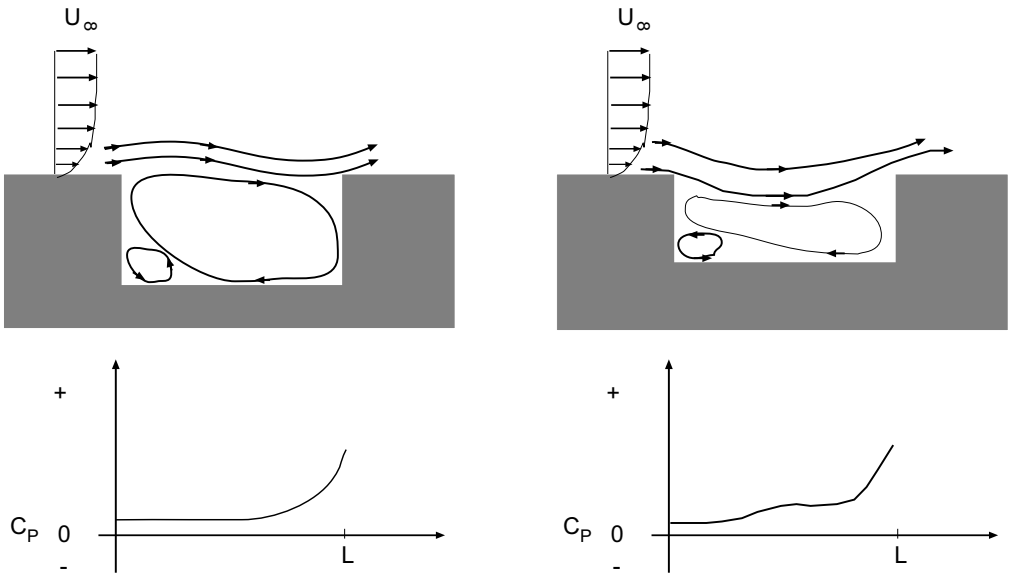

(a) Open cavity (b) Transitional-open cavity

Figure 1.3: Schematic of flow over an open and transitional-open cavity and pressure distribution along the floor.

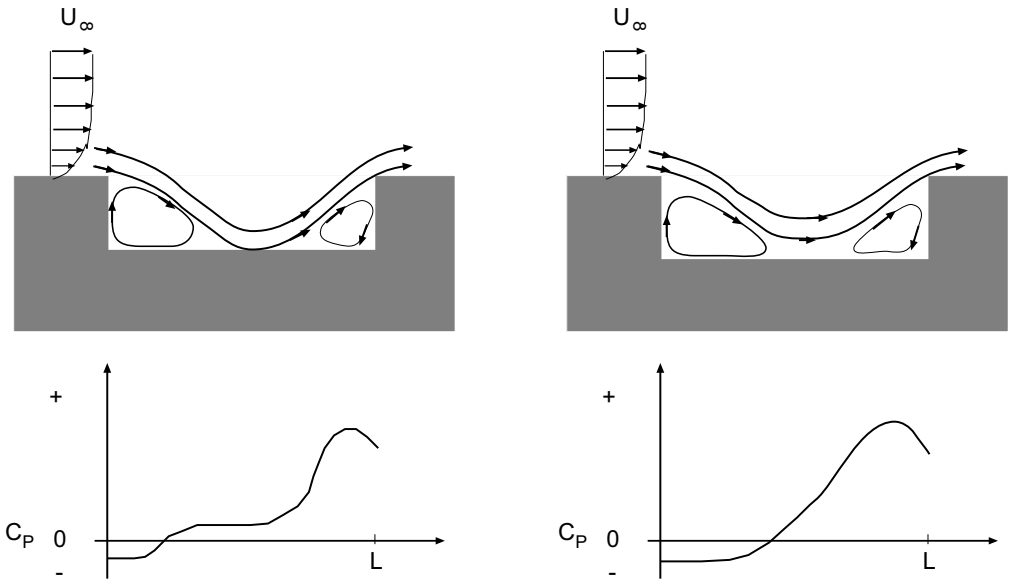

(a) Closed cavity (b) Closed-transitional cavity

Figure 1.4: Schematic of flow over an closed and transitional-closed cavity and pressure distribution along the floor.

Chapter 2

Mathematical and Numerical Models

2.1 Introduction

This chapter describes the numerical methods employed in the current research. The choice of spatial and temporal discretisation will be described in details. Boundary conditions are especially important as the solution must not be allowed to be spoiled due to spurious reflections within the computational domain.

2.2 Modelling Approach

The aim of the computational work in this research is to study the noise generation due to unsteady flows at low Mach numbers. The Navier-Stokes equations for a compressible fluid are presented in Appendix A. The emphasis is on unsteady separated flows. To this end, the Detached Eddy Simulation (DES) approach has been implemented as part of the research work. The work involves a two-stage approach of computing the noise from a subsonic rectangular cavity flow. Firstly, the use of a high order solver coupled with the DES method allows a direct computation of the sound generation in the near-field. In the second stage, the far-field noise directivity is evaluated using the Ffowcs Williams

and Hawkings (FW-H) acoustic analogy [65, 66]. Since the work in this research did not involve the development of the FW-H solver, this chapter is limited to the description of the near-field methodology.

2.3 Governing Equations - Generalized Coordinate System

The flow variables (u, v, w, p, e_t) in equation (A.1) are given in terms of variations with respect to a Cartesian frame of reference. To proceed to a numerical solution of the Navier-Stokes equations a set of orthogonal curviliear coordinates system is introduced, represented as (ξ, η, ζ, t), corresponding to (x, y, z, t) respectively. This type of representation is usually referred to as body-fitted coordinates. This is a common practice in CFD when dealing with complex geometries. The governing equations (A.1) are recast to a rectangular uniform grid in the computational domain which is easier to handle when dealing with finite differences. The grid spacing in all directions is unity and the Jacobian of transformation relates the geometrical properties of the physical space to the computational space.

$$\xi = \xi(x, y, z, t) \tag{2.1}$$

$$\eta = \eta(x, y, z, t) \tag{2.2}$$

$$\zeta = \zeta(x, y, z, t) \tag{2.3}$$

The derivatives in (A.1) are transformed using the chain rule and it follows that:

$$\begin{aligned}
\frac{\partial}{\partial x} &= \frac{\partial}{\partial \xi}\left(\frac{\partial \xi}{\partial x}\right)+\frac{\partial}{\partial \eta}\left(\frac{\partial \eta}{\partial x}\right)+\frac{\partial}{\partial \zeta}\left(\frac{\partial \zeta}{\partial x}\right) \\
\frac{\partial}{\partial y} &= \frac{\partial}{\partial \xi}\left(\frac{\partial \xi}{\partial y}\right)+\frac{\partial}{\partial \eta}\left(\frac{\partial \eta}{\partial y}\right)+\frac{\partial}{\partial \zeta}\left(\frac{\partial \zeta}{\partial y}\right) \\
\frac{\partial}{\partial z} &= \frac{\partial}{\partial \xi}\left(\frac{\partial \xi}{\partial z}\right)+\frac{\partial}{\partial \eta}\left(\frac{\partial \eta}{\partial z}\right)+\frac{\partial}{\partial \zeta}\left(\frac{\partial \zeta}{\partial z}\right)
\end{aligned} \tag{2.4}$$

The terms in brackets are called the metrics and relate the two coordinate systems. The metrics are derived from the general transformations given by equations (2.1) - (2.3). The time derivative remains unchanged for the fixed grid used in this study.

Substituting the transformed derivatives into equation (A.1) leads to the Navier-Stokes Equations for a curvilinear coordinate system, as shown below:

$$\frac{\partial \mathbf{Q}}{\partial t}+\frac{\partial(\mathbf{F}-\mathbf{F_v})}{\partial \xi}+\frac{\partial(\mathbf{G}-\mathbf{G_v})}{\partial \eta}+\frac{\partial(\mathbf{H}-\mathbf{H_v})}{\partial \zeta}=0 \tag{2.5}$$

where the solution vector $\mathbf{Q}$ and the flux vectors are given by:

$$\mathbf{Q}=J\begin{pmatrix}\rho\\ \rho u\\ \rho v\\ \rho w\\ \rho e_t\end{pmatrix},\mathbf{F}=J\begin{pmatrix}\rho u\\ \rho U u+p\xi_x\\ \rho U v+p\xi_y\\ \rho U w+p\xi_z\\ U(\rho e_t+p)\end{pmatrix},\mathbf{G}=J\begin{pmatrix}\rho V\\ \rho V u+p\eta_x\\ \rho V v+p\eta_y\\ \rho V w+p\eta_z\\ V(\rho e_t+p)\end{pmatrix},\mathbf{H}=J\begin{pmatrix}\rho W\\ \rho W u+p\zeta_x\\ \rho W v+p\zeta_y\\ \rho W w+p\zeta_z\\ W(\rho e_t+p)\end{pmatrix} \tag{2.6}$$

where (U,V,W) are the contravariant velocity components given by:

$$U=\xi_x u+\xi_y v+\xi_z w \tag{2.7}$$

$$V = \eta_x u + \eta_y v + \eta_z w \tag{2.8}$$

$$W = \zeta_x u + \zeta_y v + \zeta_z w \tag{2.9}$$

the viscous flux vectors are now defined as follows,

$$\begin{aligned}
\mathbf{F_v} &= J \begin{pmatrix} 0 \\ \xi_x\tau_{xx} + \xi_y\tau_{xy} + \xi_z + \tau_{xz} \\ \xi_x\tau_{xy} + \xi_y\tau_{yy} + \xi_z + \tau_{yz} \\ \xi_x\tau_{xz} + \xi_y\tau_{yz} + \xi_z + \tau_{zz} \\ \xi_x b_x + \xi_y b_y + \xi_z b_z \end{pmatrix}, \\
\mathbf{G_v} &= J \begin{pmatrix} 0 \\ \eta_x\tau_{xx} + \eta_y\tau_{xy} + \eta_z + \tau_{xz} \\ \eta_x\tau_{xy} + \eta_y\tau_{yy} + \eta_z + \tau_{yz} \\ \eta_x\tau_{xz} + \eta_y\tau_{yz} + \eta_z + \tau_{zz} \\ \eta_x b_x + \eta_y b_y + \eta_z b_z \end{pmatrix}, \\
\mathbf{H_v} &= J \begin{pmatrix} 0 \\ \zeta_x\tau_{xx} + \zeta_y\tau_{xy} + \zeta_z + \tau_{xz} \\ \zeta_x\tau_{xy} + \zeta_y\tau_{yy} + \zeta_z + \tau_{yz} \\ \zeta_x\tau_{xz} + \zeta_y\tau_{yz} + \zeta_z + \tau_{zz} \\ \zeta_x b_x + \zeta_y b_y + \zeta_z b_z \end{pmatrix},
\end{aligned} \tag{2.10}$$

In equation (2.10), (b_x, b_y, b_z) are the viscous contributions to the heat flux arising in the energy equation and these are expressed as

$$b_x = u\tau_{xx} + v\tau_{xy} + w\tau_{xz} + q_x \tag{2.11}$$

$$b_y = u\tau_{xy} + v\tau_{yy} + w\tau_{yz} + q_y \tag{2.12}$$

$$b_z = u\tau_{xz} + v\tau_{yz} + w\tau_{zz} + q_z \tag{2.13}$$

2.4 Turbulence Modelling: Spalart-Allmaras One Equation Model

For the purposes of modelling separated turbulent flows, the Spalart-Allmaras (S-A) one-equation turbulence model was implemented. The motivation behind the emphasis on the S-A model will become clearer in subsequent sections. Most one-equation models are based on the transport of turbulent kinetic energy. Nee and Kovasznay (1986), and more recently Baldwin and Barth (1990) and Spalart and Allmaras (1992) [67], have devised model equations for the transport of the turbulent viscosity (eddy viscosity) or a parameter proportional to the turbulent viscosity. The S-A turbulent kinematic viscosity is given by;

$$\nu_T = \tilde{\nu} f_{v1} \tag{2.14}$$

The parameter $\tilde{\nu}$ is an eddy viscosity that is obtained from the following transport equation:

$$\frac{\partial \tilde{\nu}}{\partial t} + U_j \frac{\partial \tilde{\nu}}{\partial x_j} = c_{b1}\tilde{S}\tilde{\nu} - c_{w1} f_w \left(\frac{\tilde{\nu}}{d}\right)^2 + \frac{1}{\sigma}\frac{\partial}{\partial x_k}\left[(\nu + \tilde{\nu})\frac{\tilde{\nu}}{\partial x_k}\right] + \frac{c_{b2}}{\sigma}\frac{\partial \tilde{\nu}}{\partial x_k}\frac{\partial \tilde{\nu}}{\partial x_k} \tag{2.15}$$

The closure coefficients and auxiliary relations are;

$$c_{b1} = 0.1355,\ c_{b2} = 0.622,\ c_{v1} = 7.1,\ \sigma = 2/3 \tag{2.16}$$

$$c_{w1} = \frac{c_{b1}}{\kappa^2} + \frac{1 + c_{b2}}{\sigma},\ c_{w2} = 0.3,\ c_{w3} = 2,\ \kappa = 0.41 \tag{2.17}$$

$$f_{v1} = \frac{\chi^3}{\chi^3 + c_{v1}^3},\ f_{v2} = 1 - \frac{\chi}{1+\chi f_{v1}},\ f_w = g\left[\frac{1+c_{w3}^6}{g^6+c_{w3}^6}\right]^{1/6} \tag{2.18}$$

$$\chi = \frac{\tilde{\nu}}{\nu},\ g = r + c_{w2}\left(r^6 - r\right),\ r = \frac{\tilde{\nu}}{\tilde{S}\kappa^2 d^2} \tag{2.19}$$

$$\tilde{S} = S + \frac{\tilde{\nu}}{\kappa^2 d^2} f_{v2},\ S_{ij} = \sqrt{2\Omega_{ij}\Omega_{ij}} \tag{2.20}$$

Ω_{ij} is the rotation tensor based on the mean velocity gradients, given by;

$$\Omega_{ij} = \frac{1}{2}\left(\frac{\partial u_i}{\partial x_j} - \frac{\partial u_j}{\partial x_i}\right) \tag{2.21}$$

One important observation in the S-A one-equation model is that d is the distance from the closest surface and hence the presence of a solid wall is automatically detected. The model can also include a transition correction that introduces four additional closure coefficients and two more empirical functions. The source terms for the eddy viscosity depends on the distance from the closest surface, d, as well as upon the gradient of $\tilde{\nu}$. As $d \to \infty$, the model also predicts no decay of eddy viscosity in a uniform stream far from solid boundaries. The model has been proved to be far superior than most $k-\varepsilon$ models in the simulation of separated flows. The S-A model is coupled to the RANS by

$$\mu_T = \rho\nu_T \tag{2.22}$$

The S-A model allows the estimation of the Reynolds stresses and the turbulent heat transfer terms by the Boussinesq approximation. The Navier-Stokes equations for the turbulent flow are written as before except that the model fluid viscosity is made up of two

contributions, namely the (eddy) turbulent and laminar parts i.e. $(\mu+\mu_T)$. The coefficient of the heat transfer terms is replaced by $(\mu/Pr+\mu_T/Pr_T)$, where Pr_T is the turbulent Prandtl number and is taken as 0.9.

2.4.1 RANS-LES hybridisation

The RANS approach tends to be the industry standard for the calculation of turbulent wall bounded flows as it permits the modelling of relatively high Reynolds number flows relevant to engineering applications. The RANS approach tends to give poor results for bluff body flows, where large-scale motion has an important impact on the spatial evolution of the mean flow field. On the other hand, DNS or LES are often too expensive to be applied to commercial CFD work. The Detached Eddy Simulation (DES) approach aims to deliver affordable predictions of separated flows at high Reynolds numbers relevant to engineering applications. It combines a the RANS approach in boundary layer regions with the LES approach in separated flow regions.

2.4.2 The Detached Eddy Simulation concept

Detached Eddy Simulation or DES is a concept introduced by Spalart *et al* [68] for the unsteady 3D numerical simulation of separated flows. Flow separation is inherently a 3D phenomenon and DES is well-suited for the numerical simulation of such flows. It functions as a sub-grid scale (SGS) in regions where the grid density is fine enough for LES resolution and as a RANS method where the grid spacing in all directions is larger than the thickness of the turbulent boundary layer. The model is able to sense the grid density and adjusts itself to a lower level of eddy viscosity relative to the RANS model to unlock the large scale instabilities of the flow, thus enabling the energy cascade to extend to the length scales close to the grid spacing. In other regions, primarily in boundary layers, the model will function as a RANS method. DES uses a single velocity and model field and there is no issue of smoothness between RANS and LES regions.

For the RANS model, the S-A one equation was initially used [68, 69], although technically there are no obstacles in implementing other turbulence models that function in a similar way to the S-A model. The main advantage of the S-A one-equation model is that it will automatically detect the presence of a wall, which is ideal when one is attempting a numerical solution of an external aerodynamic flow, such as that over a 3D wing. The standard S-A one-equation model uses the distance to the closest wall, d, as a length scale. The DES modification involves substituting for d everywhere in the equations by a new length scale $\tilde{d}$, which now depends on the grid spacing,

$$\tilde{d} = min(d, C_{DES}\Delta) \tag{2.23}$$

Δ is based on the largest dimensions of the grid spacing, i.e.,

$$\Delta = max(\Delta x, \Delta y, \Delta z) \tag{2.24}$$

It is then a matter of calibrating C_{DES}, the empirical model constant, which was proposed as 0.65 in [68]. This value provided a $-5/3$ power law for the turbulent energy spectrum.

2.4.3 The motivation behind DES

RANS simulations have proven to be inaccurate to predict unsteady cavity flows. LES and DNS are too expensive to be used for complex geometries. Therefore for a full simulation of a turbulent boundary layer, the RANS method is the only choice available at present. This is the first response of a DES motivation, i.e. to render the computational costs more manageable and maintain a high level of accuracy, approaching that of DNS/LES.

For massively separated flows, RANS methods usually struggle to predict the onset of flow separation and the flow downstream of it. In this respect LES is an attractive option to capture the large scale eddies (instabilities) accurately in a separated flow region. If L is the domain size and ℓ is the local size of the energy carrying eddies, for an LES resolution

the grid spacing must be of the order of ℓ at most. As the energy carrying eddies have $\ell \ll L$, they can create a formidable task in terms of computational cost and number of grid points required to resolve their motion. On the other hand, the characteristic length scale of the turbulent structures in a boundary layer $\ell_2 < \delta < L$, which is much smaller than *ell* and thus would require an even finer computational mesh. In the solution for a DES implementation, there are regions of $\tilde{d} \approx d$, where the model functions in a RANS mode, corresponding to a boundary layer type mesh, where, $\Delta \gg d$. Then in regions of $\tilde{d} \approx C_{DES}\Delta$ the model acts as a sub-grid scale for LES. These two regions are not explicitly defined, as there is a single velocity and eddy-viscosity field. There have recently been various attempts to apply DES to different flow problems, for example, axi-symmetric jets as in [70], flow around a sphere [71], and cavity flow simulations [56].

2.5 Numerical Method

Aeroacoustics involves inherently unsteady phenomena over a wide spectrum of frequencies and amplitudes. To faithfully represent the sound source physics it is essential that the numerical algorithm captures all the relevant scales in the flow field. Hence the discretisation method (spatial and temporal) must have a low dispersion and dissipation errors so that the wave propagation characteristics are preserved. An appropriate spatial discretisation can be obtained from a high order finite difference methods such as the one proposed by Lele [72]. In this work, a high-order compact finite-difference scheme similar to the one by Hixon [73] is used. The governing equations are integrated in time by a fourth order Runge-Kutta methods. Special non-reflecting boundary conditions are implemented that were developed specifically for CAA applications.

2.5.1 Spatial discretisation

Finite difference schemes can be classed as either explicit or implicit. Explicit schemes employ large computational stencils for accuracy. Implicit schemes, on the other hand,

achieve high-order accuracy by solving for the spatial derivatives as independent variables at each grid point. The drawback with such methods is that the inversion of a matrix system is required at any point in the computational domain to compute the local spatial derivatives. Recently, Hixon [73] applied a pre-factorisation procedure to reduce the size of the computational stencil, thereby simplifying the boundary condition specification and enhancing its robustness. This procedure reduces the tri-diagonal matrix to a system of lower and upper bi-diagonal system that may be solved in parallel, thus increasing efficiency. Recently Ashcroft and Zhang [74] further optimized the pre-factored schemes proposed by Hixon [73, 75] to obtain even smaller computational stencils and also improve the numerical wavenumber resolution characteristics of the scheme. According to Lele [72], a general compact approximation to the first-order derivative $(\partial f/\partial x)$ is given by

$$\beta D_{i-2} + \alpha D_{i-1} + D_i + \alpha D_{i+1} + \beta D_{i+2} = c\frac{f_{i+3} - f_{i-3}}{6\Delta x} + b\frac{f_{i+2} - f_{i-2}}{4\Delta x} + a\frac{f_{i+1} - f_{i-1}}{6\Delta x} \tag{2.25}$$

where D_i is the spatial derivative of f at point i. In the pre-factorisation as presented by Hixon [73] the derivative of D at a point i is defined as being half the sum of the forward and the backward derivatives

$$D_i = \frac{1}{2}(D_i^F + D_i^B) \tag{2.26}$$

where D_i^F is the forward derivative and D_i^B is the backward derivative. By defining the forward and backward derivative operators using equation (2.25), the generic stencils for the forward and backward derivative operators for a sixth-order is

$$\alpha_F D_{i+1}^F + \beta_F D_i^F + \gamma_F D_{i-1}^F = \frac{1}{\Delta x}[a_F f_{i+1} + b_F f_i + c_F f_{i-1}] \tag{2.27}$$

$$\alpha_B D_{i+1}^B + \beta_B D_i^B + \gamma_B D_{i-1}^B = \frac{1}{\Delta x}[a_B f_{i+1} + b_B f_i + c_B f_{i-1}] \tag{2.28}$$

The coefficients must be chosen such that when the two biased stencils are added the orig-

Coefficient	Value
$\alpha_F = \gamma_B$	0.276393202
$\beta_F = \beta_B$	0.723601797
$\gamma_F = \alpha_F$	0
$a_F = -c_B$	0.87939886714
$b_F = -b_B$	-0.75879773
$c_F = -a_B$	-0.120601133

Table 2.1: Stencil coefficients for the sixth-order forward and backward pre-factored compact operators.

inal sixth-order central compact difference scheme is recovered. Using Fourier analysis as shown by Hixon and Turkel [75], it is possible to determine the coefficients of the scheme according to the required level of accuracy. In the present work, a sixth-order accurate scheme is chosen and the coefficients are given in Table 2.1.

The central stencil presented in equations (2.27-2.28) are suitable only for the interior points of the computational space. If a multi-block approach is employed to subdivide the computational domain, at internal block boundaries, two eleven-point symmetric boundary stencils are employed. This stencil requires data from adjacent blocks. Thus the inter-block boundary stencil given by Hixon [76] is expressed as in equation (2.29). The corresponding stencil coefficients are given in Table 2.2. For other block boundaries, such as those at solid walls, two pairs of corresponding seven-point stencils are defined in equation (2.30) for the forward and backward operators as developed by [73]. The one-sided stencil coefficients are given in Table 2.3.

$$D_i^F = \frac{1}{\Delta x}\sum_{j=-5}^{j=5} b_i f_{i+j} \qquad D_i^B = \frac{1}{\Delta x}\sum_{j=-5}^{j=5} -b_i f_{i+j} \tag{2.29}$$

$$D_{i=1}^F = \frac{1}{\Delta x}\sum_{j=1}^{7} -e_j f_{i+j-1} \qquad D_{i=N}^F = \frac{1}{\Delta x}\sum_{j=N-6}^{N} -s_{N+1-j} f_{i+j-N}$$
$$D_{i=1}^B = \frac{1}{\Delta x}\sum_{j=1}^{7} s_j f_{i+j-1} \qquad D_{i=N}^B = \frac{1}{\Delta x}\sum_{j=N-6}^{N} e_{N+1-j} f_{i+j-N} \tag{2.30}$$

Coefficient	Value	Coefficient	Value
b_{-5}	-0.00054865580136	b_1	1.33473699809402
b_{-4}	0.00572148910474	b_2	-0.39229020218225
b_{-3}	-0.02745972472803	b_3	0.09057683838004
b_{-2}	0.08051553963950	b_4	-0.01419057897666
b_{-1}	-0.32813469266668	b_5	0.00110701937661
b_0	-0.75003403024106		

Table 2.2: Stencil coefficients for inter-block boundaries.

Coefficient	Value	Coefficient	Value
s_1	-2.74887508613327	e_1	2.15112491386674
s_2	6.91226506738309	e_2	-5.08773493261691
s_3	-8.57098789320798	e_3	6.42901210679204
s_4	7.29044096437465	e_4	-6.04289236895866
s_5	-3.93792558049982	e_5	3.56207441950018
s_6	1.2204502059161	e_6	-1.17959497940839
s_7	-0.16532249250833	e_7	0.16801084082501

Table 2.3: Biased stencil coefficients for the forward and backward operators.

2.5.2 Optimized pre-factored compact scheme

It is sometimes beneficial to sacrifice the formal order of accuracy of a spatial scheme to improve the performance of the discretisation over a wider wavenumber bandwidth, especially in the high wavenumber range. Ashcroft and Zhang [74] have performed a dispersion relation preserving optimization procedure to the sixth-order scheme presented in Section 2.5.1. Of particular relevance is the five-point optimized scheme that, although formally a fourth accurate method offers an enhanced spectral resolution over a larger range of wavenumbers. The general form of the forward and backward derivative operators of the five-point scheme is given in equations (2.31-2.32) and the coefficients of the scheme for minimal dispersion errors are given in Table 2.4.

$$\alpha_F D^F_{i+1} + \beta_F D^F_i = \frac{1}{\Delta x}[a_F f_{i+2} + b_F f_{i+1} + c_F f_i + d_F f_{i-1} + e_F f_{i-2}] \tag{2.31}$$

$$\alpha_B D^B_i + \gamma_B D^B_{i-1} = \frac{1}{\Delta x}[a_B f_{i+2} + b_B f_{i+1} + c_B f_i + d_B f_{i-1} + e_B f_{i-2}] \tag{2.32}$$

where the following restrictions are imposed on the coefficients of the forward and back-

Coefficient	Value
α_F	0.2974586350149729
β_F	0.71518963303413346
a_F	0.0
b_F	0.87203153537225117
c_F	-0.73137757420887159
d_F	-0.14065396116337958
e_F	0.0

Table 2.4: Five-point stencil coefficients for the fourth-order optimized pre-factored scheme.

ward stencils:

$$\begin{aligned} \beta_B &= \beta_F, \quad \gamma_B = \alpha_F, \quad a_B = -e_F \\ b_B &= -d_F, \quad c_B = -c_F, \quad d_B = -b_F, \quad e_B = -a_F \end{aligned} \tag{2.33}$$

As in the original un-optimized pre-factored compact scheme, specific boundary stencils are required to treat the inter-block boundaries, wall boundaries and inflow and outflow boundaries. For a domain with N points in a particular coordinate direction, the five-point fourth-order scheme the boundary stencil can be applied from $j = 3$ to $N-2$. Along internal boundaries, a central explicit stencil is employed, whereas along the external boundaries a biased explicit stencil is used. For the internal boundary treatment, two eleven-point stencils are employed as in the un-optimized scheme as detailed in equation (2.29), but the coefficients have been chosen to preserve the fourth-order accuracy while maintaining similar wavenumber resolution as in the interior points. The coefficients are listed in Table 2.4. The biased explicit stencils for the five-point fourth order scheme are required at nodes $j = 1$, $j = 2$, $j = N-1$ and $j = N$. The biased stencils as given by Ashcroft and Zhang [74] are given in equation (2.34) and the coefficients listed in Table 2.5. Additional relations are needed at the actual boundary points $j = 1$ and $j = N$. These stencils and the corresponding coefficients are given in equation (2.35)

Coefficient	Value	Coefficient	Value
s_1	1.968010730879214299	e_N	1.69865593578745236
s_2	3.336693493864702415	e_{N-1}	-2.66330650613529758
s_3	-1.769354795091761932	e_{N-2}	1.23064520490823806
s_4	0.400672032106273816	e_{N-3}	-0.26599463456039285

Table 2.5: Biased stencil coefficients for the five-point fourth-order scheme.

$$
\begin{aligned}
D_2^B &= \frac{1}{\Delta x}\sum_{j=1}^{4} s_j f_j & D_{N-1}^B &= \frac{1}{\Delta x}\sum_{j=N-3}^{N} e_j f_j \\
D_2^F &= \frac{1}{\Delta x}\sum_{j=1}^{4} -e_{N+1-j} f_j & D_{N-1}^F &= \frac{1}{\Delta x}\sum_{j=N-3}^{N} -s_{N+1-j} f_j
\end{aligned}
\tag{2.34}
$$

$$
\begin{aligned}
D_1 &= \frac{1}{\Delta x}\sum_{j=1}^{4} c_j f_j & D_{N-1}^B &= \frac{1}{\Delta x}\sum_{j=N-3}^{N} -c_{N+1-j} f_j \\
c_1 &= -33/8, \quad c_2 = 3, \quad c_3 = -3/2 \quad c_4 = 1/3
\end{aligned}
\tag{2.35}
$$

2.5.3 Time marching scheme

Multi-stage Runge-Kutta time integration schemes are widely employed in CFD applications due to their low storage requirements, efficiency and ease of implementation. The major drawback of such methods is the relatively low stability limits compared to implicit time integration schemes. For computing acoustic waves however, the stability criterion alone is not sufficient to judge the merits of a time integration scheme since implicit methods are highly dissipative and dispersive in nature and therefore can be unsuitable to aeroacoustic applications.

Traditionally, in Runge-Kutta schemes, the coefficients of the various stages are chosen such that the maximum possible order of accuracy is obtained for a given number of

stages. It is however possible to choose the coefficients so as to minimize the dissipation and dispersion errors for propagating waves. The low Dissipation and Dispersion Runge Kutta (LDDRK) schemes have been especially developed for this purpose. Hu *et al* [77] have proposed a two-step alternating LDDRK scheme for CAA algorithms, where they employed an optimization procedure to minimize the dissipation and dispersive errors associated to the temporal integration. The optimization procedure was such that it did not compromise the stability considerations of the scheme. The method alternates between 4 and 6 stages at successive time steps in the integration loop. The two additional stages in the even time steps are used to further improve the wave resolution characteristics in terms of minimum dispersion relations. A general time-dependent problem can be expressed by equation (2.36), where $\mathbf{U}$ is a vector of unknown quantities and $F(\mathbf{U})$ is a vector containing the discretized spatial derivatives.

$$\frac{\partial \mathbf{U}}{\partial t} = F\left(\mathbf{U}\right) \tag{2.36}$$

An explicit $P-$stage Runge-Kutta scheme advances the solution from time level $t = t_n$ to $t_n + \Delta t$, where Δt is the prescribed time step. The choice of time step is a critical parameter in explicit temporal schemes as it usually dictates the stability of the scheme. The stability considerations of the LDDRK schemes are extensively explored in [77]. The low storage representation of an explicit $P-$stage Runge-Kutta time advancement scheme can be expressed as

$$\mathbf{U}^{n+1} = \mathbf{U}^n + \mathbf{K}_P \tag{2.37}$$

$$\mathbf{K}_i = \Delta t F\left(\mathbf{U}^n + \beta_i \mathbf{K}_{i-1}\right), \quad i = 1, 2, ..., P \tag{2.38}$$

The optimized Runge-Kutta coefficients for the four/six alternating stages are listed in Table 2.6.

The constants c are related to the the Runge-Kutta constants in equation (2.38) through

Scheme	c_1	c_2	c_3	c_4	c_5	c_6
four-stage step	1	1/2	1/6	1/24	-	-
six-stage step	1	1/2	1/6	1/24	0.0162098	0.00286365

Table 2.6: LDDRK four/six stage scheme coefficients.

the following relations, details of which are provided in [77].

$$c_1 = 1, \quad c_2 = \beta_p, \quad c_3 = \beta_p\beta_{p-1}, \quad \ldots, \quad c_p = \beta_p\beta_{p-1}\ldots\beta_2 \tag{2.39}$$

2.6 Boundary Conditions

2.6.1 Adiabatic walls

Solid walls are represented using the no-slip boundary conditions;

$$(u, v, w) = 0 \tag{2.40}$$

$$\frac{dp}{dn} = 0 \tag{2.41}$$

$$\frac{dT}{dn} = 0 \tag{2.42}$$

Equation (2.40) implies that the fluid velocity vector at the wall surface is zero and equation (2.41) imposes a zero pressure gradient normal to the wall. An adiabatic wall boundary condition is implemented through equation (2.42). This condition implies that the heat flux normal to the wall is zero.

2.6.2 Inflow and outflow boundaries

Artificial boundaries have to be introduced for a finite computational domain and the partial differential equations governing the problem have to be satisfied in the sense of

Dirichlet or Neumann boundary conditions. Acoustic waves are solutions of the compressible Navier-Stokes equations and the inflow and outflow boundaries have to be applied to allow the waves to propagate out of the domain without any spurious reflections. Similarly, vorticity and entropy waves also need to propagate transparently through the computational boundaries. Therefore, numerical non-reflecting boundary conditions have thus been implemented.

The buffer zone technique is a group of boundary conditions based upon damping methods. For this approach, the grid is extended so as to create an extra zone in which the solution is damped by the application of low-pass filters, grid stretching or numerical damping. Following Wasistho [78], a buffer zone method is formulated as follows,

$$\tilde{\mathbf{Q}}^{n+1} = \overline{\tilde{\mathbf{Q}}^{n+1}} - \sigma(\overline{\tilde{\mathbf{Q}}^{n+1}} - \tilde{\mathbf{Q}}_{target}) \tag{2.43}$$

where $\overline{\mathbf{Q}^{n+1}}$ is the solution vector computed after each time step. The damping coefficient, σ, varies smoothly according to the function,

$$\sigma(x) = \sigma_{max} \left| 1 - \frac{L_b - x_b}{L_b} \right|^{\beta} \tag{2.44}$$

L_b is the length of the buffer zone, x_b is the distance from the inner boundary of the buffer and σ_{max} and β are coefficients that determine the shape of the damping function. $\tilde{\mathbf{Q}}_{target}$ is the target solution and has to be specified. Since the solution is damped in the buffer region, it has no physical meaning and does not model any real flow. The buffer zone is therefore removed during the post-processing of the solutions. Recently, Richards *et al* [79] assessed the performance of the buffer zone techniques compared to the traditional method of characteristics as presented by Thompson [80] and Giles [81]. The conclusion from the study was that the buffer zone technique is a much better approach for CAA algorithms. The main drawback is that it can be computationally expensive.

2.7 Code Validation

2.7.1 Laminar flat plate boundary layer

The laminar flow over a flat plate is a standard benchmark test for any Navier-Stokes solver being developed. Here, the approach flow is of Mach 0.5 and a boundary layer develops on the surface of the plate as shown in Figure 2.1. For this flow an analytical solution exists which is useful to validate the computed results.

The analytical solution is derived from the Howarth-Dorodnitsyn transformation [82] that removes density from the equations of motion. This approach is important as in a compressible flow the density varies with the wall-normal distance. Thus if the well known incompressible Blasius solution for the flat plate were used a discrepancy would occur in the velocity profile due to the density fluctuations. The transformation introduces a new variable

$$\overline{Y} = \int_0^y \frac{\rho}{\rho_\infty} dy \tag{2.45}$$

This integrates the density weighted with respect to the freestream value along the direction normal to the flat plate. The new variable in equation (2.45) replaces y in the equations of motion leaving x unchanged. This approach enables ρ to be removed explicitly from the initial Navier-Stokes equations, and in doing so the Blasius equation is recovered which can be solved numerically to obtain a solution for the velocity profile across the boundary layer. The compuational setup and results are shown in Figure 2.2.

The computational mesh used is shown in Figure 2.2(a). This consists of 2 blocks with 50x150 grid points in the x and y directions respectively. The mesh was refined near the solid wall so as to resolve the velocity gradients arising at the surface giving $\delta y^+ = 1.0$ at$x > 0.3$, where δy^+ is the first interior node normalized wall-normal distance. This results in a first node distance from the wall of 2.0x10^{-5}m which will be taken into ac-

count when determining the time step required for a stable solution. The normalized wall-normal coordinates are defined in equations (2.46) and (2.47), where τ_w is the wall shear stress.

$$u^+ = \frac{u}{u_\tau}, y^+ = \frac{Re}{M}\frac{y u_\tau}{\nu} \tag{2.46}$$

$$u_\tau = \sqrt{\frac{M}{Re}\frac{\tau_w}{\rho}} \tag{2.47}$$

The CFL condition dictates the stability of the time integration scheme and depends directly on the size of the smallest mesh spacing. In this case the Courant number is 0.25. The Mach number in this case is 0.5.

A common validation procedure is to compare the computed velocity profile against the Blasius solution described earlier. Figure 2.2(b) shows the Blasius solution (solid line) against the computed velocity profile (solid symbols) at the trailing edge of the flat plate. The Blasius solution and the numerical prediction are in good agreement

2.7.2 Turbulent flat plate boundary layer

The turbulent flow over a flat plate was simulated to validate the Spalart-Allmaras one equation model [67]. Part of the boundary layer was computed with periodic boundary conditions at the inflow and outflow as shown in Figure 2.3. The domain size is L_y and L_x respectively and has 60 points in the streamwise direction and 100 points in the wall normal direction.

The Reynolds number based on the length of the flat plate, Re_L is 5×10^5 and the freestream Mach number is 0.5. The first mesh point away from the wall is $\delta y = 1.0 \times 10^-5$m which corresponds to $y^+ = 1.0$. Non-dimensional wall parameters such as u^+ and y^+ are defined in equations (2.46) and (2.47). An equilibrium turbulent boundary layer velocity profile, normalized according to equation (2.46), follows

$$u^+ = y^+ \tag{2.48}$$

in the viscous sub-layer, and

$$u^+ = \frac{1}{\kappa} \ln y^+ + B \tag{2.49}$$

in the logarithmic region, referred to as the log layer. The approximate values for the constant B and the von Kàrman constant κ are 5.5 and 0.41 respectively. The computational setup and results are shown in Figure 2.4. Figure 2.4(a) shows the computational domain and Figure 2.4(b) shows the comparison between the theoretical logarithmic velocity profile and the computed profile plotted using the normalized wall-normal coordinates. There is a reasonable agreement between the theoretical result and the numerical prediction.

2.8 Summary

The mathematical and numerical methods that have been implemented in the present work have been introduced. The implementation of the turbulence model together with the DES approach has also been discussed. The performance of the viscous solver has been assessed over two standard test cases. With the laminar flow over a flat plate, it has been shown that the velocity profile shows a good agreement with the Blasius profile. With a turbulent flow over the flat plate, the Spalart-Allmaras one equation model was used. The velocity profile in this way agrees with the law of the wall and validates the implementation of the turbulence model.

2.9 Chapter 2 Figures

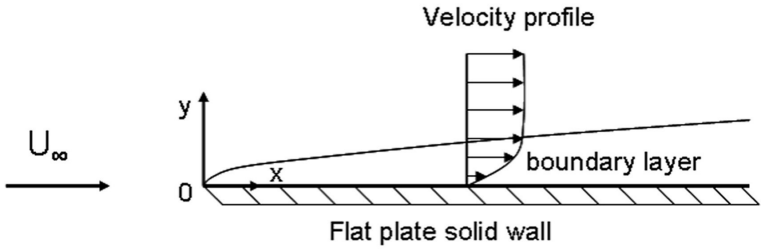

Figure 2.1: Laminar flat plate boundary layer.

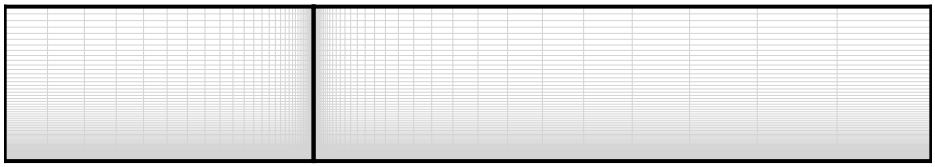

(a) Computational domain.

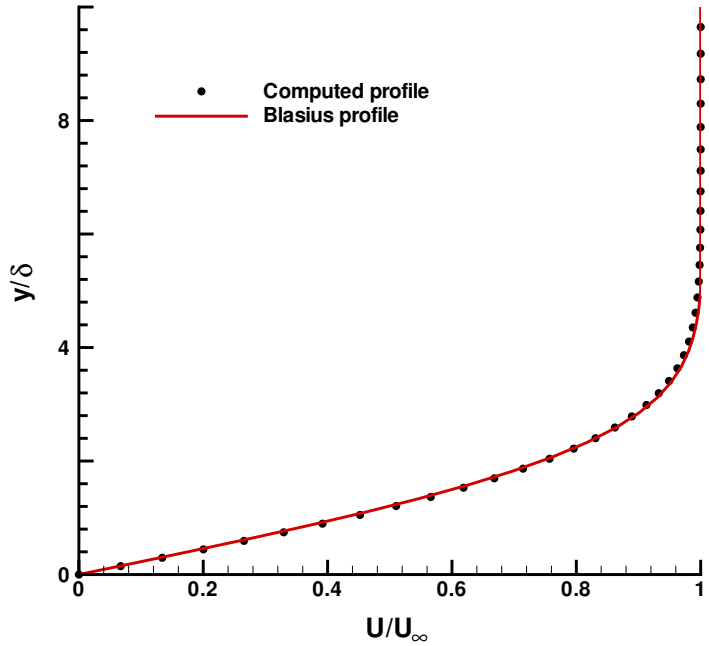

(b) Velocity profile.

Figure 2.2: Laminar flow over a flat plate, Mach 0.5.

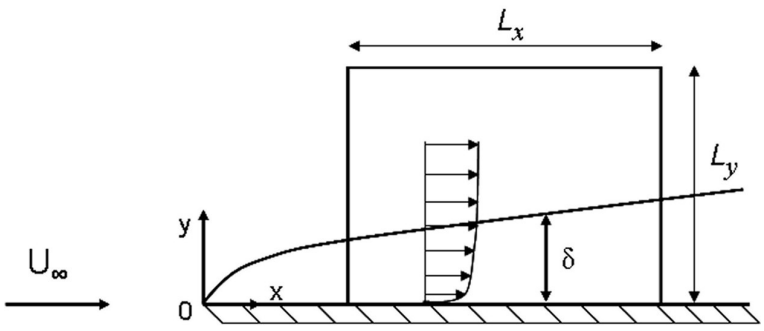

Figure 2.3: Turbulent flat plate boundary layer.

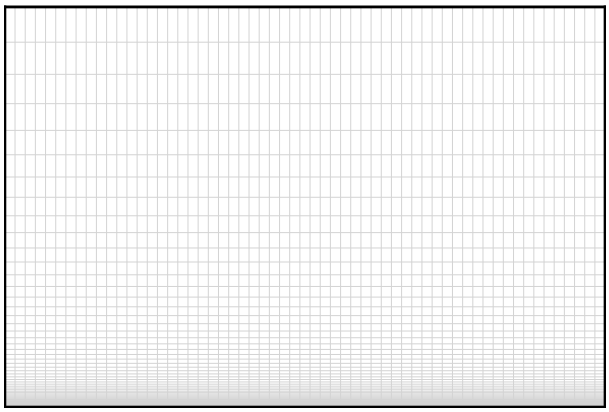

(a) Computational domain for turbulent boundary layer.

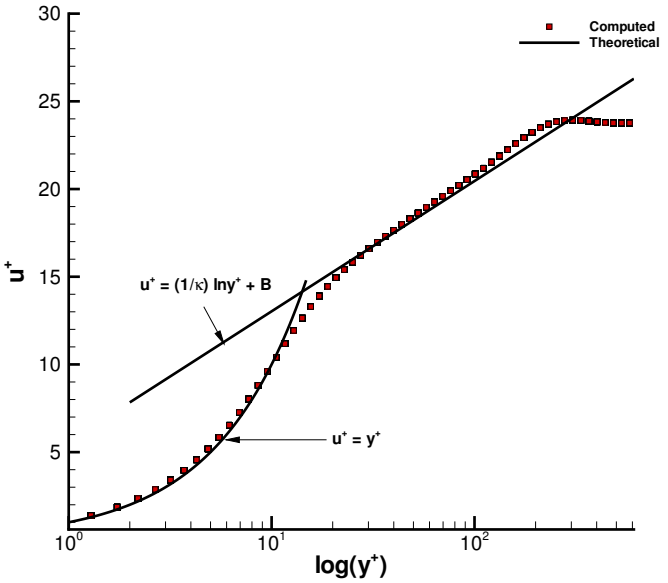

(b) Turbulent boundary layer profile, $M = 0.5,\ Re_x = 500000$.

Figure 2.4: Turbulent flat plate boundary layer computation.

Chapter 3

Grid Sensitivity Study

3.1 Introduction

The aim of this chapter is to perform a grid sensitivity study to evaluate the performance of the high-order flow solver on different mesh densities. For this purpose, the laminar flow over a rectangular cavity is chosen as a model problem.

3.2 Computational Approach

To study the effect of grid sensitivity on the the simulation of the cavity flow, two computational meshes were employed to simulate the flow over a cavity. The cavity geometry has a length-to-depth ratio (L/D) of 2 and the flow Mach number is 0.4. The Reynolds number based on the cavity depth, Re_D, is 3000. The first mesh, which is referred to as the coarse mesh, has 100 points in each direction and comprises of 8 blocks. The computational domain extends to $5L$ in the streamwise direction and $5L$ in the flow-normal as shown in Figure 3.1(a). The second mesh which is dubbed the fine mesh has 180 points in streamwise direction and 200 points in the flow-normal direction. The domain is subdivided into 16 blocks, as shown in Figure 3.1(b). The refined mesh therefore is

approximately seven times denser. The boundary layer thickness at the cavity upstream edge is approximately $0.2D$.

Under the appropriate conditions, the flow over a cavity is known to undergo a self-sustained oscillation of the shear layer and can be empirically represented by the Rossiter model. The modified Rossiter equation was presented in Section 1.2. The main oscillation frequency of the cavity shear layer is well predicted by equation (1.6).

A grid independent solution is obtained if both grids, under the same simulation parameters, predict the same Rossiter modes. Equation (1.3) gives the theoretical Strouhal numbers, St, of vortex shedding from the cavity leading edge. Taking κ as 0.57, the Strouhal number for the first Rossiter mode is 0.34. The results from the simulation of the flow over the 2D cavity will now be compared for the coarse and fine meshes.

3.3 Cavity Flow Field

3.3.1 Unsteady pressure fluctuation

The pressure was monitored at the mid-point of the cavity floor for the two cases and the predicted history is shown in Figure 3.2(a). The pressure fluctuations were normalized with respect to free stream speed of sound a_∞ and density ρ_∞. The cavity length was employed as the relevant length scale to non-dimensionalise the time.

It can be seen from Figure 3.2(a) that the flow predicted on both the the fine and coarse computational grids has settled in a self-sustained oscillatory state. The variation of the pressure fluctuations with time for the coarse mesh is similar to that of the fine mesh. More insight can be obtained by performing a discrete Fourier transform (DFT) of the signals to analyze their frequency contents. The $\Delta St = 0.0003$ constant bandwidth power spectra obtained are shown in Figure 3.2(b). The striking feature of the power spectra for both grid densities is that that they agree over a wide range of frequencies. This shows

that, firstly, the numerics are performing as required and, secondly, the same physical phenomenon is modelled with both computational meshes. The only major difference between the power spectra of the coarse and of the fine mesh is that they appear to diverge at higher frequencies. This is due to the numerical dispersion and dissipation in the scheme that affects higher frequency waves, but it is to be expected that the finer mesh provides more spatial resolution in the higher end of the frequency-wavenumber spectrum. However, the underlying physics is within the Strouhal range of $St = 0.1$ to $St = 1.0$. It is in this range of frequencies that the dominant shear layer oscillation modes appear. In fact, from Figure 3.2(b), the close agreement between the spectra extends up to the third visible peak at $St = 0.99$. The peaks at $St = 0.66$ and $St = 0.99$ are harmonics of the fundamental mode. The predicted fundamental mode from equation (1.6) is $St = 0.34$ and the computed Rossiter Mode 1 from both the fine and coarse meshes is 0.33. The amplitude of the first mode in the coarse mesh computation is 148.6 dB and the fine mesh calculation indicates an amplitude for the first mode of 149.4 dB. Therefore, the coarse mesh performs adequately with respect to the computed frequencies and amplitudes.

3.3.2 Time averaged mean flow

This section is concerned with comparing the mean flow results obtained from the coarse and fine grids.

Figure 3.3 shows the time-mean velocity profiles at the cavity upstream edge obtained from the fine and coarse grids. The predictions show that the oncoming boundary layer profiles are similar. Hence there is no dependency in the upstream mean flow on the level of mesh refinement at the separation point.

Figure 3.4 shows the pressure coefficient plotted along the cavity floor at $y/D = -1.0$. The solid line shows the predictions from the fine mesh and the dashed line, the ones from the coarse mesh. It can be seen that the trends in the variation of the pressure coefficient are similar. The peak and trough are indicative of the presence of a large

time-mean re-circulating flow structure inside the cavity. The position of the minimum pressure is computed at the same location for both the coarse and fine meshes at $x/L = 0.69$. Similarly, the position of the maximum pressure in both cases is the same at $x/L = 0.83$. However, the C_p is lower in the fine mesh predictions at the maximum and the minimum points. Specifically the difference in the predicted pressure minimum is 10.1% and for the pressure maximum the difference is 14.8%. This shows that the aerodynamic predictions are mesh dependent. Whereas the predictions show that the numerical model of the laminar cavity flow is not quantitatively mesh-converged, the fine mesh predictions do not show any deviation in trend with respect to the coarse mesh predictions. This indicates that the two models are reproducing the same flow structure and this adequate for the purpose of the current work, which is an investigation on the laminar cavity flow instability mode shape at $M_\infty = 0.4$, $Re_D = 3000$, $L/D = 2$ and $\delta/D = 0.2$.

The local Mach number variation along $y/D = -0.9$ is shown in Figure 3.5. There is a good agreement between the Mach number predictions from the coarse and fine mesh computations, except at $x/L = 0.6$ and $x/L = 0.83$. Due to the lower due to the lower C_p distribution predicted by the fine mesh model, the local flow speeds at these locations are slightly higher than in the calculation performed on the coarse mesh.

The streamlines for the coarse and fine mesh are shown in Figure 3.6(a) and Figure 3.6(b) respectively. The streamlines in the two cases show a good similarity in flow pattern. The separation and re-attachment points along the cavity floor can be observed to be at the same location. This is confirmed by the similar trends in pressure distribution along the cavity floor. The downstream clockwise and the upstream anti-clockwise re-circulation patterns are similar on both mesh refinement levels.

Figure 3.7(a) and 3.7(b) show the the time mean vorticity contours predicted on the coarse and fine mesh respectively. The vorticity is non-dimensionalised with respect to the free stream flow speed and the cavity length as the reference length scale. The shape and size of the large-scale structure inside the cavity are similar in both cases.

3.4 Summary

A grid sensitivity study is conducted on a two-dimensional laminar cavity CAA model using two mesh densities. The unsteady pressure predicted at $x/L = 0.5$ on the cavity floor show the same dominant oscillation mode of the cavity, which is the Rossiter mode 1. A DFT analysis of the predicted pressure history on the coarse and fine meshes show that the spectra are characterized by the same harmonic sequence and there is only a marginal difference in the amplitude of the dominant tones. The time averaged predictions showed that on both mesh densities, using the same solver and flow parameters, the same flow features are produced. The shear layer spans the mouth of the cavity with a dominant re-circulating region centered at approximately $x/L = 0.65$ from the leading edge. Therefore, it has been shown that, for the selected test case, a grid independent flow pattern is obtained from the implemented flow solver. The results of the this study are used in the subsequent computations.

3.5 Chapter 3 Figures

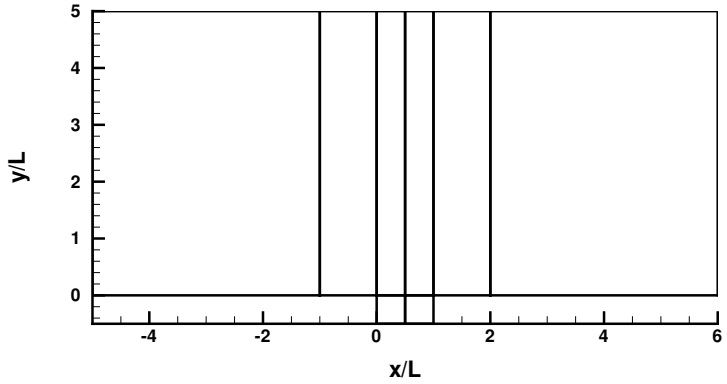

(a)

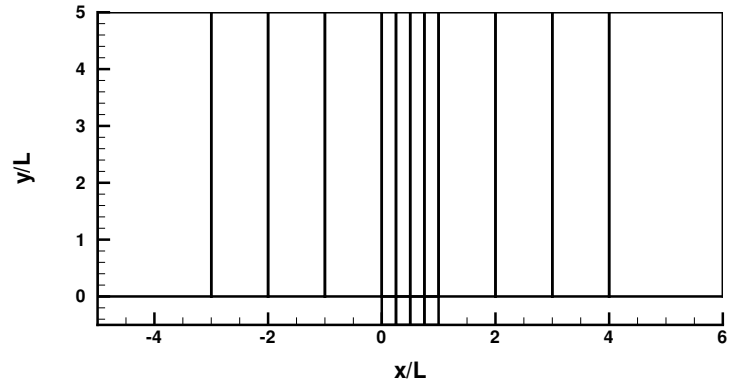

(b)

Figure 3.1: Computational meshes employed for grid sensitivity study: (a) coarse mesh and (b) fine mesh.

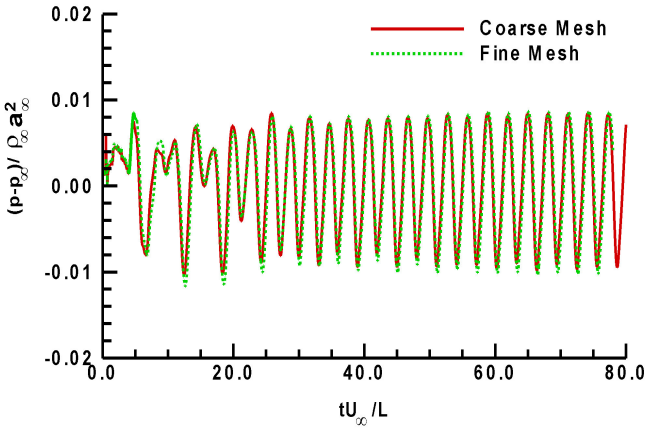

(a)

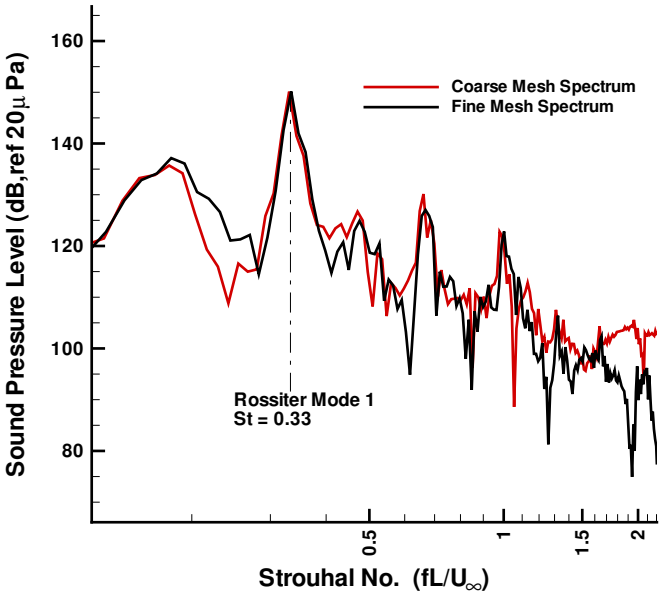

(b)

Figure 3.2: Time variation of pressure fluctuations for the coarse and fine meshes: (a) pressure fluctuations and (b) spectra, $\Delta St = 0.0003$.

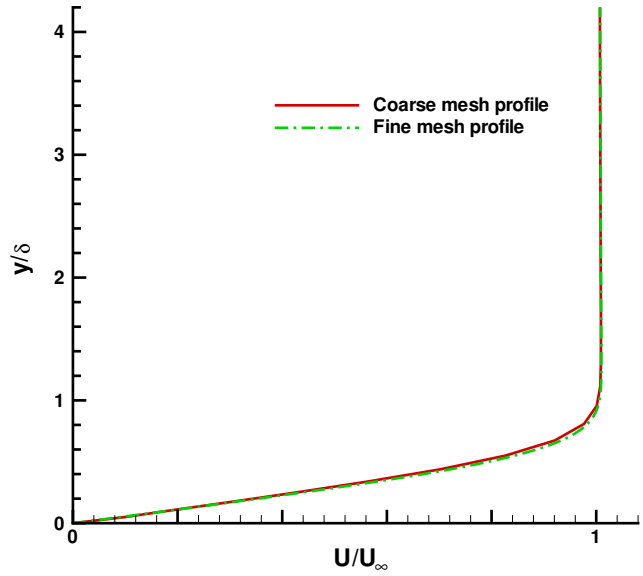

Figure 3.3: velocity profiles at $x/L = 0.0$.

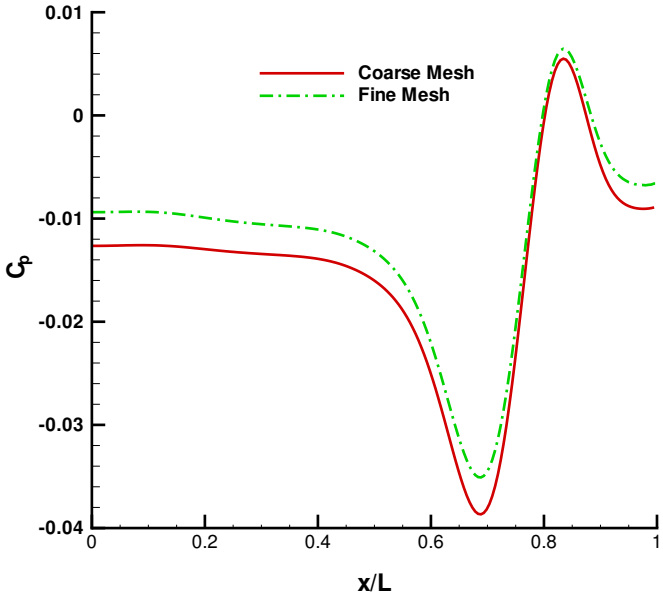

Figure 3.4: Pressure variation along the cavity floor, y/D = -1.0.

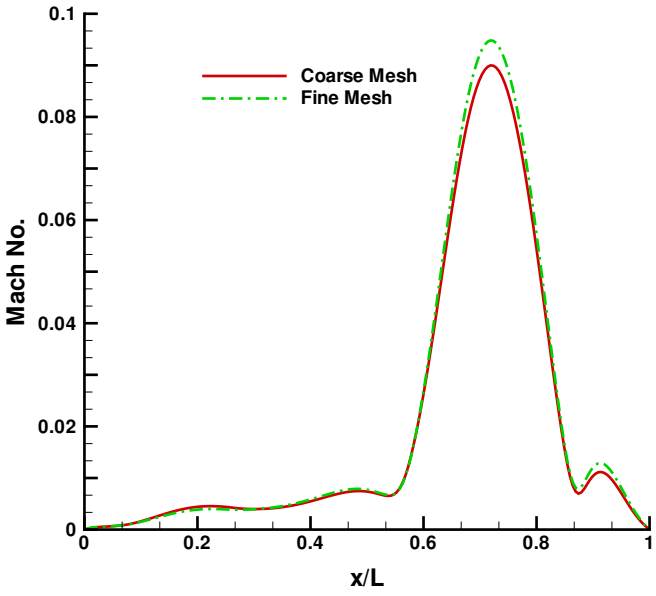

Figure 3.5: Local Mach number variation along $y/D = -0.9$.

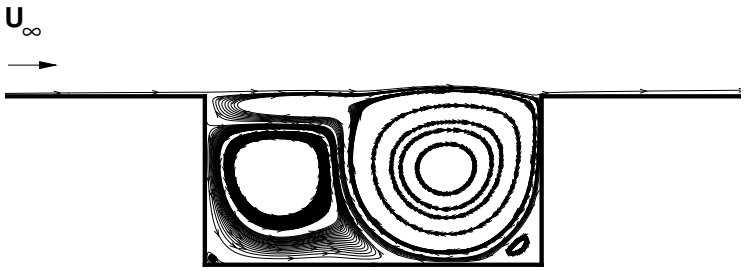

(a)

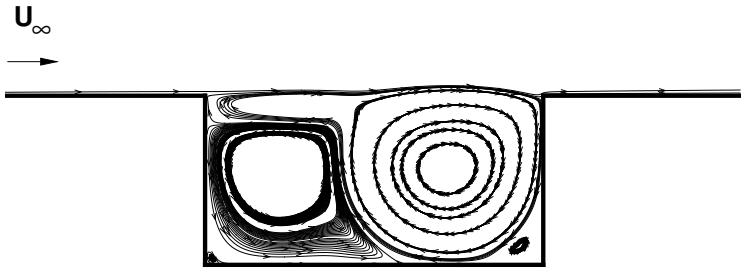

(b)

Figure 3.6: Time averaged streamline patterns: (a) coarse mesh and (b) fine mesh.

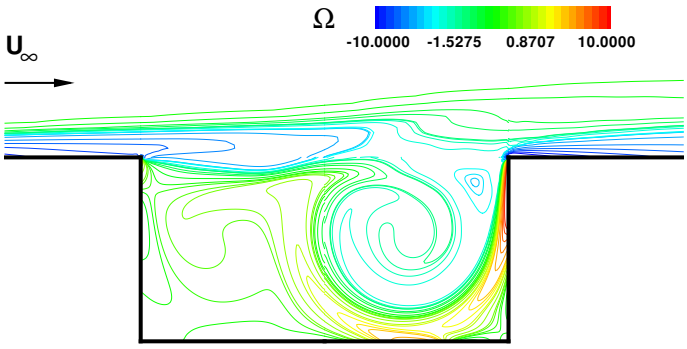

(a)

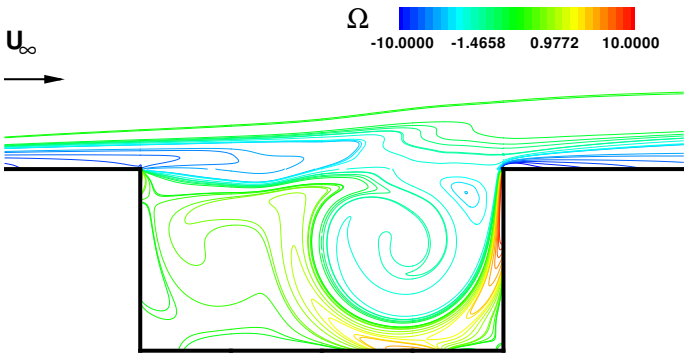

(b)

Figure 3.7: Time averaged vorticity contours: (a) coarse mesh and (b) fine mesh.

Chapter 4

Two-Dimensional Cavity Flow Simulations

4.1 Overview

The results of numerical simulations of the flow over 2D cavities are presented for a range of length-to-depth ratios. In the near field, the flow solutions are computed with the Detached Eddy Simulation (DES). At observer positions far away from the source regions, the acoustic fields are calculated using the Ffowcs William-Hawkings (FW-H) integral radiation model. In this chapter, the effect of cavity geometry on the near-field aerodynamics and on the acoustic radiation is investigated.

4.2 Introduction

The behaviour of 2D cavity flows is a function of several parameters, including the length-to-depth ratio. Depending on this ratio, the cavity flow can be classed as either open, transitional or closed according to Plentovich *et al* [11]. In the open cavity case, the shear

layer formed due to the boundary layer separation at the upstream cavity edge bridges the whole cavity mouth. The closed cavity case, the boundary layer re-attaches on the cavity floor and detaches again towards the aft corner, forming effectively a backward facing step flow followed by a forward facing step flow. This classification was based on the static pressure distribution of the supersonic flow over 3D cavities [11]. The same open, transitional and closed cavity flow patterns have been observed by various researchers [58, 62, 55] performing the numerical simulation of cavity flows. In all cases, however, the flow-induced cavity oscillations are characterized by large fluctuations in the pressure, density and velocity, resulting in significant noise radiation dominated by strong tonal components. In this chapter, the flow characteristics as well as the noise radiated from five basic rectangular cavity geometries is investigated numerically using the methodology explained in Chapter 2. To compare the far field noise, a hybrid approach is adopted in which the near field aerodynamic flow computations are coupled with integral solutions of the Ffowcs Williams and Hawkings (FW-H) equation.

4.3 Geometry and Flow Conditions

The basic geometries investigated are 2D cavities with various length to depth ratios. A rectangular cavity is characterized by its length (L) and its depth (D). According to Ahuja and Mendoza [28], a 2D cavity is formed whenever the L/W ratio is less than unity so that the shear layer displays a large degree of spanwise coherence and can thus be represented as 2D. In the current analysis, the oncoming flow is subsonic and the freestream Mach number $M_\infty = 0.5$. The Reynolds number based on the depth $Re_D = 60{,}000$ is constant for all selected 2D cavity test cases, giving a cavity depth of $5.1mm$ in all cases. The oncoming boundary layer thickness at the cavity leading edge for all cases is $\delta = 1.02$mm, so that $\delta/D = 0.2$.

4.4 Computational Domain

The computational domains employed were designed to resolve the shear layer dynamics accurately and a small portion of the acoustic field. The 2D geometry is given in Figure 4.1, where the geometrical parameters such as the length and depth are shown. A typical domain is shown in Figure 4.2 and is of a multi-block topology. The inter-block boundaries are shown in solid dark lines. Each block has 186 nodes in the x direction and 193 nodes in the y direction with a total of 574,000 grid points per geometry. The domain is subdivided into 16 sub-domains and the flow simulations are performed using Southampton University's Iridis PC cluster. For these 2D calculations, 16 2.5 GHz P4 processors were employed. The shear layer lies in the region $-0.10 \leq y \leq 0.10$. This region consists of approximately 143,592 computational nodes. The domain extends to $15L$ in the streamwise direction and $5L$ in the vertical direction. As required for viscous calculations, the mesh is clustered with a hyperbolic tangent distribution near the wall regions. A minimum of 40 points is used inside the boundary layer regions. For all the geometries studied, the first grid point above all solid walls is placed such that $y^+ = O(1)$.

4.5 2D Cavity Flow Field

4.5.1 Mean flow characteristics

The mean aerodynamic flow field obtained from each 2D cavity can be understood through an examination of the static pressure distribution along the cavity floor. The time averaged streamline patterns on the other hand provide a useful visual aid to interpreting the static pressure plots. In this section, the mean flow characteristics observed from each 2D cavity case are examined and compared.

Charwat *et al* [10] performed an experimental investigation on separated flows. From this investigation, they classified the flow over rectangular cutouts as being either closed

or open based on the cavity floor pressure distribution. Following this, from their experimental studies, Plentovich *et al* [11] also defined an open cavity as one where the variation in cavity floor pressure is quite small. Typically, $C_p \approx 0$ for $x/L < 0.6$ and C_p increases with x/L for $x/L > 0.6$. This classification was based from experimental measurements on 3D cavities at transonic and supersonic speeds. Based on the observations from these past investigations, the pressure distributions on the cavity floors in the present simulations are examined to attempt to classify the 2D cavities accordingly.

The time averaged static pressure coefficient C_p distribution for the $L/D = 2$ cavity is shown in Figure 4.3. There is a gradual drop in pressure until a minimum in the C_p is reached at $x/L = 0.68$. This minimum in the pressure distribution is followed by a rapid rise in C_p culminating in a C_p maximum at $x/L = 0.81$. This trend in the pressure distribution indicates the presence of a large and stable vortex within the cavity. This feature is evident on inspection of the streamline patterns shown in Figure 4.4. The large re-circulation region is clearly shown as well as the secondary counter re-circulating vortices at the cavity corners. The secondary depression in the pressure distribution located at $x/L = 0.91$ can be attributed to the re-circulation close to the downstream corner. It can be seen from Figure 4.4 that the large stable vortex occupies a large portion of the cavity opening. The shear layer can be seen to span the entire mouth of the cavity and it re-attaches on the cavity downstream wall. On this basis, the cavity clearly falls in the open category as explained in [11]. However, as can be seen in Figure 4.3, there are oscillations in the C_p of the order of ± 0.1 near the bottom of the front and back walls. This can be explained by the presence of a large scale re-circulation region followed by secondary corner re-circulation regions commonly referred to as Moffat vortices.

For shallow cavities $L/D \geq 4$, previous investigators such as Plentovich *et al* [11] and Tracy and Plentovich [14] demonstrated that the flow resembles that of a backward facing step. Moreover, they classed such a behaviour as a 'closed' cavity. However, even for very shallow cavities where $L/D > 10$, there is a feedback process involved due to the presence of the downstream edge in the cavity configuration [18]. Predictions for an $L/D = 4$ cavity flow are presented in Figures 4.3 and 4.5. There is no direct comparison between

the computed mean pressure coefficient and the corresponding experimental data in [11], since most experiments were performed at high Reynolds numbers for three-dimensional cavities. However a good qualitative agreement exists with the 2D simulations performed by Shieh and Morris [56, 58].

From Figure 4.3 it is observed that there exists a peak and trough behaviour in the C_p distribution in the fore portion of the cavity. The minimum pressure coefficient is located at $x/L = 0.021$ and the maximum is at $x/L = 0.067$. This corresponds to a secondary corner anti-clockwise re-circulation. The re-circulation is evident upon observation of the mean streamline patterns in Figure 4.5. Following this peak in the pressure distribution, the pressure decreases to a minimum at $x/L = 0.21$. This feature in the pressure distribution is due to the presence of the large clockwise re-circulation region inside the cavity. It can be seen that the effective length of the structure is of the order of the cavity length. The height of the structure is of the order of the cavity depth. This differs considerably from the $L/D = 2$ cavity. The rise in pressure following the minimum pressure point is explained by the fact that there is a significant diffusion of the shear layer inside the cavity opening towards the downstream corner. This rise in pressure displays an observable change in the slope at $x/L = 0.45$. The change in slope is indicative of the shear layer diffusion inside the cavity. It does not however indicate that the shear layer re-attaches on the cavity floor. An examination of Figure 4.5 suggests that the shear layer re-attaches on the downstream wall, but at a much lower location than in the $L/D = 2$ cavity. At the aft bottom corner of the cavity, secondary clockwise re-circulating eddies are observed. As the fluid flows out of the opening, the sharp downstream trailing edge causes the flow to separate, creating a re-circulating zone just downstream at the trailing edge which is closed by the downstream boundary layer re-attaching on the downstream bulkhead. This cavity is neither closed nor open. It can be classed as transitional as it displays some features of an open cavity as well as some characteristics of a closed one.

The pressure distribution along the cavity floor for the $L/D = 5$ case is broadly similar to that of the $L/D = 4$ case. There are however subtle differences in the mean streamline patterns and the static pressure. The first trough and peak trend is observed very close to

the bottom front corner as in the previous case, corresponding to the corner re-circulation. The minimum in the pressure distribution is located at $x/L = 0.019$ and the maximum at $x/L = 0.053$. This small anti-clockwise rotating corner eddy is closer to the front wall than in the $L/D = 4$ case. There is a large scale clockwise vortex centred downstream of the C_p minimum at $x/L = 0.13$. $x/L = 0.13$ corresponds to the local flow separation on the cavity floor incurred due to the presence of the secondary re-circulating pattern and the large clockwise vortex. These two re-circulating structures are in the opposite sense to each other, thus giving the minimum in the pressure distribution. The other noticeable feature is the clear decrease in the gradient of the pressure distribution with increasing x/L. At $x/L = 0.45$, there is a change in the pressure gradient, such that the fluid now accelerates out of the cavity. From the pressure distribution, there is no evidence of flow re-attachment on the cavity floor, in which case, the cavity regime is still transitional.

Further increasing the L/D produces a marked change in the pressure distribution. This is studied for two cavities of $L/D = 8$ and $L/D = 10$ respectively. The general shape of the pressure distribution up to $x/L = 0.1$ resembles that of the $L/D = 5$ cavity in both cases. For the peak and trough variation between $x/L = 0.01$ and $x/L = 0.03$ denoting the secondary counter clockwise re-circulating flow structure, it can be seen that these are slightly closer to the front wall than in the previous cases (Figures 4.7 and 4.8). The depression in the distribution denoting the local flow separation at the cavity floor due to the main clockwise structure and the secondary structure is also closer to the backward facing wall. For the $L/D = 8$ cavity the minimum is located at $x/L = 0.083$ and at $x/L = 0.069$ for the $L/D = 10$ cavity. This signifies that the centre of the main vortical structure moves backwards with increasing x/L. The rise in pressure following these minima occurs in the same way as in the $L/D = 5$ cavity, but the pressure gradient increases with increasing L/D. For the $L/D = 8$ cavity, there is a noticeable inflection point at $x/L = 0.42$, indicative of the shear layer re-attaching on the cavity floor. The re-attachment position lies between $x/L = 0.4$ and $x/L = 0.5$. At $x/L > 0.5$, there is a clear plateau in the static pressure distribution. This is followed by a gradual C_p rise as the fluid exits the cavity in the aft portion. The situation is slightly different in the $L/D = 10$ case. The inflection in

the static pressure distribution is till evident and occurs at $x/L = 0.33$. In this case case, there is no obvious plateau in the static pressure plot. Instead, the static pressure displays a gentle depression and then rises further downstream as the fluid exits the cavity in the aft portion. In both cases, the cavity flow regime changed from transitional to closed.

4.5.2 2D cavity oscillation modes

In this study, the flow Mach number and incoming boundary layer thickness are fixed so that the effect of the L/D on the aerodynamic and acoustic fields can be investigated.

The unsteady pressure was monitored on the cavity floor at $x/L = 0.5$. The spectral content of the pressure signal obtained for the $L/D = 2$ cavity is shown in Figure 4.9. The $\Delta St = 0.0025$ constant bandwidth spectrum is plotted in terms of the sound pressure level and the Strouhal number, scaled with the cavity length. There is a noticeable peak in the spectrum at a Strouhal number of 0.2. This does not correspond to a Rossiter mode as predicted by equation (1.3) but to the first sub-harmonic of the first Rossiter mode. The first Rossiter mode is shown in the spectrum at a Strouhal number of 0.38. The amplitude of this broad peak is 153.7 dB. The peak at the Strouhal number of 0.58 corresponds to a non-integer multiple of the the first Rossiter mode. This arises due to the complex nature of the hydrodynamic interaction that occurs at the cavity trailing edge. According to Rockwell and Knisely [34], the nature of the interaction of the vortical structures with the cavity trailing edge, gives rise to non-integer multiples of the fundamental mode. The amplitude of this peak is 7.1 dB lower than that of the first Rossiter mode which tends to support the theory that this mode is generated by a non-linear combination of the first and second Rossiter mode by a modal energy exchange process. The second Rossiter mode is located at a Strouhal number of 0.77 and its amplitude is 11.5 dB lower than the first mode. It is clear from the spectrum that the dominant mode is the Rossiter mode 1. It is however unclear at what instant in time do these modes occur and the duration of time at which the cavity shear layer is under the influence of each mode present in the spectrum. A wavelet analysis would be useful extension of the current study, to resolve

the time-frequency characteristics of the cavity instability.

The time-dependent analysis of the cavity floor pressure sampled at $x/L = 0.5$ was repeated for the $L/D = 4$ 2D cavity. A $\Delta St = 0.0033$ constant bandwidth spectrum was obtained by the discrete Fourier transform of the predicted pressure history as shown in Figure 4.10. The first noticeable feature in the spectrum, shown in Figure 4.10 is the peak at a Strouhal number of 0.13, corresponding to the Rossiter mode 1. The amplitude of this peak is 165.4 dB. The first harmonic of the fundamental mode is observed at a Strouhal number of 0.26. The presence of the harmonic is again indicative that the vortical structures in the shear layer interact in a complex manner with the cavity trailing edge. The Rossiter modes 2 and 3 are also observed in the spectrum at Strouhal numbers of 0.38 and 0.68 respectively. The amplitudes of these two modes are nearly equal and are 144.7 and 144.6 dB respectively. It is apparent that the dominant mode is the Rossiter mode 1, which is about 20 dB higher in amplitude than the two higher modes.

Figure 4.11 shows a $\Delta St = 0.0028$ constant bandwidth power spectrum of the predicted cavity floor pressure fluctuations at $x/L = 0.5$ for an $L/D = 5$ cavity. It can be observed that the Rossiter mode 1 is present at a Strouhal number of 0.15, together with its harmonics at Strouhal numbers of 0.29 and 0.44 respectively. The presence of the higher harmonics indicate that the mode 1 oscillation undergoes some modulation giving rise to the higher frequency harmonics. The Rossiter mode 3 is also observed at a Strouhal number of 0.59, the amplitude being 21.7 dB lower than the first mode. The dominant oscillation characteristics of this cavity would seemingly be the that of the first Rossiter mode and its harmonics.

As the cavity L/D is further increased to 8 and 10, there is a marked change in the oscillation modes that are present. The $\Delta St = 0.0065$ and $\Delta St = 0.0069$ constant bandwidth pressure spectra are shown in Figures 4.12 and Figure 4.13 respectively. In Figure 4.12, it can be seen that only the higher Rossiter modes 3 and 4 are present. The Strouhal numbers are 0.53 and 0.79 respectively. The difference among the mode amplitudes at $L/D = 8$ is much lower than at L/D =2, 4 and 5. At $L/D = 8$, mode 3 is only 5.3 dB higher than mode

4. It is not possible to conclude which mode is dominant as the mode relative amplitude may be time-dependent. However, with the existence of the sub-harmonic ($St = 0.26$) of the Rossiter mode 3 and the higher harmonics at Strouhal numbers of 1.08 and 1.34, it is plausible to infer that the preferred shear layer oscillation in this case is the Rossiter mode 3 with its harmonics. In the $L/D = 10$ case, only one Rossiter mode is observed, as shown in Figure 4.13. It can be seen that the Rossiter mode 2 is observed at a Strouhal number of 0.32 with an amplitude of 150.2 dB. In this case, the higher harmonics at Strouhal numbers of 0.65, 0.98 and 1.3 are also noticeable. Although the Rossiter mode 2 appears to be the overall dominant mode, the harmonics are very close in magnitude to the Rossiter mode 2. The third harmonic is only 11.4 dB lower than the fundamental mode. The two middle harmonics 2.4 dB lower than the fundamental. It is possible that any of these three modes could exist at any given time during the shear layer oscillation, or indeed, co-exist with one another during the oscillation cycle of the shear layer. An example of such mode staging is reported in [83], while an introduction to the mechanisms behind the mode selection in cavity flows is given by Colonius [84].

4.5.3 2D unsteady flow phenomena

In section 4.5.2 the cavity oscillation modes were investigated through the predicted unsteady pressure history at the cavity floor. Although the pressure spectra indicated that some modes were dominant in amplitude, they did not provide a complete insight into the unsteady flow field that is responsible for their generation. The nature of the flow in the vicinity of the cavity opening may be better understood by examining sequences of Favre averaged vorticity and dilatation contours. The vorticity Ω is defined in equation (2.21)and dilatation Θ where $\Theta = \partial u_j/\partial x_j$. Ω and Θ are non-dimensionalised with respect to the cavity length L and the freestream velocity U_∞. The dilatation contours are superposed onto the vorticity colourmaps to give a better insight into the evolution of the aerodynamic field coupled with the acoustic near-field.

Examining the instantaneous snapshots corresponding to approximately one period of

the fundamental mode for the $L/D = 2$ cavity indicates that the flow is dominated by the time-dependent vortex shedding in the shear layer spanning the mouth of the cavity. This is shown in Figure 4.14. The inflow boundary layer separates at the cavity leading edge forming the shear layer. The Kelvin-Helmholtz type instabilities grow as the shear layer develops further downstream eventually leading to the roll-up of convecting vortices. These vortices then impinge on the cavity trailing edge creating disturbances that propagate to the upstream cavity edge where the shear layer is receptive to them. Further vortices are shed and thus a feedback loop is formed. In Figure 4.14(a), corresponding to the quarter period of the fundamental mode, it can be seen that a vortical structure is formed just downstream of the cavity leading edge. At the same time, another structure impinged on the cavity trailing edge and was partially swept back inside the cavity, while part of it spilled over the trailing edge corner. There is only one main convecting vortex in the shear layer, corresponding to the Rossiter mode 1. At half-period of the oscillation mode, shown in Figure 4.14(b), the vortex that was formed at the cavity leading edge has now moved downstream at $x/L = 0.3$ in the shear layer and is convecting towards the cavity trailing edge. This is consistent to the Rossiter mode 2, where two vortical structures are present in the shear layer. At the three-quarter period, as seen in Figure 4.14(c), the convecting vortex has reached the aft cavity corner and is clipped. Most of the vortex is swept downwards in the cavity. At the end of this oscillation period, as depicted in Figure 4.14(d), only one vortical structure is present in the shear layer. Therefore, within one oscillation cycle, there is evidence to suggest that two modes are present, in agreement with the pressure spectrum predictions of Figure 4.9. While the shear layer undergoes an oscillation cycle, the flow inside the cavity is seen to interact with the grazing flow in a complex manner where different structures of disparate scales are present, especially when a vortical structure impinges on the cavity trailing edge.

As shown in the vorticity snapshots, the nature of the vortex-edge interaction at the aft corner is complex. Rockwell and Knisely [34, 85] studied this phenomenon and devised a specific terminology to classify different vortex-edge interaction regimes. 'Complete-clipping' occurs when most of the incident vortex is swept downwards inside the cavity.

opposite to a 'complete-clipping', the 'escape' of vortices occurs when the vortex retains most of its integrity and is allowed to progress downstream. As observed in the vorticity contours, the vortex-edge interaction for $L/D = 2$ and $M_\infty = 0.5$ is actually that of 'complete-clipping', where some of the incident vortex is swept downwards inside the cavity. The characteristics of the mean flow pattern was described in section 4.5.1, where for this cavity geometry, a dominant clockwise structure is shown to occupy the majority of the cavity volume. The source of this re-circulation pattern is therefore linked to the fact that the convectively amplified shear layer vortices are constantly swept back inside the cavity, as shown in Figure 4.14.

The vorticity colourmaps and the dilatation contours for the $L/D = 4$ cavity model are shown in Figure 4.15. The impingement of one vortical structure on the cavity trailing edge is observed at the quarter oscillation cycle. The interaction of the vortex with the aft cavity edge is different from the $L/D = 2$ case, where the vortex was completely clipped. In the present case, the vortex structure is seen to be 'partially clipped' by aft cavity edge [34]. There is only one structure in the shear layer at that instant in time, therefore, the oscillation mode described in Figure 4.15 corresponds to the Rossiter mode 1. At the half oscillation cycle shown in Figure 4.15(b), the roll-up and amplification of another vortical structure is observed. Again, only one vortical structure is present, corresponding to the Rossiter mode 1. At the three-quarter cycle shown in Figure 4.15(c), a significant upward deflection of the shear layer is seen at $x/L \approx 0.5$, $y/L \approx 0$. At the end of the cycle, Figure 4.15(d), a well defined convecting vortex is approaching the cavity trailing edge at $x/L = 0.8$ and the vorticity at the cavity leading edge shows the onset of a new shed vortex. In Figure 4.15(d), there are therefore two vortical structures in the shear layer, where one is formed at the cavity leading edge and the other in the process of being convected by the mean flow towards the cavity downstream edge. This is indicative of a Rossiter mode 2 type of oscillation. Therefore, within one cycle of the shear layer oscillation, two modes corresponding to the Rossiter modes 1 and 2 are observed. The co-existence of two different modes is therefore also observed in this case. The size of the discrete vortices that are shed from the cavity leading edge is large compared to teh

enclosure dimensions. The instabilities in the shear layer originating from the boundary layer separation undergo a rapid amplification to an extent that the resulting vortex is larger than the cavity depth. In Figure 4.15, the vortex-edge interaction is clearly depicted by the vorticity contours. Part of the vortex spills out of the cavity and a little portion is swept inside. This phenomenon is described as 'partial-clipping' as stated by Rockwell and Knisely [34]. In this case, the cavity geometry was classed as transitional. Thus, from the open to transitional cavity, the interaction of the vortical structures with the aft cavity edge changes from 'complete-clipping' to 'partial-clipping'. The 'partial-clipping' is indicative of a greater vorticity strain rate at the cavity trailing edge, as the vortex splits between the convecting component over the downstream bulkhead and a downwards component that is swept towards the main enclosure re-circulation. Such a strain rate is an effective source of sound, according to the acoustic analogy formulation by Proudman [86]. This explains the higher sound pressure levels observed in the spectrum for the $L/D = 4$ cavity as depicted in Figure 4.10.

The flow regime in the $L/D = 5$ cavity is transitional. The instantaneous flow features in Figure 4.16 display much resemblance to the $L/D = 4$ cavity. However, the predicted frequency and amplitude of the Rossiter mode 1 are lower than at $L/D = 4$. The vorticity colourmaps at the three-quarter cycle of the shear layer oscillation in Figure 4.16(c), show the extent to which the vortical structure is clipped by the aft cavity edge is less than in the $L/D = 4$ case. Moreover, only one vortical structure is seen in the shear layer at any instant in time, which is consistent with a Rossiter mode 1 oscillation. Although mode 3 was present in the $x/L = 0.5$ cavity floor pressure spectrum for this case, the spatial resolution used to produce Figure 4.16 was not high enough to show this feature. Specifically, the limits in the size of the graphical output that could be included in this thesis lead to the use of a lower spatial resolution with respect to the CFD solver for generating Figure 4.16. No other mode of the shear layer oscillation can be inferred from the vorticity contours. Through a 25% increase of the L/D, the vortex-trailing edge interaction is reduced, thus giving a lower cavity floor pressure fluctuation amplitude compared to the $L/D = 4$ case.

For the closed cavity flow regime corresponding to the $L/D = 8$ and $L/D = 10$ cases, the nature of the unsteady vorticity field is different to that of the transitional cases, as shown in Figures 4.17 and 4.18. Both cases are characterized by large scale vortex shedding. The characteristic dimension of the discrete vortices shed from the cavity upstream edge is comparable to the cavity depth. The main difference between the closed regime and transitional cavity flow is in the nature of the interaction between the vortical structures and the downstream cavity edge. Figure 4.17 shows one cycle of the shear layer oscillation. In Figure 4.17(d), the vortical structure completely 'escapes' the cavity opening with only a modest interaction with the aft cavity edge. The mean flow pattern seen in Figure 4.7 shows a significant up-turn towards the aft cavity edge, signifying a strong pressure gradient towards the rear end of the cavity. In the time-dependent flow field, the shear layer vortices follow the time-mean flow up-turn near the cavity downstream edge, where the vortices are ejected out of the cavity without significant interaction with the aft edge. In the $L/D = 10$ case, the mean flow pattern up-turns even more than at $L/D = 8$ and the cavity floor time-averaged static pressure distribution describes an even stronger positive gradient towards the rear end. Thus in this case, the vortices are ejected to a higher distance from the aft edge, as shown in Figure 4.18(a). In this case, the interaction with edge is lower than in the $L/D = 8$ case. This feature is also observed in the pressure spectrum for the $L/D = 10$ case, Figure 4.13, where the unsteady pressure amplitude was found to be lower than in the $L/D = 8$ case. Thus in increasing the L/D, the nature of the vortex-edge interaction changes from 'complete-clipping' to full 'escape', giving rise to the lower sound pressure levels predicted in the spectra of the cavity floor pressure.

4.6 2D Cavity Acoustic Radiation

The acoustic field can be visualized through the instantaneous dilatation field. In a low Mach number flow, provided the acoustic perturbations are of small amplitudes, the dilatation field corresponds to the rate of change of density of the fluid, which is related to the propagation of acoustic waves. Whereas the Mach number is higher than the one

that allows a simple correspondence between the dilatation and the rate of change of density to be made, such a relationship is sufficiently strong away from cavity immediate neighbourhood to interpret the dilatation contours as the acoustic pressure field signature.

There are several ways in which the far-field characteristics of the sound field may be determined. Conceptually, the most obvious of those is to extend the computational domain of the region of interest and solve the Navier-Stokes equations throughout the domain. However, this practice is computationally expensive. Away from the source region, the flow variables satisfy a reduced form of the governing equations. A more feasible alternative therefore is to patch the source region to a secondary region in which an appropriately reduced set of the governing equations is solved. Another approach is to employ an acoustic analogy in which, given an acoustic source distribution, its radiated sound is propagated to the far-field using the appropriate Green's function. This study follows the acoustic analogy approach. Specifically, the far-field cavity flow directivity is estimated by Ashcroft's [87] implementation of the Ffowcs Williams and Hawkings acoustic analogy. This method is detailed in Appendix C.

The post-processing FW-H code takes in the flow variables obtained from the aerodynamic simulations. An integration surface is placed parallel to the freestream flow and is truncated so as that it does not enter the inflow and outflow boundaries which have been treated by a non-reflecting buffer zone boundary condition. In this study, the observer points are located in the far field at 100 cavity lengths ($100L$) from the cavity mouth. The cavity centre point is taken at $x/L = 0.5$, $y/L = 0$ with angular measurements in the counter-clockwise direction going from 0 degrees from the downstream cavity bulkhead to 180 degrees on the upstream cavity bulkhead. The integration surface extends $4.5L$ upstream and downstream of the cavity centre point. Since the FW-H formulation is based on the free-space Green's function, the 3D integration surface is constructed by replicating the 2D data in the spanwise direction with a replication length equal to the cavity length L. The streamwise extent as well as the spanwise extent of the integration will influence the FW-H predictions, as shown in a previous study [88].

In the near-field, the acoustic field for the $L/D = 2$ cavity can be visualized through the dilatation contours as shown in Figure 4.14. It can be seen that the most intense acoustic radiation occurs at the cavity trailing edge whenever a vortical structure interacts with it. This radiation is shown in Figure 4.14(b) corresponding to the half cycle of the oscillation and in Figure 4.14(d) at the end of the cycle. The impingement of the vortical structures on the aft corner thus induces pressure fluctuations which then radiate as acoustic waves. There is a dominant upstream directivity as shown by the dilatation contours. From the FW-H calculation, the far-field acoustic directivity is shown in Figure 4.19. It is observed that at 100 cavity lengths, the sound pressure level tends to peak at an angle of 110 degrees in the upstream direction. The sound pressure level observed at this location is 138.7 dB. Two integration surfaces were employed, at $y/L = 2.0$ and $y/L = 2.5$ respectively. It can be seen that there is about 2 dB discrepancy between the two predictions at $\phi < 20^\circ$ and $\phi > 120^\circ$, which indicates that the effective noise source field, that includes sound refraction, is not fully enclosed by the $y/L = 2.0$ integration surface. In the near-field, pressure fluctuations are of the order of 165.6 dB, thus there is an attenuation of 26.9 dB at a distance of $100L$ from the cavity mouth in the direction of the peak directivity. The FW-H computation therefore confirms the near-field observation that the dominant radiation direction is in the upstream direction.

In Figure 4.15(a), a vortical structure is seen to interact with the downstream cavity edge of the $L/D = 4$, $M_\infty = 0.5$ cavity. At this instant, acoustic waves are emitted from the corner and the directivity in the near-field is again observed to be in the upstream direction. From Figure 4.19, it can be observed that the peak directivity is at 117.2° with a corresponding sound pressure level of 140.5 dB compared to the near-field cavity floor pressure fluctuations which were predicted to be 172.8 dB. An attenuation of about 23.3 dB is predicted at a distance of $100L$ from the cavity mouth. The $L/D = 4$ transitional cavity shows a more pronounced upstream radiation angle compared to the open cavity flow regime as seen in the $L/D = 2$ case. The acoustic source, observed from the dilatation field in both cases, is due to the interaction of the vortices with the aft cavity edge. However, the vortex-edge interaction in the $L/D = 4$ case appears to be more intense. As

the characteristic dimension of the vortical structure in the $L/D = 4$ case is comparable to the cavity depth, the induced pressure fluctuations on the cavity trailing edge solid surfaces are likely to be stronger than at $L/D = 2$. This matches with to the higher far-field sound pressure levels observed for this case. The $L/D = 5$ cavity, which also corresponds to a transitional flow regime, displays similar acoustic radiation patterns to the $L/D = 4$ case. In the near-field, the acoustic source is again seen to be due to the interaction of the vortical structures with the aft cavity edge. This is shown in Figure 4.16(c), where an acoustic emission can be observed from the downstream cavity edge where the vortex structure impinges on the solid corner. In the far-field, the directivity peaks at 115.4°, where the sound pressure level is 139.1 dB, as shown in Figure 4.19. The far-field noise amplitude is slightly lower than in the $L/D = 4$ case over the range $20° \leq \phi \leq 160°$, and is possibly due to the fact that the vortices tend to impinge less on the downstream cavity edge. In the near-field, the pressure fluctuations were found to be 171.8 dB in magnitude. An attenuation of 32 dB is observed at a distance of $100L$ from the cavity mouth. The far-field sound pressure for the $L/D = 4$ at the peak directivity angle is 1.4 dB higher than for the $L/D = 5$ case. This agrees with the near-field pressure fluctuations which were found to be 1 dB higher for the $L/D = 4$ case.

The dilatation contours for the $L/D = 8$ cavity are shown in Figure 4.17. The nature of the vortex-edge interaction at $L/D = 8$ is that of an 'escape' of vortices past the downstream cavity edge. When a vortex passes over the cavity trailing edge, as shown in Figure 4.17(a), acoustic waves are generated. In this case, although the vortex does not directly impinge on the solid corner, fluctuating pressures are still induced due to the sharp velocity gradients caused by the convection of vortices over the downstream edge. At the end of the oscillation cycle, Figure 4.17(d), this acoustic source is observed again. The dilatation contours show that the acoustic waves have a predominant radiation angle in the upstream direction. The FW-H calculation to predict the far-field sound signature is shown in Figure 4.19. It can be seen that the dominant directivity is at 123.1° with a sound pressure level of 132.1 dB. Thus the directivity is more pronounced in the upstream direction than in the closed and transitional cavity simulations. The attenuation in the un-

steady pressure amplitude at a distance of $100L$ is 36.1 dB for $L/D = 8$. There are several peaks and troughs in the far-field directivity as seen in Figure 4.19, indicating that there is also a component of acoustic radiation in the downstream direction.

The directivity shown in Figure 4.18 for the $L/D = 10$ cavity is qualitatively similar to that of the $L/D = 8$ case. The major source is again observed to be due to the convection of the vortical structures over the sharp aft cavity edge as seen in Figure 4.18(a) and Figure 4.18(d). Most of the sound power is again directed in the upstream direction. The peak directivity is observed to be at an angle of 119.8°. The sound pressure level at this angle is 134.2 dB which is higher than the peak directivity at $L/D = 8$. This is slightly in contradiction to the near-field observations where the pressure fluctuations for the $L/D = 10$ cavity were found to be 2.1 dB lower than in the $L/D = 8$ case. This could be attributed to the higher sensitivity of the placement of the FW-H integration surfaces in the $L/D = 8$ case, thus making the FW-H calculation less reliable for this test case.

4.7 Summary

In this chapter, various 2D cavity configurations were studied under the same inflow conditions. The computed oscillation frequencies agree well with the values predicted by the Rossiter model. The amplitudes of the modes are dependent on the vortex-edge interaction. The presence of Rossiter modes in the cavity oscillations tends to indicate that a feedback mechanism is present.

The vortex-edge interaction is in accordance to that observed in past experiments [34]. In both the $L/D = 2$ and $L/D = 4$ cases, the vortex-edge interaction can be described by a 'complete clipping' action, whereas the $L/D = 5$ cavity showed only 'partial clipping'. For the $L/D = 8$ and $L/D = 10$, discrete vortices 'fully escape' the enclosure, having a modest interaction with the solid edge. It is believed from the current study that the intensity of the vortex-edge interaction has a direct effect on the radiated sound amplitude in the far-field.

The far field sound was computed using the Ffwocs-Williams and Hawkings acoustic analogy. It was observed that the far-field directivity changed from the open to closed cavity. The computed far-field sound pressure levels were consistent with the observations in the near-field pressure fluctuation levels. The FW-H method confirmed the observations in the pressure spectra, that the $L/D = 4$ produced the most intense oscillations and the stronger acoustic field. The directivity pattern is therefore dependent on the L/D. A difference of 13° in the orientation of the peak directivity was observed between the open cavity and the closed cavity.

4.8 Chapter 4 Figures

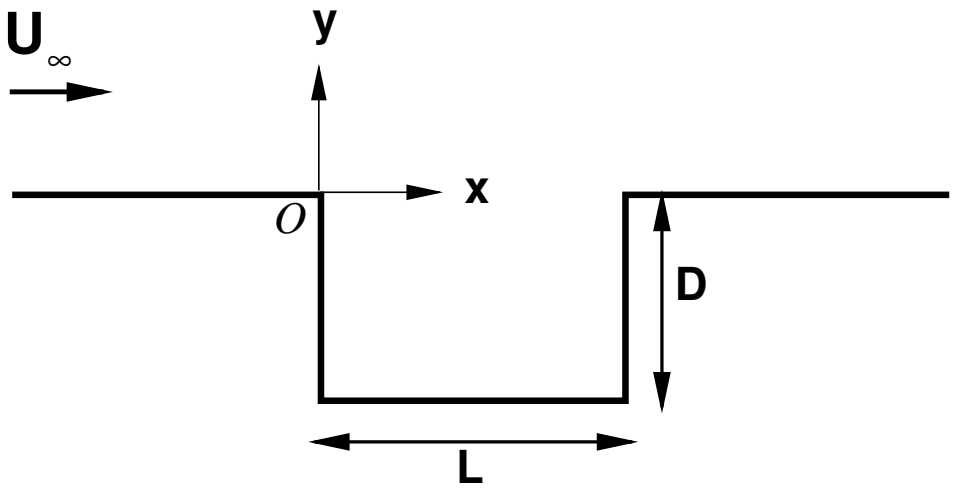

Figure 4.1: 2D cavity geometry.

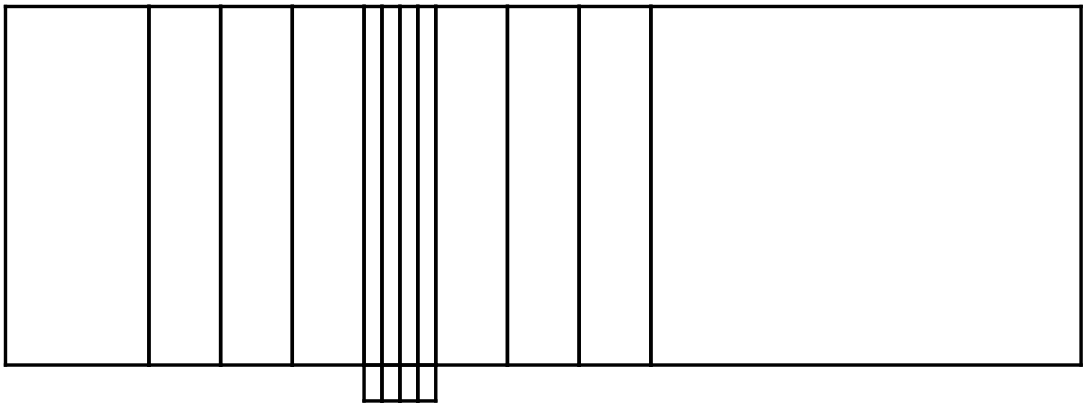

Figure 4.2: Typical computational domain, with 574,000 cells. Flow from left to right.

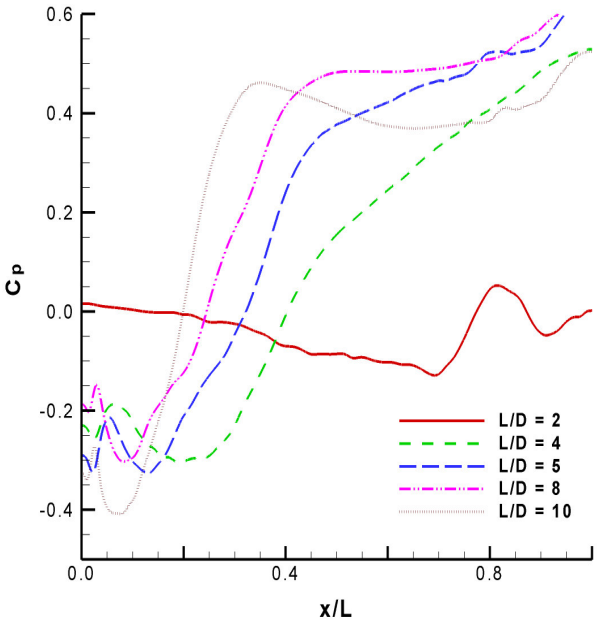

Figure 4.3: Static pressure distribution along the cavity floor at $M_\infty = 0.5$.

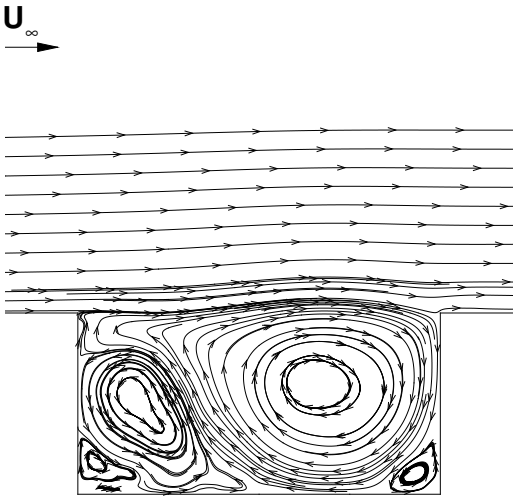

Figure 4.4: Time-averaged streamline patterns; $L/D = 2$, $M_\infty = 0.5$.

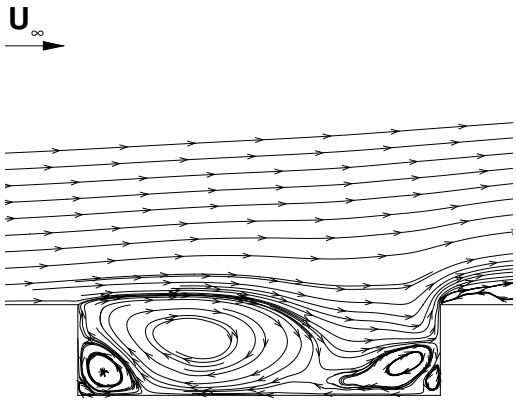

Figure 4.5: Time-averaged streamline patterns; $L/D = 4,\ M_\infty = 0.5$.

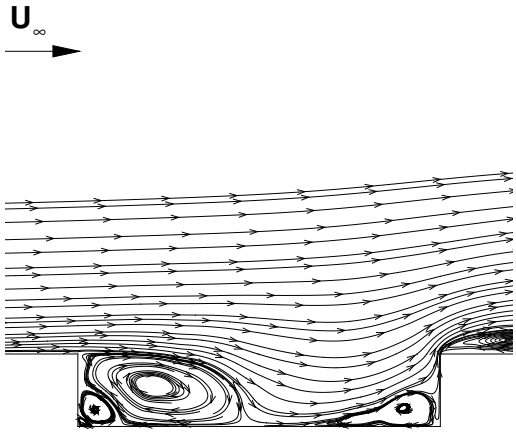

Figure 4.6: Time-averaged streamline patterns; $L/D = 5,\ M_\infty = 0.5$.

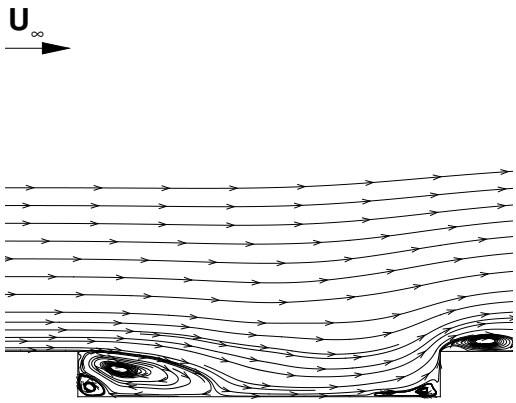

Figure 4.7: Time-averaged streamline patterns; $L/D = 8,\ M_\infty = 0.5$.

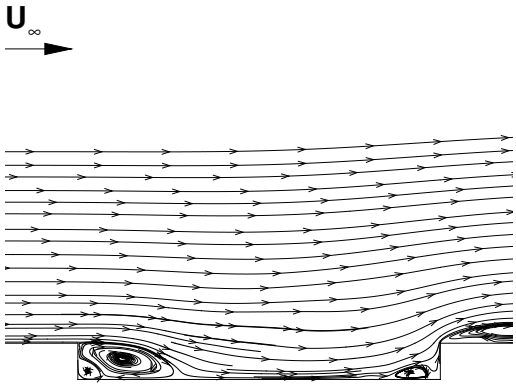

Figure 4.8: Time-averaged streamline patterns; $L/D = 10,\ M_\infty = 0.5$.

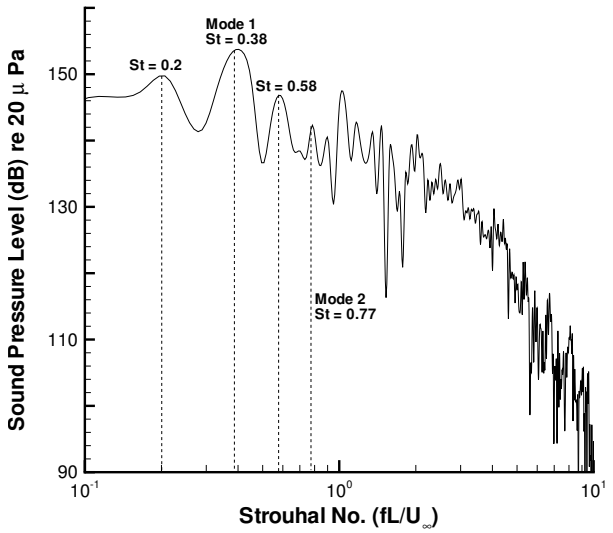

Figure 4.9: Sound Pressure Level in dB, $L/D = 2,\ x/L = 0.5,\ \Delta St = 0.0025$.

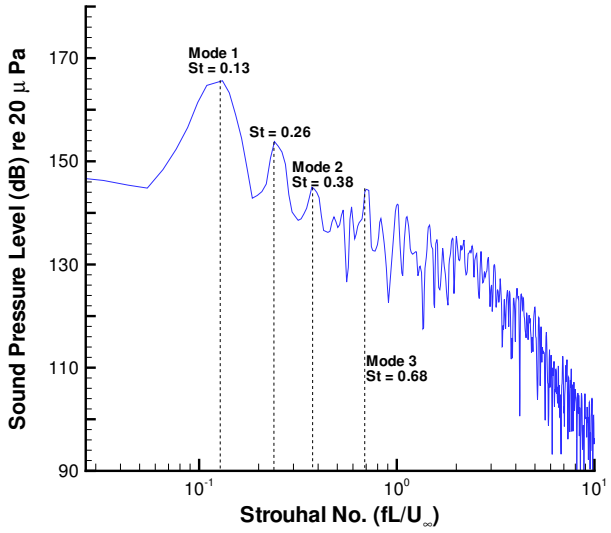

Figure 4.10: Sound Pressure Level in dB $L/D = 4,\ x/L = 0.5,\ \Delta St = 0.0033$.

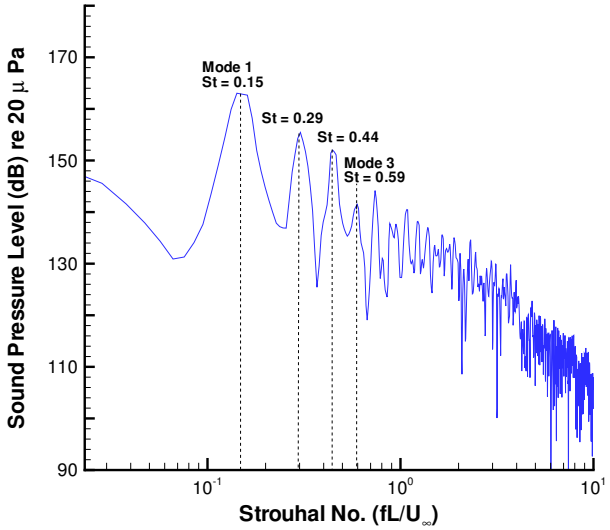

Figure 4.11: Sound Pressure Level in dB $L/D = 5,\ x/L = 0.5,\ \Delta St = 0.0028$.

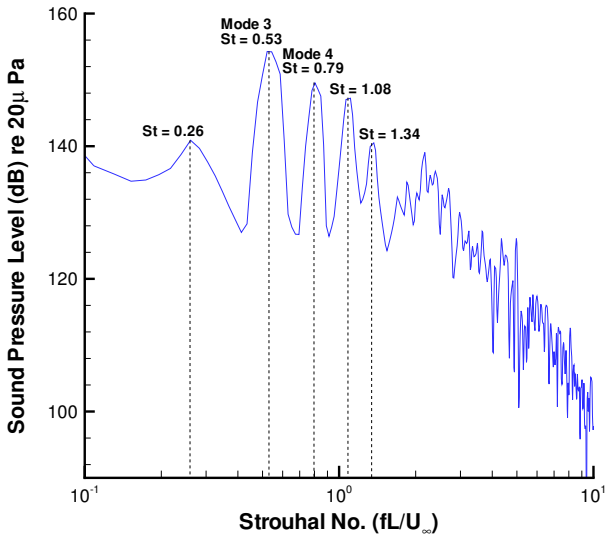

Figure 4.12: Sound Pressure Level in dB $L/D = 8,\ x/L = 0.5,\ \Delta St = 0.0065$.

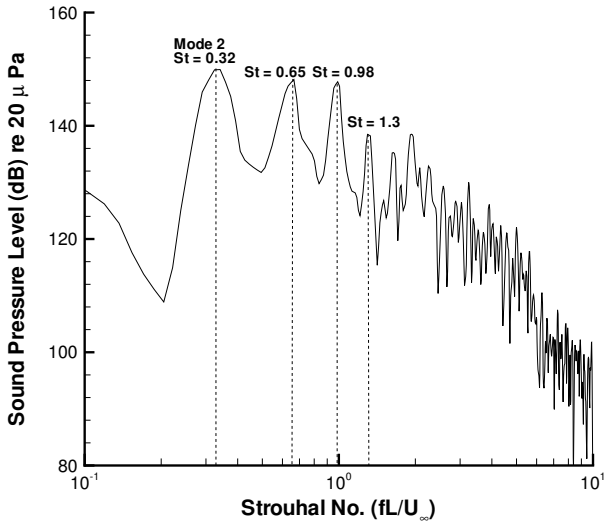

Figure 4.13: Sound Pressure Level in dB $L/D = 10,\ x/L = 0.5,\ \Delta St = 0.0069$.

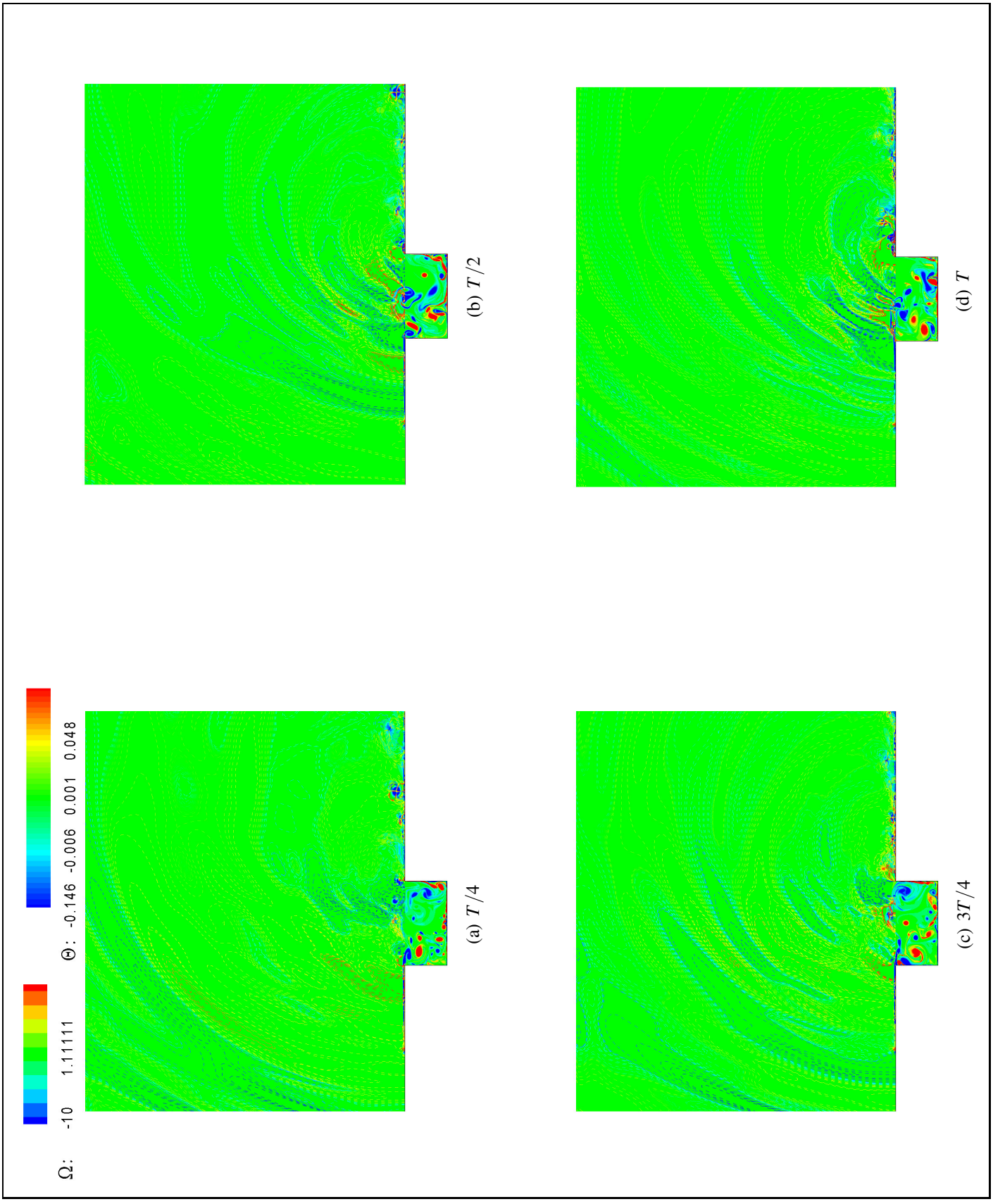

Figure 4.14: Instantaneous non-dimensional vorticity Ω and dilatation (dashed lines) Θ; $L/D = 2$, $M_\infty = 0.5$.

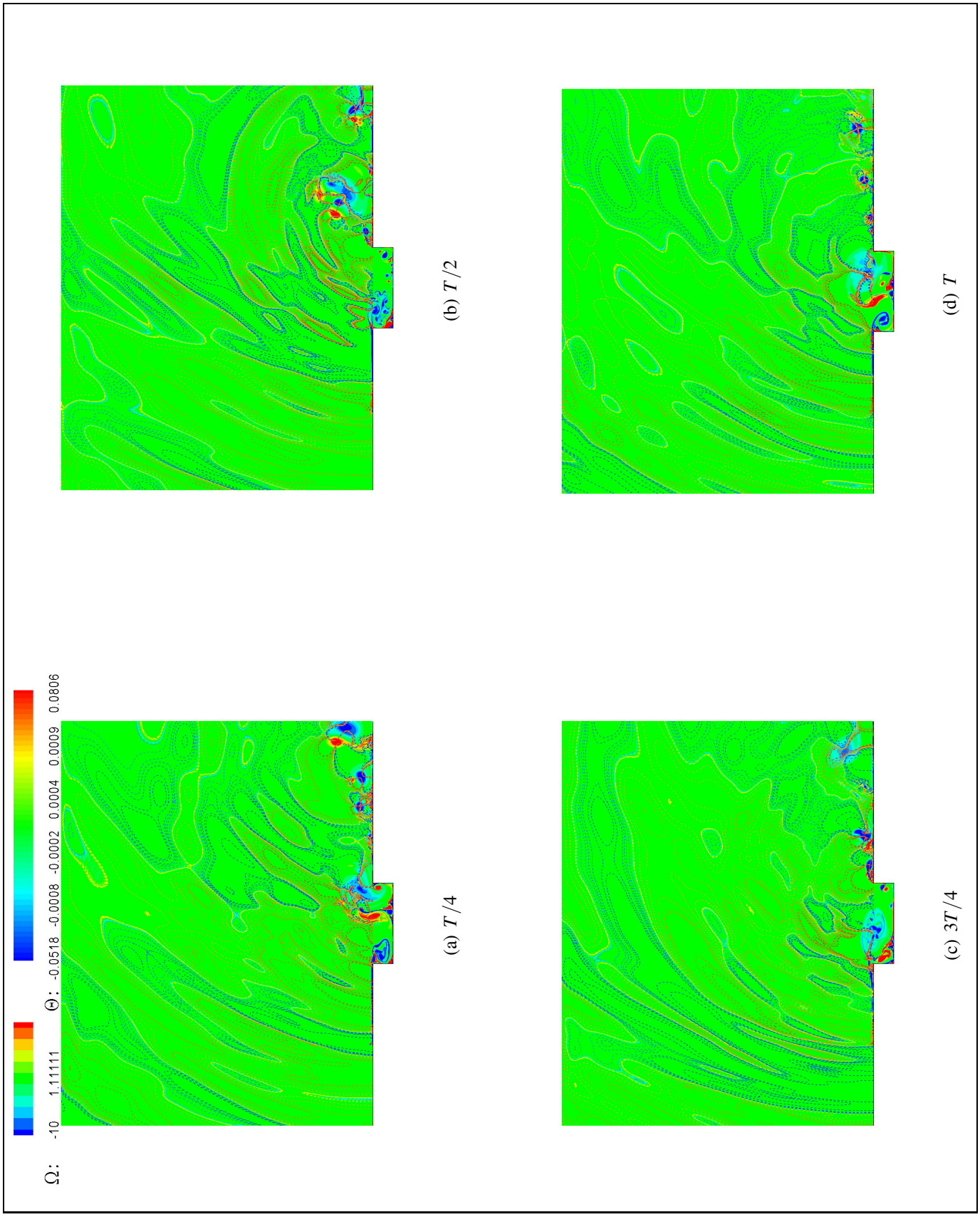

Figure 4.15: Instantaneous non-dimensional vorticity Ω and dilatation (dashed lines) Θ; $L/D = 4$, $M_\infty = 0.5$.

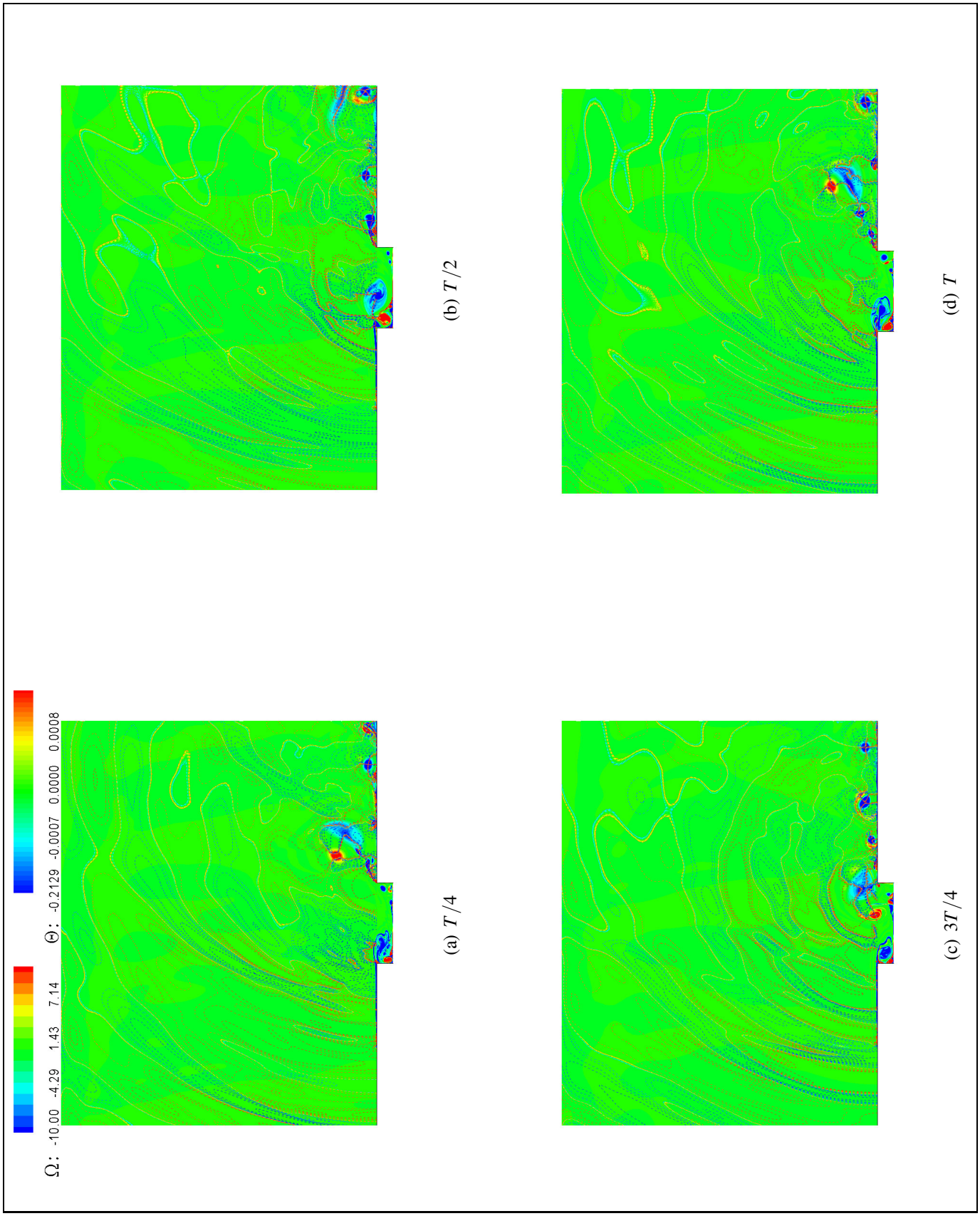

Figure 4.16: Instantaneous non-dimensional vorticity Ω and dilatation (dashed lines) Θ; $L/D = 5$, $M_\infty = 0.5$.

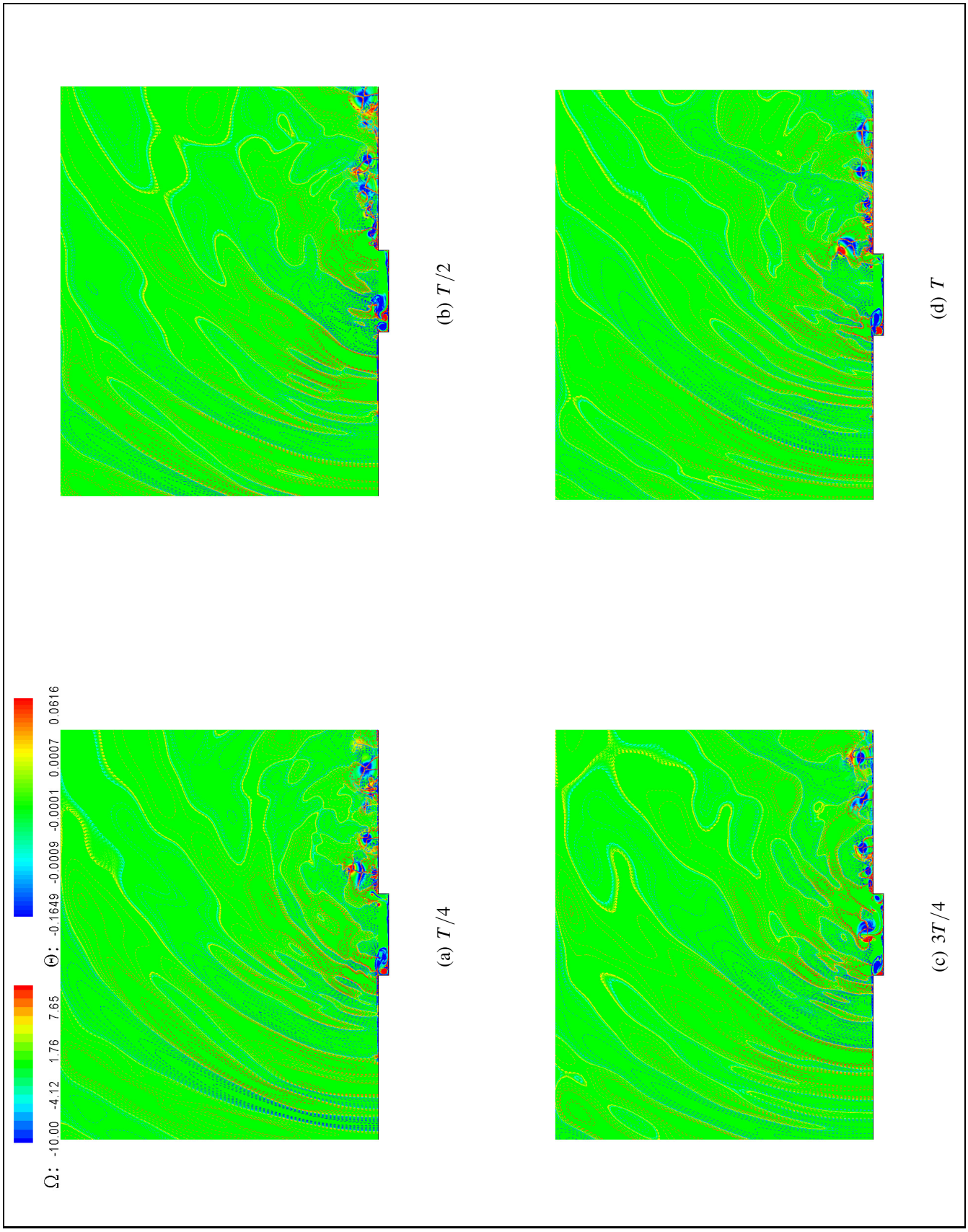

(a) $T/4$ (b) $T/2$ (c) $3T/4$ (d) T

Figure 4.17: Instantaneous non-dimensional vorticity Ω and dilatation (dashed lines) Θ; $L/D = 8$, $M_\infty = 0.5$.

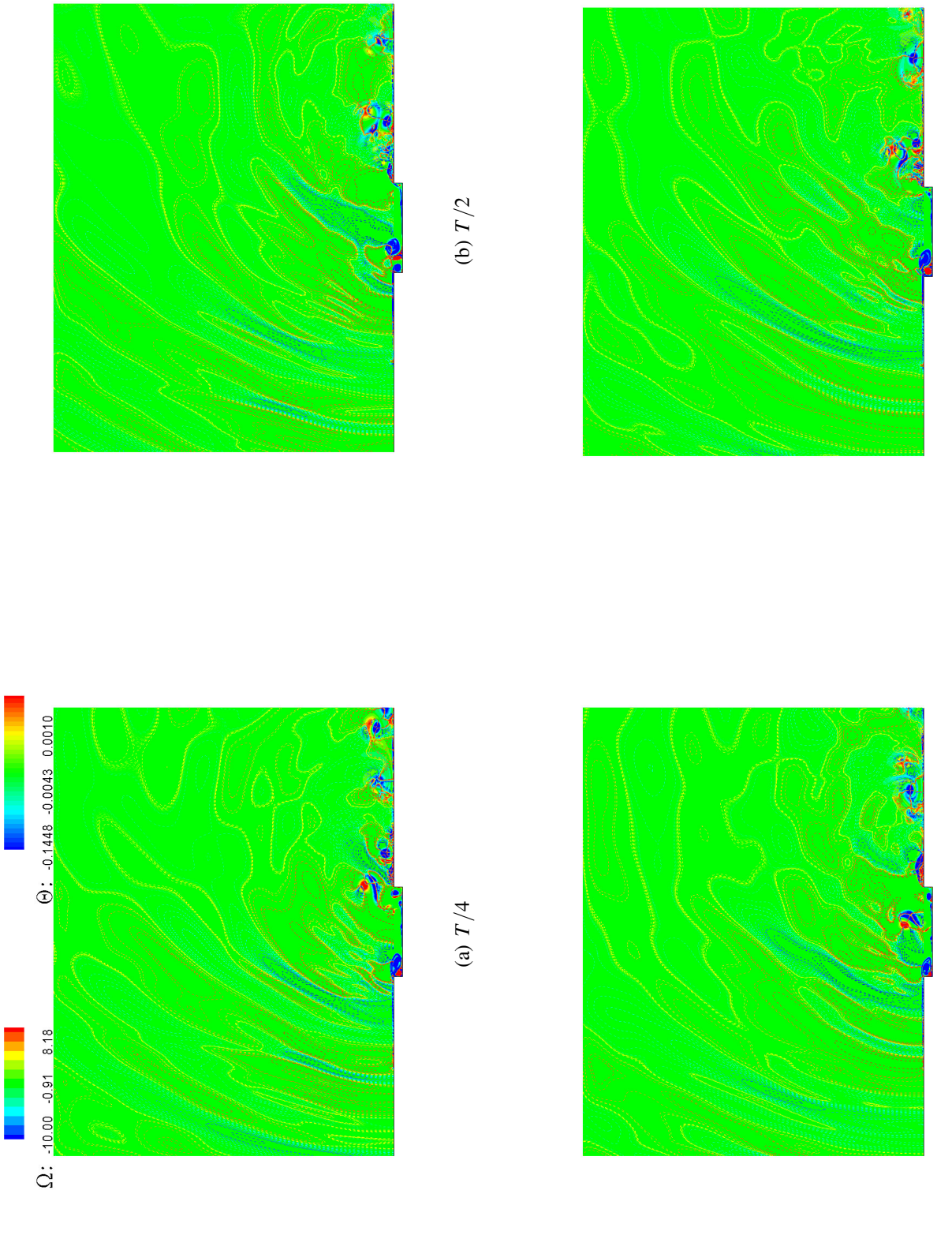

Figure 4.18: Instantaneous non-dimensional vorticity Ω and dilatation (dashed lines) Θ; $L/D = 10$, $M_\infty = 0.5$.

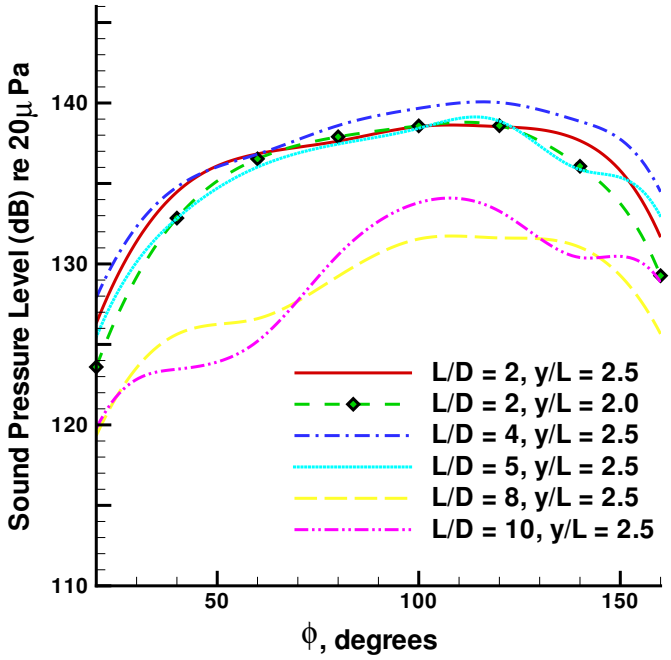

Figure 4.19: Far-field sound pressure level and directivity for varying L/D; $M_\infty = 0.5$.

Chapter 5

Three-Dimensional Cavity Flow Investigation with PIV

5.1 Overview

An experimental study of the low speed flow over 3D cavity geometries was conducted using the Particle Image Velocimetry (PIV) technique. The objective of the experiments was to obtain a detailed view of the flow topology inside 3D cavities. The cavity had a constant $L/D = 4$ and the width-to-depth was varied from 0.5 to 3. Surface oil flow visualizations were also performed on these geometries to complement the PIV measurements.

5.2 Introduction

The experimental work by Roshko [9] in 1955 constituted the first major investigation into cavity flow physics and subsequent noise radiation. In particular, the author highlighted the importance of the geometrical parameters on the mean-flow. For shallow cavities at

low Mach numbers, a main vortical structure with secondary re-circulating regions in the corner (Moffatt eddies) was observed.

In 1963, Maull and East [12] performed experiments to demonstrate the 3D nature of the flow inside rectangular and circular cavities. Cellular re-circulating structures were observed for certain cavity widths. It was concluded that the existence of these structures and the number of cells are directly related to the size of the primary vortical structure in the streamwise direction.

The seminal work by Maull and East highlighted the important three-dimensionality of the flowfield in cavities of large spans. However, there remains a poor account of the flow topology, thereby explaining the motivation behind the current initiative. Using modern experimental techniques, such as PIV, this study aims to further improve the understanding behind the nature of 3D cavity flows.

5.2.1 Test facilities and experimental set up

All the measurements were acquired in the University of Southampton's low speed 2.1m x 1.5m wind tunnel. The 2.1m x 1.5m tunnel is a closed circuit return wind tunnel with a contraction ratio of 5:1. An axial fan drives the flow through the tunnel and a series of meshes are used to homogenize the flow. The freestream turbulence intensity level of the facility was quantified at 0.3% for a flow speed of 30 m/s. In the present study, the wind tunnel fan rotational speed was set such that freestream velocities of 10m/s, 20m/s and 30m/s were obtained.

A cavity model was mounted above the wind tunnel floor via the four supporting legs. The presence of the legs below the cavity model creates a blockage effect, giving an adverse pressure gradient. Therefore the model was tilted by -2.3 degrees such that a zero pressure gradient is achieved above the cavity. The length of the cavity model is 200mm and the depth 50mm. The upstream cavity bulkhead is 265mm long and a Carborundum grit trip is placed at 20mm from its leading edge to ensure that the boundary layer is fully turbulent

before it reaches the cavity leading edge. The whole upper surface is of smooth aluminium painted with gloss black paint. This procedure ensures that surface roughness effects on the boundary layer are minimized. The boundary layer characteristics were measured in a previous study by Ashcroft [87], using Laser Doppler Anemometry (LDA). The boundary layer thickness, δ, measured at $x/D =$ -0.2, is 6.23 mm. The displacement thickness (δ^*) and momentum thickness (θ) are 1.07 mm and 0.77 mm respectively. The shape factor, H, is 1.39.

A 3 views drawing of the cavity model is shown in Figure 5.1. The original model span was 900mm, giving an overall W/D of 18. In this study, the span is restricted by the means of blocks introduced at both spanwise ends. This procedure was also employed by Maull and East [12]. Schematics in Figures 5.2 and 5.3 show the Cartesian reference system used in the cavity flow measurements.

5.2.2 Particle image velocimetry (PIV)

PIV is a non-intrusive technique for obtaining the instantaneous velocity field distribution over a finite planar area. PIV measures the distance traveled by particles in the flow within a known time interval, Δt. The flow is seeded in order to detect the movement of the seed particles, which are photographed by flashing them with a light pulsed laser sheet.

A CCD (Charged Coupled Device) camera is positioned at right angles to the laser light sheet to record the position of the illuminated seed particles. Camera images are synchronized with the light pulses such that the positions of the particles are recorded on two different frames at a short time interval, Δt, apart. A Dantec PIV system was employed, consisting of a Flowmap 1100 Processor, a Gemini PIV 15 Nd:YAG laser (class 4, 120mJ and wavelength 532 nm) and a Dantec HiSense camera (type 13 gain 4) which produces images of 1290 x 1024 pixels resolution. The flow was seeded with smoke particles of $0.1 - 5\mu m$ in diameter. The use of a single camera allows the measurement of velocity components in 2D planes, i.e. in the plane of the laser sheet. To minimize errors due to

optical effects, it was essential that the camera plane and the laser plane remained orthogonal to each other. To investigate the cavity 3D flowfield the velocity distribution was measured on several 2D planes. Figure 5.4 shows a schematic of the camera and laser arrangement in the wind tunnel.

At a sampling rate of $2Hz$, the mean-flow was obtained by averaging over 500 instantaneous datasets measured in batches of 250. Within one run some instantaneous datasets contained little or no noise while others contained a high noise level. The variation of the data quality within one run is thought to vary due to several factors. First the quality of the acquisition depends on the level of seeding in the flow, as too little or too much seeding was found to have a negative effect on the data quality. It is important that a trial run is carried out before acquiring the data to make sure that an optimal level of seeding is reached. The second factor affecting the PIV results is the timing between image pairs, which in this study, was $10\mu s$. The positions of the illuminated particles on each image pair are cross-correlated to identify the position shift between the two images. For the cross-correlation purposes, the Dantec Flowmanager software provided a number of options, namely the resolution of the vector map desired. It was found through trial and error that a cross-correlation window of 32 x 32 pixels was the optimal setting and contained the least level of noise. This setting was therefore chosen for post-processing the majority of the raw images. A third factor that affects the PIV results is the amount of stray reflection inside the wind tunnel from the laser sheet pulses. Reflections off sharp edges and shiny surfaces have to be minimized so that they do not introduce spurious light around the area under investigation. This was done by using gloss black paint on the model surfaces.

5.2.3 Surface oil flow visualization

A thin layer of a titanium dioxide and paraffin oil mixture was applied on all the cavity surfaces and the wind tunnel was run at a constant freestream speed for several minutes for the oil to evaporate. As the oil evaporates, the titanium dioxide particles are displayed

by the oil streaks, driven by the shear stress that the flow exerts on it. The particles left after the oil has evaporated mark the direction of the oil streaks. The oil streaking speed is very slow compared to the flow speed, as it takes several minutes for the oil pattern to form. This means that the titanium dioxide left behind displays the oil streaklines that are the footprint of the time-averaged flow streamlines close to the surface. Due to the slow reaction time of the oil, this visualisation technique gives a qualitative record of the near-surface time-mean flow. It is a very useful tool to locate and identify complex time-mean flow features.

5.3 Time Averaged Flow

5.3.1 Surface oil flow results

The flow speed was set at 30 m/s and surface oil flow visualisations were obtained at W/D =0.5, 1, 1.5, 2 and 3. The results in Figures 5.5 to 5.9 show a flow inside and around the cavity that is highly three-dimensional. The surface flow inside the cavity is shown in an unfolded view, whereby the cavity surfaces have been dismantled displaying each surface on a plane. For such complex flows, it is convenient to describe the flow patterns through basic fluid motions as described by Chong *et al* [89]. Time averaged flows, no matter how complex, can be reduced to the basic flow patterns in the vicinity of an observer moving along a streamline. The basic patterns comprise of critical points and bifurcation lines in the near-surface flow. The overall topology is largely dictated by a combination of these patterns. Critical points occur where the flow velocity is zero and the streamline slope is indeterminate. These points can be nodes, saddles or focal points respectively. Bifurcation lines are formed when the neighbouring streamlines move apart from one another. Negative bifurcation lines are formed where the oil streaks coalesce, indicating an upwash of the time-mean flow away from the surface. A topological understanding of the flow structure inside 3D cavities will thus be attempted through the identification and classification of the critical points and bifurcation lines in Figures 5.5

to 5.9. In the following paragraphs where each cavity case will be described, node points will be marked as 'N', saddle points as 'S' and focal points as 'F'. Bifurcation lines will be highlighted wherever they are observed in the flow patterns. Detailed explanations on the nature of node, saddle and focal points is given by Perry and Chong [90].

Figure 5.5 corresponds to the cavity of $W/D = 3$, which is the widest cavity configuration studied herein. This configuration is taken as the baseline case. On the cavity floor, the oil flow depicts a well-defined re-circulation region comprising of two cellular structures. For this case, a quasi symmetrical behaviour about the centreline is evident and the oil streaklines show two counter rotating regions downstream of the cavity front wall marked as Cell 1 and Cell 2. The centres of these cellular structures are focal points, where Cell 1 is a clockwise spiral and Cell 2 a counter-clockwise spiral. The PIV presented later on shows that the flow is spiralling around Cell 1 and Cell 2. This spiralling can be hypothesized to be an indication of the presence of vortex stretching in the direction normal to the cavity floor. Upstream of the cellular structures, a saddle point divides the flow along the cavity centreline. For a flow with a pure rate of strain, the saddle point would be orthogonal. However, in the present case, the saddle point is deformed indicating that a rate of rotation is also present, but the rate of strain is still dominant. A pair of bifurcation lines exists to the left and right of the saddle point. The bifurcation lines are created as the spirals attract fluid towards the focal points. The oil streaks are seen to asymptote towards the bifurcation line hence giving a negative bifurcation. The combination of focal points, saddle point and bifurcation lines give a kidney shaped flow pattern on the cavity floor. The surface flow patterns on the cavity front and rear walls are also shown in Figure 5.5. No identifiable pattern can be seen on the front walls. However, near the corner between the rear wall and the cavity floor, a separation line can be seen which spans the entire width of the cavity. The separation line is a positive bifurcation line where the oil streaks are seen to diverge on either side. The presence of such a line indicates that a secondary vortical structure is present at the rear corner of the cavity. Slightly aft of the trailing edge, a separation bubble is present and is shown through a contortion of the oil streaks in the spanwise direction in Figure 5.5. The separation

bubble is formed due to the presence of the 90° edge which causes the flow to separate as the shear layer passes around it and subsequently re-attaches on the surface which follows.

On the left and right side walls, several flow patterns can be identified, namely a bifurcation line and a re-circulating flow region. The bifurcation line is formed due to the interaction between the main streamwise re-circulating flow driven by the cavity shear layer and the physical boundary of the wall on the left and right sides. In this case it can be seen that the bifurcation lines are composed of oil streaklines which diverge away from each other, giving a positive bifurcation structure. A re-circulating flow region can also be identified below the bifurcation line and this indicates that the time-mean flow towards the downstream end is directed into the enclosure, giving a time-mean mass injection along the side walls.

In the oil flow visualisation at $W/D = 2$ shown in Figure 5.6, the time-mean surface flow does not show the same degree of symmetry along the centreline as in the $W/D = 3$ cavity. A main streamwise re-circulating flow region is shown on the front portion of the cavity floor. Two cellular structures make up the re-circulation region and are marked as Cell 1 and Cell 2. The centres of the cells are focal points marked as 'F'. As in the $W/D = 3$ case, Cell 1 is a clockwise rotating structure and Cell 2 is a counter-clockwise rotating structure. In this case however, the two structures are not as easily distinguishable as at $W/D = 3$. The two focal points seem to have a degree of interaction which tends to produce asymmetric re-circulation cells. Downstream of the cellular structures, a node point exists and is marked as 'N' in Figure 5.6. The presence of a node instead of a saddle point as in the $W/D = 3$ case indicates that the rate of rotation of the fluid particles in that region of the cavity increased as the cavity span was reduced. A pair of bifurcation lines is also produced to the left and right of the node as the fluid spirals towards the focal points. The asymptotic behaviour of the streaks around the edge of the spanwise re-circulation is also indicative of the presence of the bifurcation line. The combination of the node, bifurcation lines and focal points give rise to the distorted flow pattern observed in the fore portion of the cavity.

On the rear and side walls of the $W/D = 2$ cavity, the flow patterns observed are similar to those at $W/D = 3$. This is shown in Figure 5.6, where a separation line (positive bifurcation line) is observed at a similar location as in the $W/D = 3$ cavity. On the side walls, the $W/D = 2$ cavity displays similar flow features as at $W/D = 3$, namely, a bifurcation line and a re-circulating flow region.

The unfolded view of the surface oil flow visualisation on the $W/D = 1.5$ is shown in Figure 5.7. A main spanwise re-circulation region is immediately identified in the front portion of the cavity. In contrast to the baseline and $W/D = 2$ cases, only one cellular structure is observed and is marked as Cell 1. The re-circulation of the cell is as described by the PIV results later on, is clockwise. The cell structure is seen to be approximately of the same dimension as the cavity width. The centre of the re-circulation region is a focal point and causes fluid to spiral towards it. The critical point is marked as 'F'. The spiraling effect is seen to produce a bifurcation line at the edge of re-circulation region. The oil streaklines are seen to converge towards each other and thus giving a negative bifurcation. This geometry is in direct contrast to the $W/D = 3$ and $W/D = 2$ cases as no other critical point is present. This is due to the presence of only one focal point in the cellular structure. The presence of a lone focal point indicates that the rate of rotation dominates the flow in this portion of the cavity and that the rate of strain is negligible. This is a direct consequence of a further reduction in the cavity span dimension. As in the previous cases, a separation line is observed near the downstream cavity corner. On the cavity side walls, a bifurcation line and a re-circulating flow region are present, similarly to the $W/D = 3$ and $W/D = 2$ cases.

A surface oil flow visualisation over the $W/D = 1$ cavity is shown in Figure 5.8. As in the $W/D = 1.5$ case, only one cellular structure is observed in the front portion of the cavity. The structure is seen to be of approximately of the same dimension as the cavity width. The re-circulation region comprises of only one cell marked as Cell 1 and is a counter-clockwise rotating structure. The centre of the cell is a focal point marked as F. The presence of only one focal point creates a bifurcation line as fluid spirals towards the critical point. The lone focal point is indicative that the rate of rotation dominates the flow

in fore portion of the cavity and that the rate of strain is again negligible. In contrast to the $W/D = 3$ case, the flow pattern in this case is asymmetrical. At the bottom of the rear cavity wall, the separation line is again noticeable. On the left and right side walls the identifiable flow patterns are a bifurcation line and a re-circulating flow region. The existence of these features follow the same reasoning provided in the baseline configuration.

For the cavity of $W/D = 0.5$, the spanwise re-circulation pattern is still in the front portion of the cavity and comprises of only one cellular structure. The flow in this case is asymmetrical and is similar to the one in $W/D = 1$ case. From the oil flow visualisation in Figure 5.9, other critical points and bifurcation lines are not evident on the cavity floor. A separation (positive bifurcation) line is again observed at the cavity downstream corner. On the left and right side walls the identifiable flow patterns are a bifurcation line and a re-circulating flow region.

Maull and East [12] performed oil flow visualization on 3D cavities with $W/D = 9.5$, 7.5 and 5. The observation was that on reducing the W/D, the flow inside the cavity breaks down into a number of cellular structures forming spanwise re-circulation regions. According to the authors, the effect of reducing the width of the cavity is to change the number of cellular structures present across the cavity span. In the current study, when the W/D was systematically reduced from 3 to 0.5 the number and shape of the cellular structures displayed a similar trend. For the cavities of $W/D = 3$ and 2, two cells were observed whereas the narrower cavities showed only one structure of approximately the same dimension as the width. Therefore, the number of cellular structures is a function of the cavity width. For the larger cavities of $W/D = 3$ and 2, two focal points were present and were separated by another critical point. The nature of this critical point would appear to have a direct effect in determining the flow pattern on the cavity floor. If a saddle point is present as in the $W/D = 3$ case, the re-circulating spanwise cells were quasi-symmetrical. For the $W/D = 2$ case where the cavity width was reduced, the two focal points within the re-circulating flow region tend to interact with each other in a repulsive action thus distorting the spanwise symmetry of the cells. The rate of rotation of fluid particles in those regions thus increases and the saddle point which separates the

two foci becomes a node. Upon a further reduction of the cavity width, only one cellular structure was observed and the narrower cavity width gave just one focal point, no saddle point and no nodal point. Such a behaviour was observed in the flow pattern in the cases of $W/D = 1.5$, 1.0 and 0.5. Thus the flow pattern on the cavity floor is directly related to the number and type of critical points present which in turn is controlled by the cavity width.

5.3.2 Time-averaged velocity measurements

The time-averaged velocity field in the cavity was obtained through an ensemble averaging of the instantaneous PIV images. As this particular investigation was tailored towards acquiring the flow patterns inside the cavity, the shear layer above the cavity was not captured. Velocities in $x-y$ planes at various spanwise positions were measured. PIV data at various $x-z$ planes were also acquired and of particular significance were the y/D = -0.9 planes (horizontal plane 5mm from the cavity base). This provided a means to compare the PIV data against the oil flow visualization. The plane $z/D = 0$ corresponds to the cavity centreline in all cases.

The dominant feature of the mean streamwise flow inside the 3D cavity is a main clockwise re-circulation region as shown in Figures 5.10 to 5.14. This is present in all the cases tested, however as different spanwise planes were measured, a change in the re-circulation centre positions is observed. The re-circulation centre was estimated for each test case as the centroid of the area at the core of the concentric streamlines pattern in Figures 5.10 to 5.14. The positions of these points are summarized in Tables 5.1 to 5.5. Table 5.6 summarizes the positions of the vortex cores in a $W/D = 18$ cavity. It can be seen from these Tables that there is a significant variation of the centres of the re-circulation regions. For the $W/D = 3$ case (in Table 5.1), it is noted that the streamwise coordinate of the centre of rotation changes between the $z/D = 0.0$ and the z/D = -1.25 planes. The net displacement of the vortex core is a maximum of $\Delta x/D = 0.34$ in the streamwise direction at 10 m/s and $\Delta x/D = 0.19$ at 30 m/s. There is also a vertical change in position starting from

the lowest at y/D = -0.58 to y/D = -0.36. The net drift of the core in the flow normal direction is $\Delta y/D = 0.12$ for all flow speeds, as summarized in Table 5.1. For the W/D = 2 cavity, the mean positions of the vortex core are summarized in Table 5.2. The primary vortex core drifts by $\Delta x/D = 0.16$ in the downstream direction between the planes z/D = 0 and z/D = -0.5. Then it drifts in the upstream direction between the planes z/D = -0.5 and z/D = -0.75, where the net change in position is $\Delta x/D$ = -0.18. The vertical change in position of the main vortex centre is always in the flow normal direction and in this case the net drift is on average $\Delta y/D = 0.14$. The mean position of the respective vortex cores for the narrower cavities of W/D = 1.5 and 1.0 is summarized in Tables 5.3 and 5.4. In the case of the $W/D = 1.5$ cavity, the mean movement of the primary vortex core is on average $\Delta x/D = 0.26$ in the downstream direction. The vertical change in position is again in the flow normal direction by $\Delta y/D = 0.12$. The $W/D = 1.0$ cavity displays a net change in position of the vortex core of $\Delta x/D = 0.07$ in the streamwise direction while the flow normal drift is $\Delta y/D = 0.07$.

The mean velocity fields at 30 m/s for the cavities of W/D = 3, 2, 1.5 and 1 are shown in Figures 5.10 to 5.13. As only one plane of data was acquired for the $W/D = 0.5$ cavity corresponding to $z/D = 0$, it is not possible to deduce the spanwise change in position of the primary vortex core. However a comparison of the narrowest cavity investigated i.e. $W/D = 0.5$ with the cavity of $W/D = 18$ (classed as a 2D cavity) is possible. Tables 5.5 and 5.6 indicate the position of the primary vortex cores at the different flow speeds. It can be deduced that for $W/D = 0.5$, the vortex core is located at $x/D = 3.0$ and y/D = -0.44 at 30 m/s. On the other hand for the 2D cavity, the primary vortex core is at x/D = 3.15 and y/D = -0.346 suggesting that the re-circulation centre is closer to the trailing edge at $W/D = 18$. The PIV data for these two cases are shown in Figure 5.14. In all the cases investigated, it was observed that the net movement of the primary vortex core was significant and involved a drift in both horizontal and vertical directions. In general, the streamwise drift decreases as the cavity width is reduced whereas the vertical drift is more or less constant. The presence of the side walls causes a warping of the primary vortex axis corresponding to changes in position of the core as discussed. The

term 'vortex core' was implied loosely in the previous sections. Upon examination of Figures 5.10 to 5.13 it can be seen that the regions referred to are regions of rotating fluid. However, the spiraling nature of the flow around what was referred as the vortex core is evident and the quantitative drifts mentioned are can also be visually observed. The spanwise centres of the re-circulation regions are critical points, namely, focal points (rate of rotation dominates while strain rate is negligible) and the spiraling indicates vortex stretching in the spanwise direction. For the 2D cavity shown in Figure 5.14(b), it can be seen that the sectional streamlines describe well defined concentric patterns (no spiraling effect), which tends to indicate that there is no significant vortex stretching in the spanwise direction and that a focal point is not present as in the 3D cases. This contrast is best shown in Figure 5.14(a) which corresponds to the cavity of $W/D = 0.5$. The focal point and the spiraling fluid is clearly shown. The effects of vortex stretching and additional viscous forces at the cavity side walls drive the warping of the axis of the main streamwise vortical structures inside the cavity.

PIV measurements were also acquired at the plane $y/D =$ -0.9 which corresponds to a horizontal plane 5mm off the cavity floor. The time averaged PIV data acquired at $y/D =$ -0.9 for the various geometries considered are qualitatively compared against the oil flow results of Section 5.3.1. Figure 5.15(a) shows two mean spanwise re-circulation patterns near the the cavity floor and a quasi-symmetry about the centreline between them is evident. The re-circulation regions are centred at about $x/D = 0.8$ and $z/D = \pm 0.5$, as marked by the arrow in Figure 5.15(a). A saddle point ahead of the cellular structures is at $x/D = 1.5$ and $z/D = 0.1$, as indicated by the arrow, and no further critical point is evident from these plotted streamlines. In Figure 5.15(b) the sectional streamlines are superimposed on top of the oil flow visualization picture and there is a close agreement in the flow pattern. For the cavity of $W/D = 2$, Figure 5.16(a) shows two mean spanwise re-circulation patterns on the cavity floor. Figure 5.16(a) shows that the re-circulating flow region comprises of two cellular structures centred at about $x/D = 1$ and $z/D = \pm 0.48$, and, a node point is roughly at about $x/D = 1.4$ and $z/D = 0.0$. The superimposed sectional streamlines are shown in Figure 5.16(b) and again show good qualitative agree-

ment with oil flow. The mean spanwise re-circulation pattern for the cavity of $W/D =$ 1.5 is shown in Figure 5.17(a) and the asymmetrical behaviour is evident. The main re-circulation region comprises of a single cellular structure and its focal point is centred at about $x/D = 0.5$ and $z/D =$ -0.3. Again the oil flow visualization and the PIV results show a good qualitative agreement as shown in Figure 5.17(b). Figure 5.18(a) shows the mean spanwise re-circulation patterns observed on the floor of the cavity of $W/D = 1$. An asymmetric surface flow is shown by the streamline plot in Figure 5.18(a). It can be seen that the main re-circulation region has a single cellular structure and its focal point is centred at $x/D = 0.8$ and $z/D = 0.02$ and a bifurcation line lies between $x/D = 1.0$ and $x/D = 2.0$. The oil flow visualisation in Figure 5.18(b) agrees qualitatively with the PIV measurements. The oil flow visualization on the cavity of $W/D = 0.5$ was not clearly indicative of the flow pattern. However PIV measurements at $y/D =$ -0.9 in Figure 5.19(a) shows that there are two focal points close to the cavity floor. The first one is at $x/D =$ 0.5, $z/D = 0.0$ and the second one is at $x/D = 1.5$ and $z/D = 0.0$. These two points are separated by a bifurcation line. No other critical point is present. Therefore, the narrower cavities $W/D = 2.0$, 1.5, 1.0 and 0.5 showed that an asymmetric mean flow pattern exists near the base of the cavity. Minor discrepancies between the oil flow and PIV is due to the fact that the PIV data was not acquired on the surface.

For the widest cavity of $W/D = 3$, the cavity span was large enough such that the two focal points are separated by a saddle point. It was observed that the flow pattern was more or less symmetrical. For the cavity of $W/D = 2$, the two focal points can be seen to interact with each other as the cavity width was reduced, and a node point now separates the two foci. When the cavity width was reduced further, only one focal point existed and no other critical point was found and the flow pattern was completely asymmetrical. Thus the type of critical points control the flow pattern, as expected, but the cavity width dictates which type of critical points can exist.

5.3.3 Instantaneous flow features

The analysis of the instantaneous PIV data follows that of Adrian *et al* [91] where various velocity field decomposition methods have been proposed. The Reynolds averaging of the time-dependent velocity into its mean and fluctuating components is the standard approach to describing turbulent velocity fields. Such an approach is the correct basis for statistical analyzes but it does not provide the means for visualizing the time-dependent flow dynamics. To understand the nature of the structured, coherent flow motion, a method for extracting the large scale eddies is best suited.

In this study, the Large Eddy decomposition method is used to visualize the large scale structures. The instantaneous velocity field $\mathbf{u}$ is filtered through a low-pass homogeneous Gaussian filter. A filtered velocity field $\overline{\mathbf{u}}$ is estimated as in equation (5.1), where the integral sign is over the entire flow domain volume V. The filter function is defined in equation (5.2).

$$\overline{\mathbf{u}}(\mathbf{x},t) = \int_V \Pi(\mathbf{e})\mathbf{u}(\mathbf{x}-\mathbf{e},t)d\mathbf{e} \tag{5.1}$$

$$\Pi(\mathbf{e}) = \left(\frac{6}{\pi\underline{\Delta}^2}\right)^{1/2} exp\left(-\frac{6|\mathbf{e}|^2}{\underline{\Delta}^2}\right) \tag{5.2}$$

where $\underline{\Delta}$ defines the filter width. In the current study, a filter width of 10mm was used. Additionally, following [91], a Galilean decomposition is applied to the filtered velocity field. The total velocity field is represented as the sum of the filtered velocity field and a constant convection velocity $\mathbf{U}_c$ which is taken as approximately 66% of the freestream value. When the convection velocity matches the translational velocity of an eddy, the latter becomes visible as a circular pattern of the velocity vectors. To visualize the large-scale vortical structures in the shear layer, the Galilean transformation is applied to the

filtered instantaneous velocity field. Sample results for the cavities of $W/D = 18$, 3 and 1 are presented for a freestream speed of 30 m/s.

The large-scale decomposed velocity field for the $W/D = 18$ cavity is shown in Figure 5.20. Large-scale vortical structures are clearly present within the shear layer that spans across the cavity opening. At any instant in time, there may be three or more vortical structures within the shear layer. This is linked to the shear layer oscillation modes. The vortical structures (disturbances) are first produced at the leading edge of the cavity and they are subsequently amplified as they are convected downstream towards the trailing edge. These coherent structures show a regular occurrence within the shear layer hinting at a periodic oscillation of the flow over the cavity. However to confirm this hypothesis, the pressure spectra at discrete locations on the cavity walls will have to measured.

Rockwell and Knisely [34] argue that the presence of the aft wall in an open cavity flow enhances the organization of the flow in terms of their regular occurrence within the shear layer. Furthermore, this organized nature of the flow due to the impinging shear layer is not restricted to the vicinity of the impingement region but is present along the entire length of the cavity. The results in Figure 5.20 support this argument. In Figure 5.20(a) it can be seen that there are two vortical structures within the shear layer. The first has just escaped the cavity while the second one is at $x/D = 2.0$ and is being convected downstream. A vortex escaping the cavity trailing edge is a class of vortex-edge interaction described by Rockwell and Knisely. In Figure 5.20(c) one vortex is convected towards the trailing edge and is on the point of impingement. The snapshot in Figure 5.20(d) shows that part of this vortex is swept downwards in the cavity and is a class of interaction which Rockwell and Knisely [34] describe as partial clipping. Other classes of vortex-edge interactions are the 'clipped' and the 'escape' regimes. In general, none of these classes of vortex-edge interaction persisted at all times but a time-dependent combination of these was seen in the range of PIV data acquired, leading to what is termed as 'vortex jitter'.

For the 3D configurations of $W/D = 3$ and $W/D = 1$, the same analysis as in the 2D case

has been applied. However the field of view in the PIV images was set-up so that the shear layer was not entirely captured and the region below the plane $y/D =$ -0.1 is outside the field of view. This was due to the fact that the CCD camera was placed below the side blocks constraining the cavity span. This reduced the field of view available to the CCD camera. Figure 5.21 shows a portion of the shear layer across the mouth of the cavity. The shear layer reveals the existence of large-scale structures. The organized nature of the shear layer is not obvious. Due to the presence of the aft cavity edge a recurrent pattern in the vortical structures is expected and upon examination of the trailing edge region, such a pattern emerges in Figure 5.22. The snapshots of the interaction of the shear layer with the cavity trailing edge is highly irregular and reinforces the idea that 'vortex jitter' occurred. Mass ejection at the trailing edge is however visible in Figure 5.22(c) and Figure 5.22(d), where the velocity vectors are seen to be directed away from the cavity opening. This indicates that recurrent mass injection and ejection exists close to the cavity trailing edge.

The shear layer above the $W/D = 1$ cavity was monitored in the same way as the $W/D =$ 3 case. Figure 5.23 shows a series of snapshots at equal intervals of time. The organized nature of the flow over the cavity is clearly evident in this case and seems to extend along the entire cavity opening as opposed to the $W/D = 3$ case. It can be deduced that in each snapshot there are two large-scale eddies within the shear layer. The gradual growth of these structures as they convect downstream is observable through the snapshot sequence. Upon examination of the flow around the trailing edge region, shown in Figure 5.24, the class of interaction of the shear layer and the trailing edge can be deduced. Figures 5.24(a) and 5.24(b) show that the vortices have escaped from the cavity. In Figures 5.24(c) and 5.24(d) it can be seen that part of the vortices are clipped by the cavity trailing edge. In this case, as in the previous ones, none of the classes of interactions described by Rockwell and Knisely persisted at all times. This again suggests a 'vortex jitter' regime. A reduced amplitude of mass injection and ejection is noticeable in the snapshot sequence of Figure 5.24. Figure 5.24(c) shows a mass ejection event. The area of the outflow is smaller compared to Figure 5.22(d) . This is a direct consequence of reducing the cavity span and hence important 3D effects tend to reduce the extent of the flow oscillation and

mass ejection with respect to the $W/D = 3$ case.

5.4 Summary

The particle image velocimetry technique has been used to provide an account of the velocity field in rectangular cavities at low speeds. The time-averaged mean flow for all configurations has been described and the differences in the time-mean flow features have been documented. To study the flow patterns, oil flow visualization was employed. The flow patterns were explained through critical point theory and explanations for certain topological aspects were proposed. The differences in the flow topology resulting from different cavity geometries were highlighted and explained through critical point theory. The instantaneous velocity field has also been analyzed. The present measurements provide (a) some guidance in setting up 3D CFD models and (b) an insight into the 3D cavity flow physics.

U_∞	x/D	y/D	z/D
10 m/s	2.86	-0.58	0.0
	3.14	-0.45	-1.0
	3.21	-0.36	-1.25
20 m/s	2.86	-0.60	0.0
	2.70	-0.46	-1.0
	2.83	-0.39	-1.25
30 m/s	2.80	-0.65	0.0
	2.89	-0.48	-1.0
	2.99	-0.37	-1.25

Table 5.1: Mean re-circulation centre positions for $W/D = 3$.

U_∞	x/D	y/D	z/D
10 m/s	2.98	-0.58	0.0
	3.14	-0.45	-0.5
	2.96	-0.42	-0.75
20 m/s	2.85	-0.59	0.0
	2.97	-0.52	-0.5
	2.81	-0.46	-0.7
30 m/s	2.89	-0.63	0.0
	2.88	-0.51	-0.5
	2.86	-0.51	-0.75

Table 5.2: Mean re-circulation centre positions for $W/D = 2$.

U_∞	x/D	y/D	z/D
10 m/s	2.91	-0.53	0.0
	3.19	-0.46	-0.25
	3.17	-0.41	-0.5
20 m/s	2.84	-0.55	0.0
	2.99	-0.51	-0.25
	3.07	-0.45	-0.5
30 m/s	2.91	-0.56	0.0
	3.07	-0.52	-0.25
	3.16	-0.44	-0.5

Table 5.3: Mean re-circulation centre positions for $W/D = 1.5$.

U_∞	x/D	y/D	z/D
10 m/s	3.09	-0.48	0.0
	3.15	-0.41	-0.25
20 m/s	3.08	-0.46	0.0
	2.96	-0.46	-0.25
30 m/s	3.03	-0.46	0.0
	2.98	-0.45	-0.25

Table 5.4: Mean re-circulation centre positions for $W/D = 1.0$.

U_∞	x/D	y/D	z/D
10 m/s	2.99	-0.44	0.0
20 m/s	2.94	-0.44	0.0
30 m/s	3.00	-0.44	0.0

Table 5.5: Mean re-circulation centre positions for $W/D = 0.5$.

U_∞	x/D	y/D	z/D
10 m/s	3.12	-0.346	0.0
20 m/s	3.12	-0.346	0.0
30 m/s	3.15	-0.346	0.0

Table 5.6: Mean re-circulation centre positions for 2D cavity.

5.5 Chapter 5 Figures

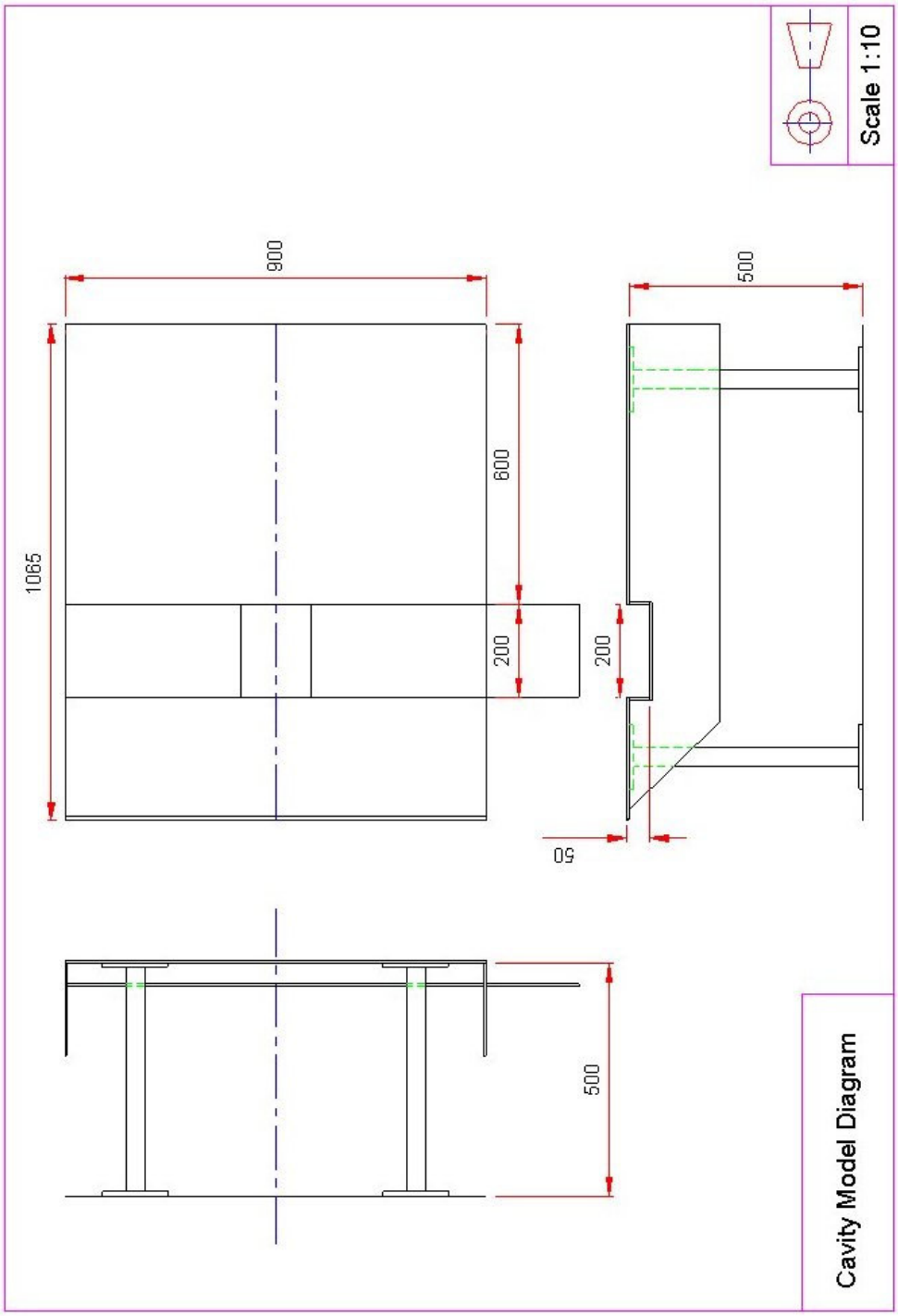

Figure 5.1: Cavity model drawing, all dimensions in mm.

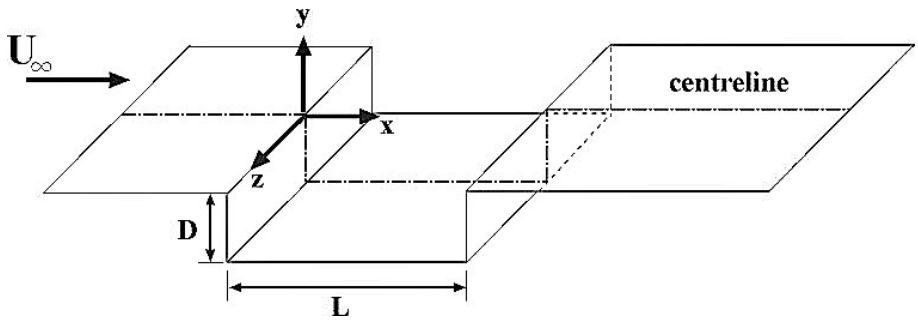

Figure 5.2: 2D cavity configuration.

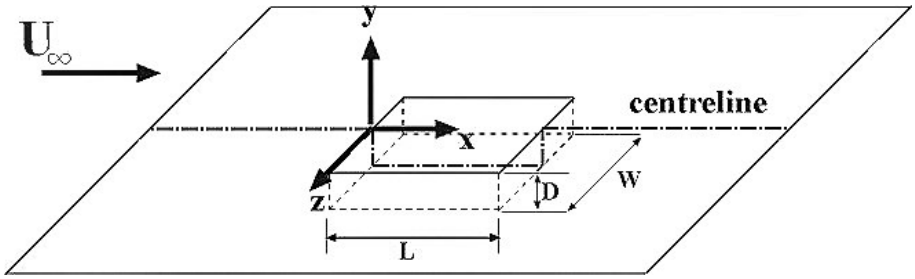

Figure 5.3: 3D cavity configuration.

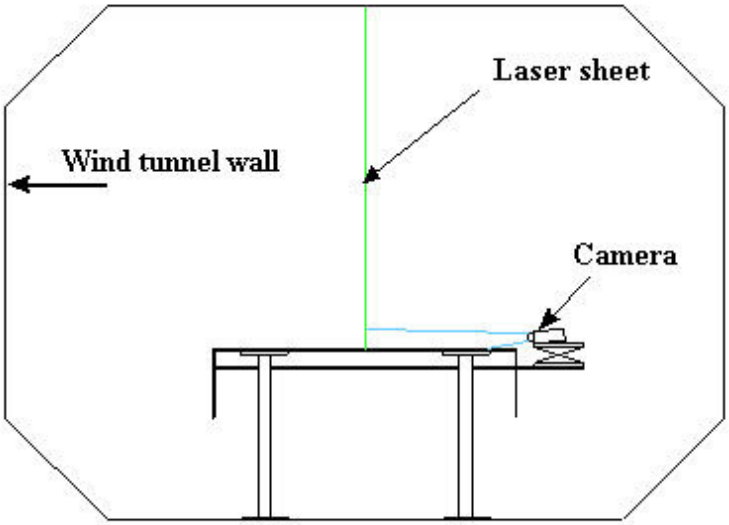

Figure 5.4: Schematic of the model setup in the wind tunnel.

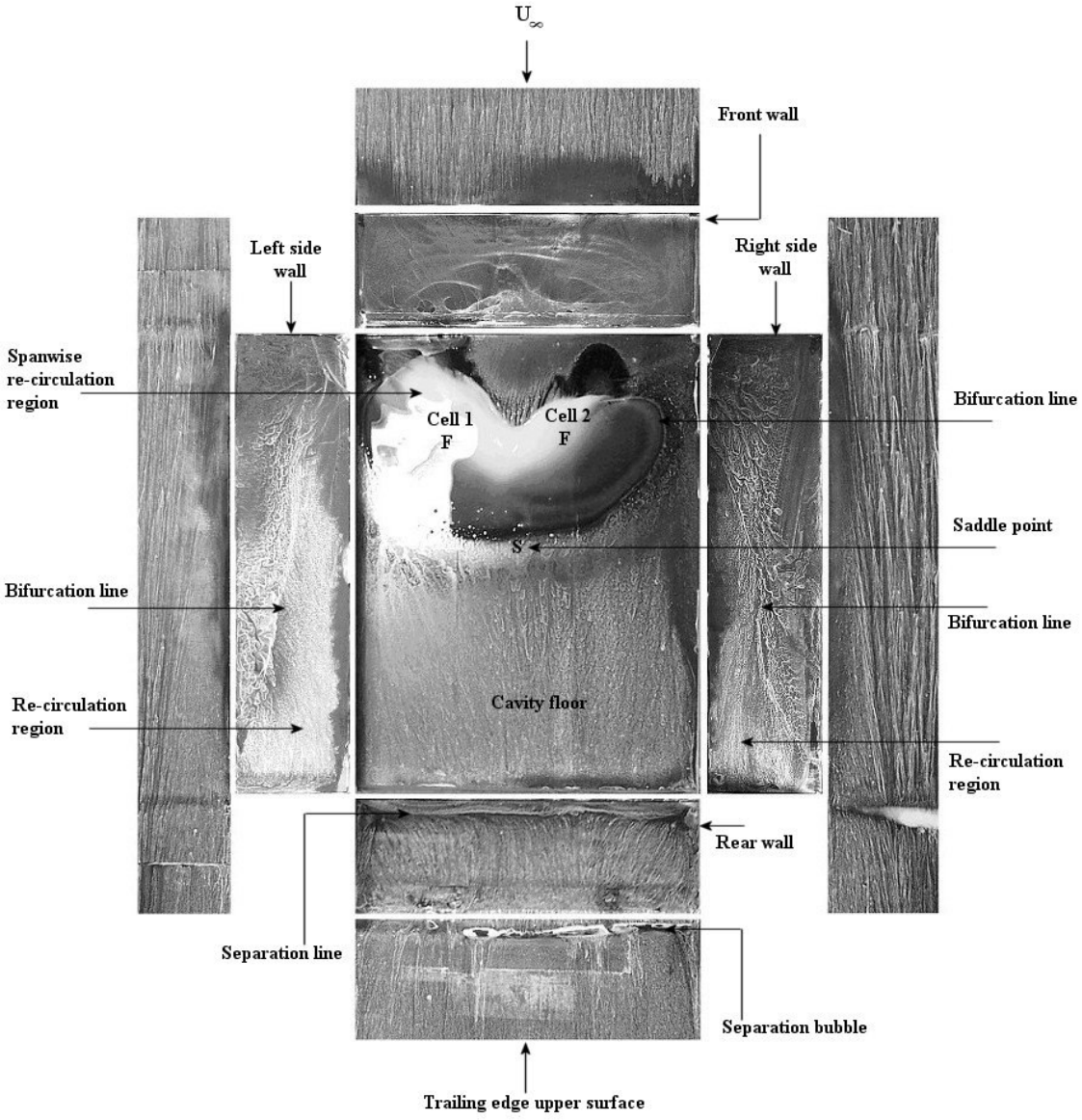

Figure 5.5: Unfolded view of surface flow visualization, $W/D = 3$, $U_\infty = 30m/s$.

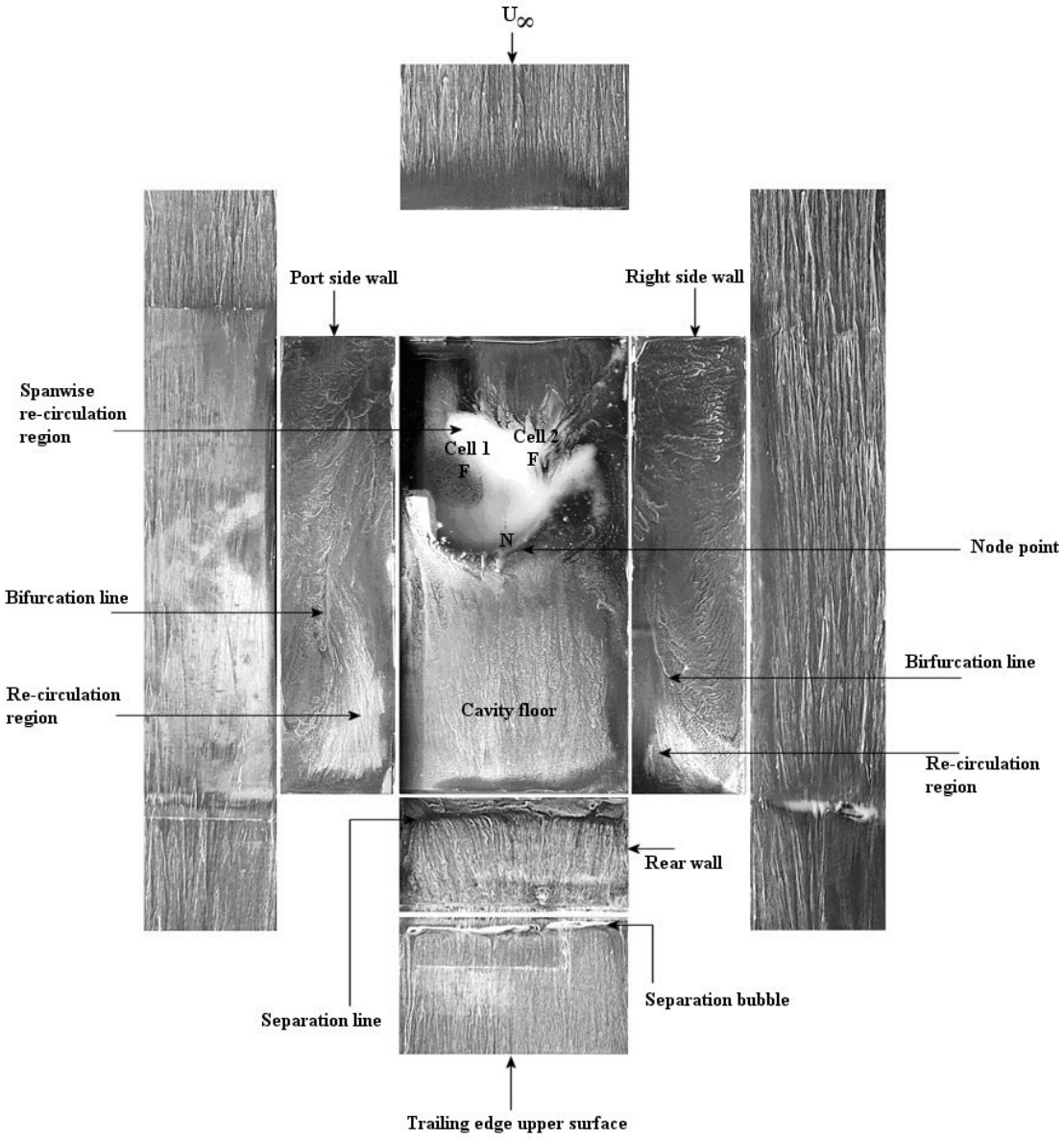

Figure 5.6: Unfolded view of surface flow visualization, $W/D = 2$, $U_\infty = 30m/s$.

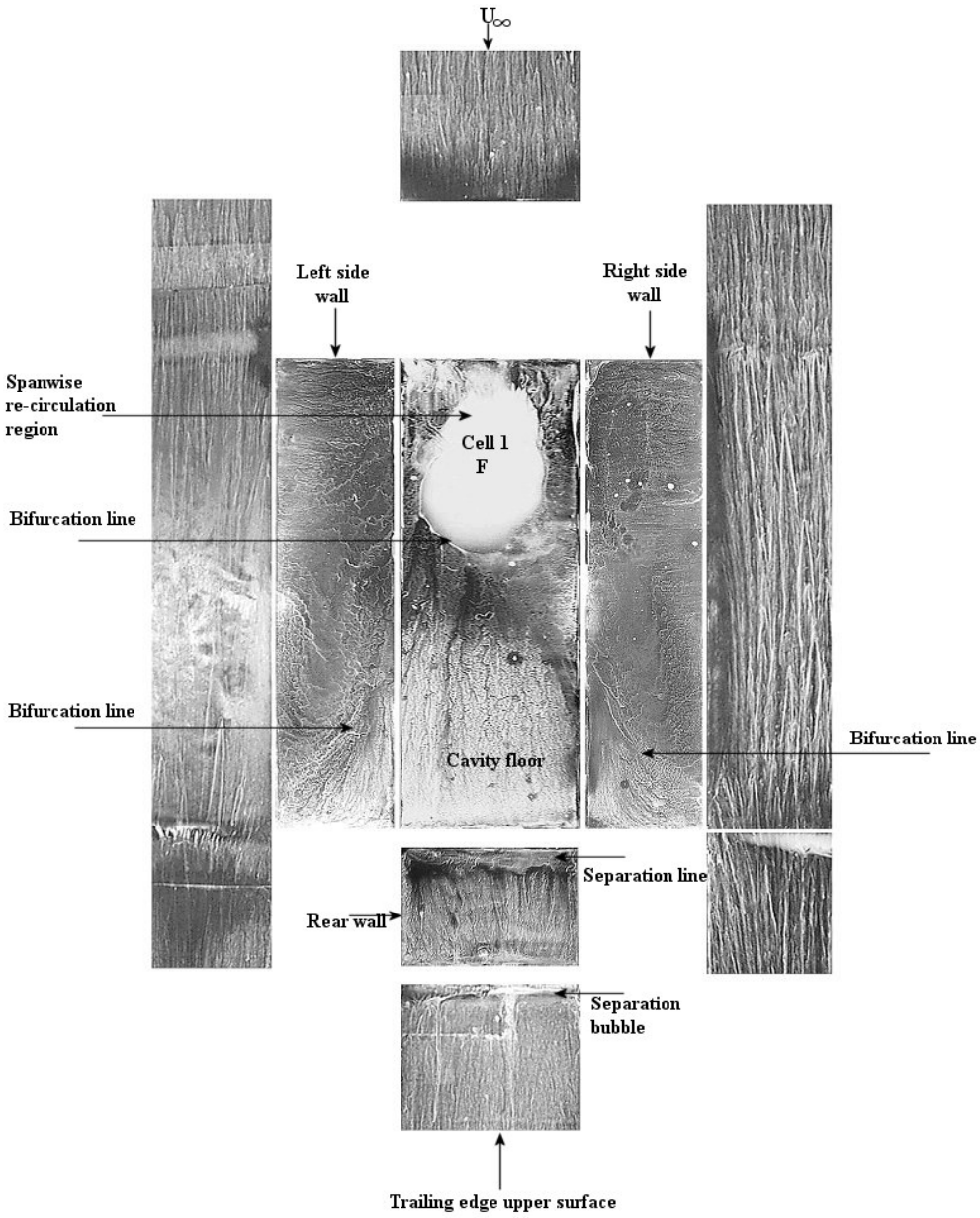

Figure 5.7: Unfolded view of surface flow visualization, $W/D = 1.5$, $U_\infty = 30m/s$.

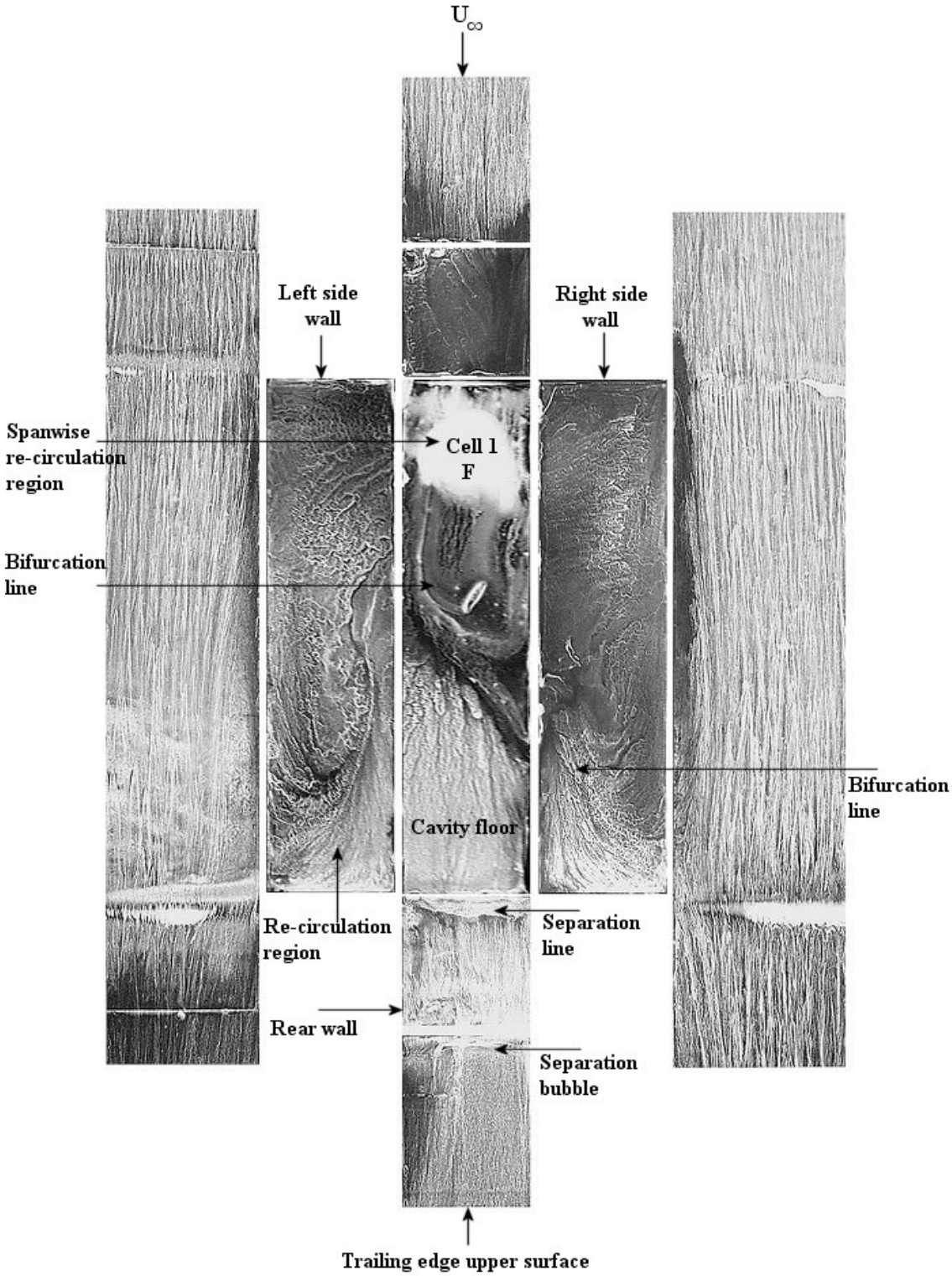

Figure 5.8: Unfolded view of surface flow visualization, $W/D = 1$, $U_\infty = 30m/s$.

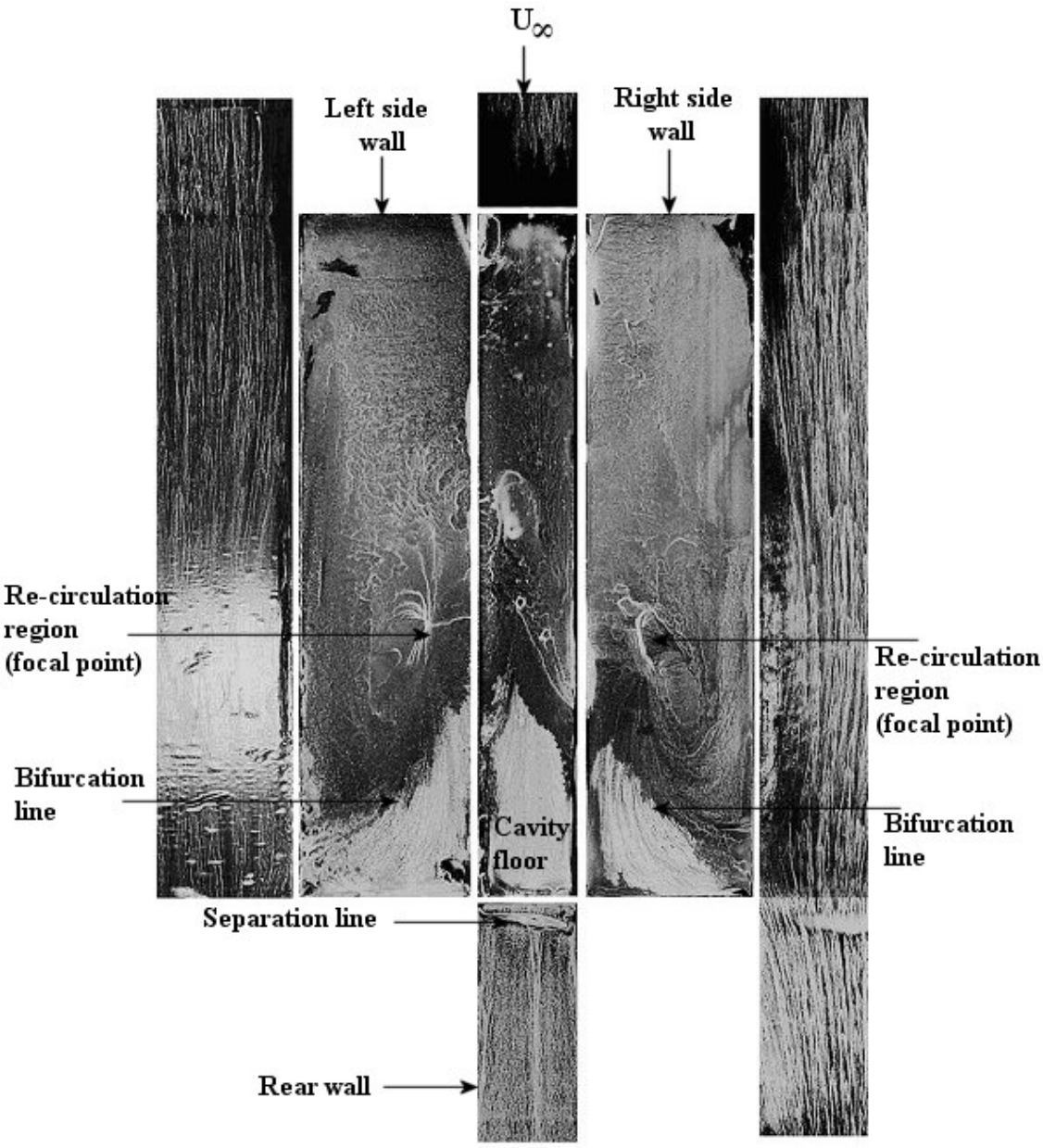

Figure 5.9: Unfolded view of surface flow visualization, $W/D = 0.5$, $U_\infty = 30m/s$.

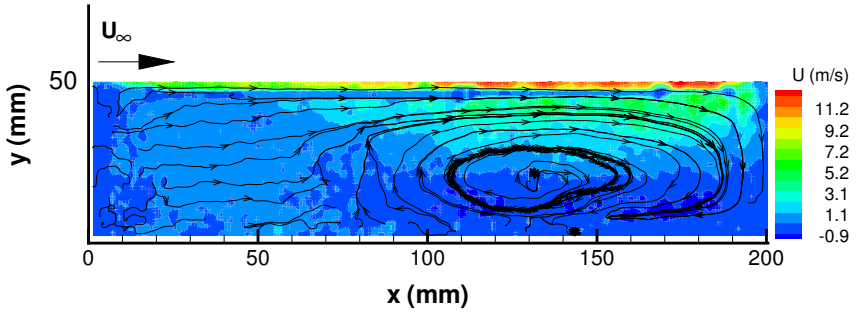

(a) $z/D = 0$.

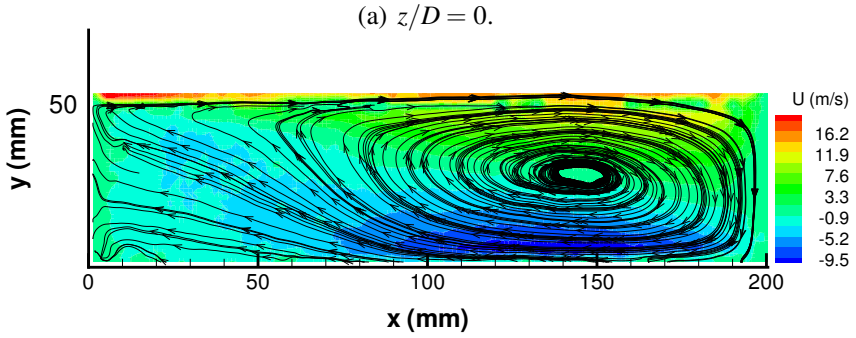

(b) $z/D =$ -1.0.

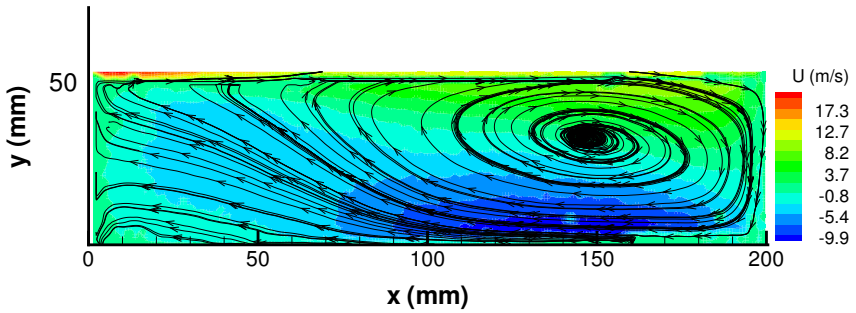

(c) $z/D =$ -1.25.

Figure 5.10: Mean sectional streamlines at various spanwise positions, $W/D = 3$, $U_\infty = 30$m/s.

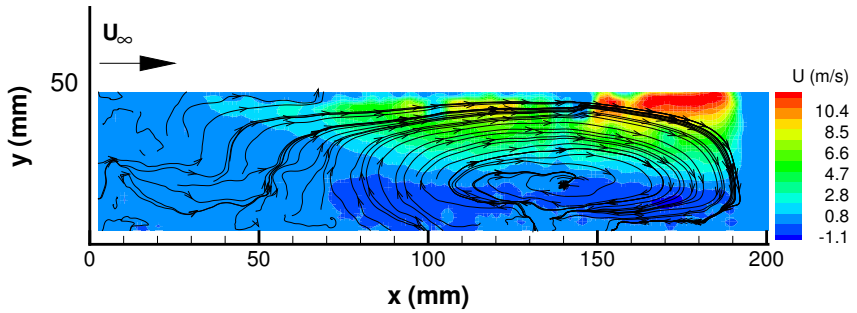

(a) $z/D = 0$.

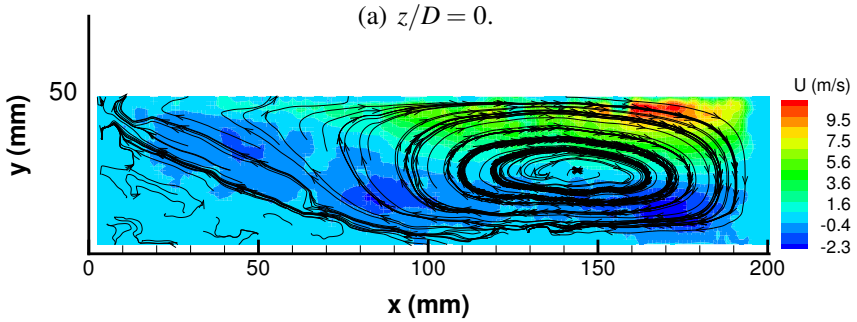

(b) $z/D =$ -0.5.

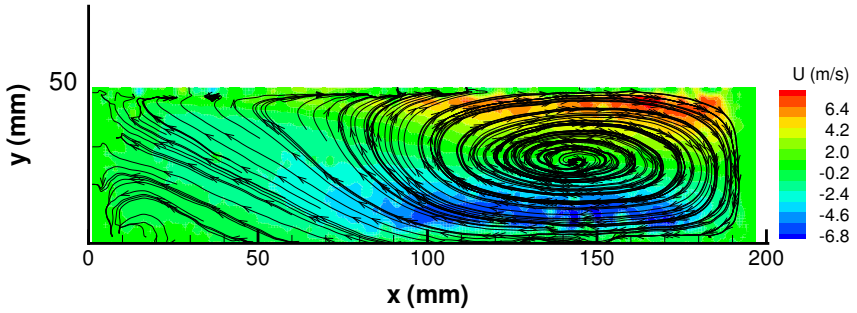

(c) $z/D =$ -0.75.

Figure 5.11: Mean sectional streamlines at various spanwise positions, $W/D = 2$, $U_\infty = 30$m/s.

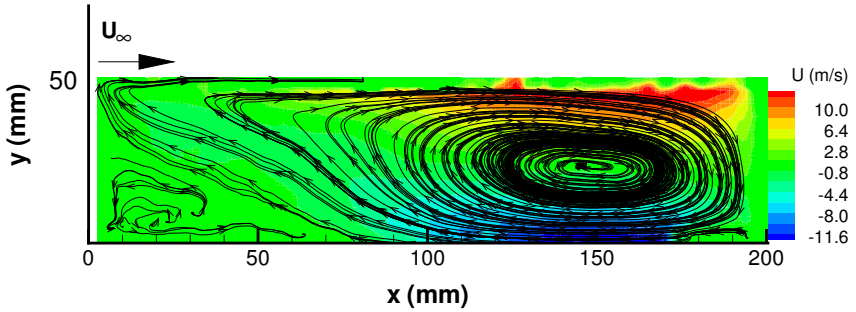

(a) $z/D = 0$.

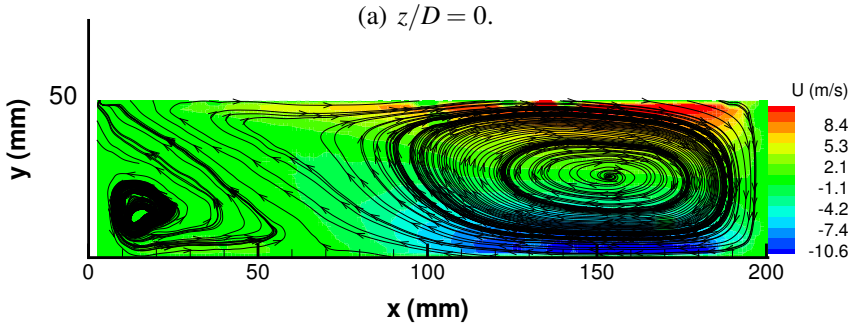

(b) $z/D =$ -0.25.

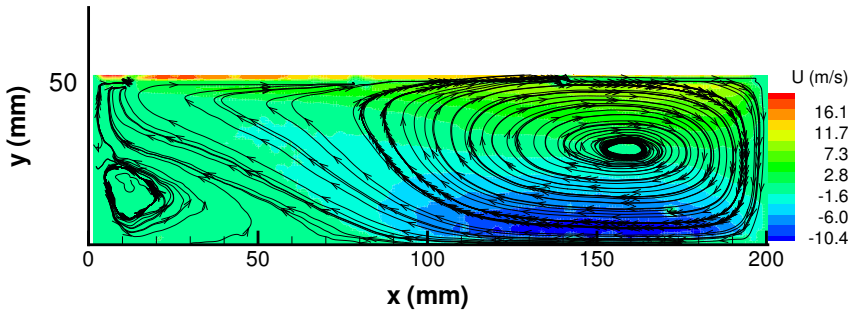

(c) $z/D =$ -0.5.

Figure 5.12: Mean sectional streamlines at various spanwise positions, $W/D = 1.5$, $U_\infty = 30$m/s.

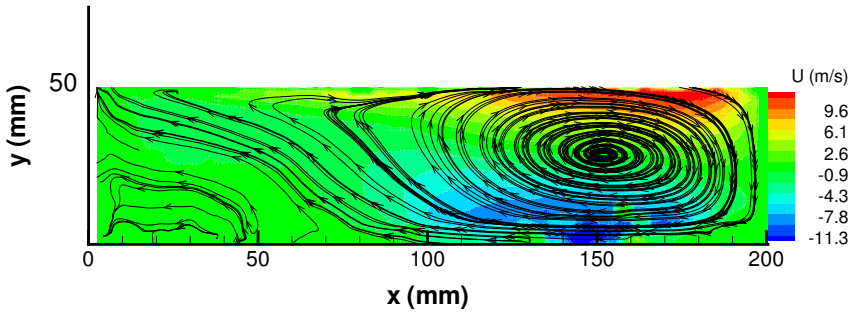

(a) $z/D = 0$.

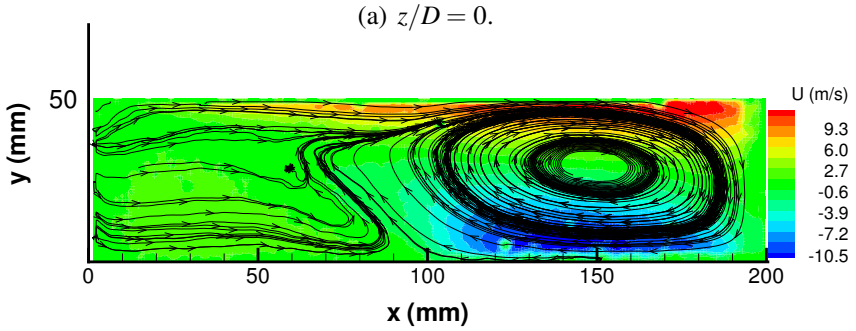

(b) $z/D =$ -0.25.

Figure 5.13: Mean sectional streamlines at various spanwise positions, $W/D = 1.0$, $U_\infty = 30$m/s.

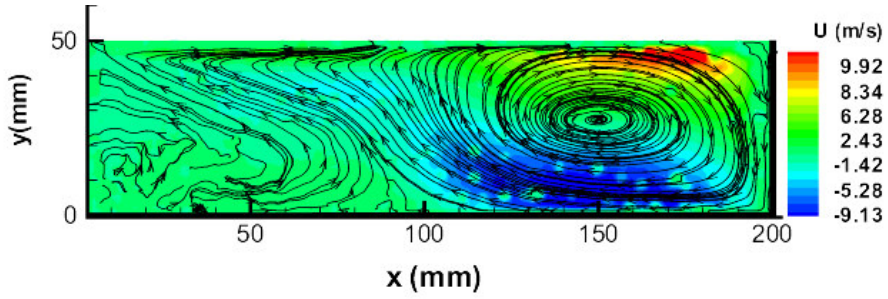

(a) $W/D = 0.5$, $z/D = 0$; 3D flow. $U_\infty = 30$ m/s.

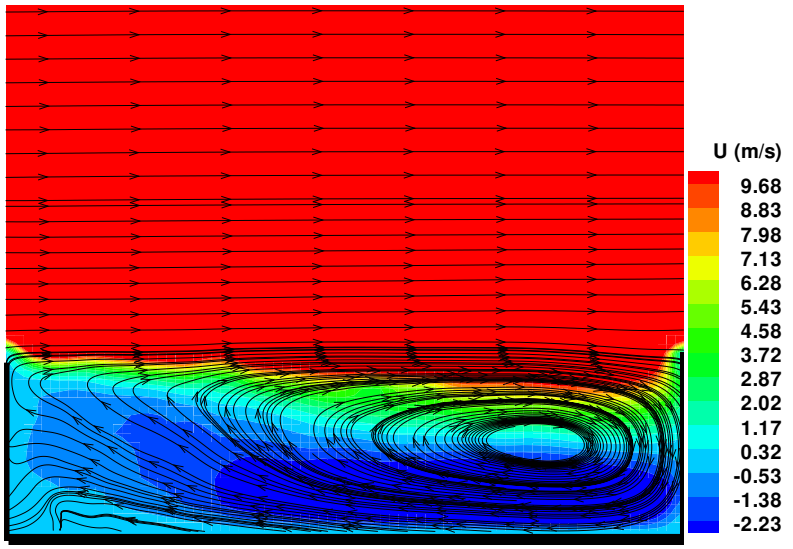

(b) $W/D = 18$, $z/D = 0$; 2D flow. $U_\infty = 30$ m/s.

Figure 5.14: Comparison of 3D $W/D = 0.5$ cavity and 2D $W/D = 18$ cavity. Flow from left to right.

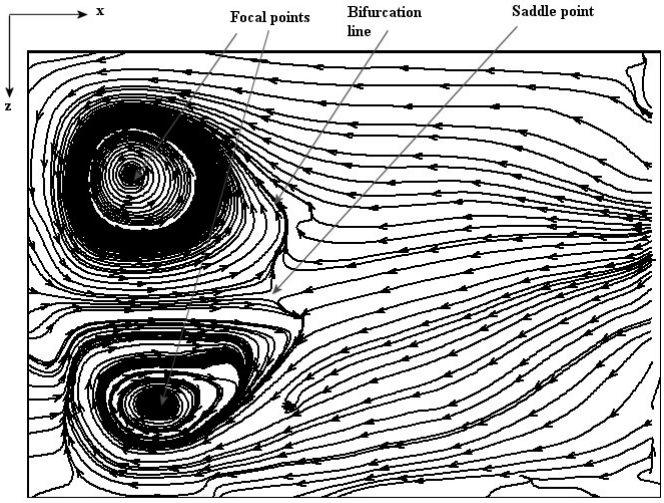

(a) Mean spanwise re-circulation from time-averaged PIV, $W/D = 3$, $y/D =$ -0.9; $U_\infty = 30$ m/s.

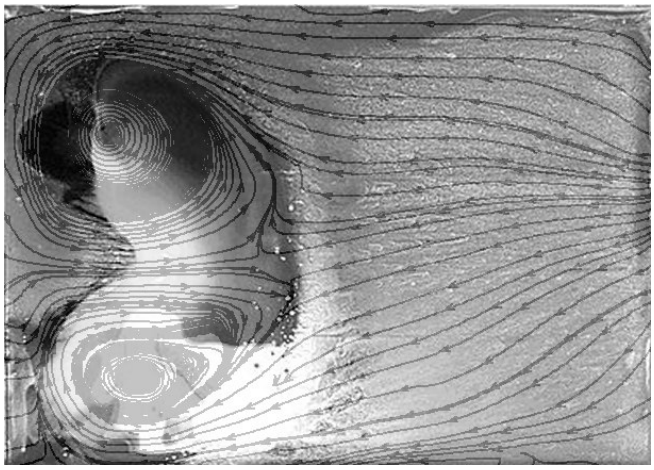

(b) Superimposed sectional streamlines on oil flow.

Figure 5.15: Comparison of surface oil flow against PIV data, $W/D = 3$, $y/D =$ -0.9; $U_\infty = 30$ m/s.

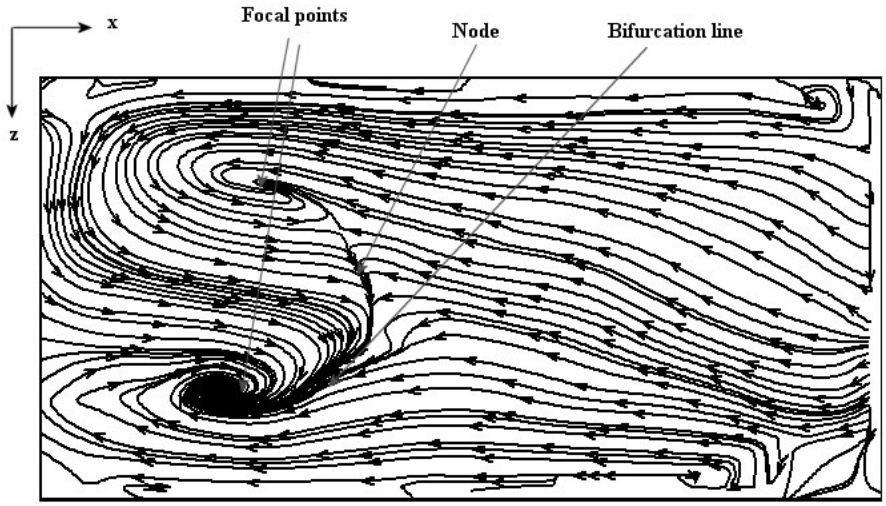

(a) Mean spanwise re-circulation from time-averaged PIV, $W/D = 2$, $y/D =$ -0.9; $U_\infty = 30$ m/s.

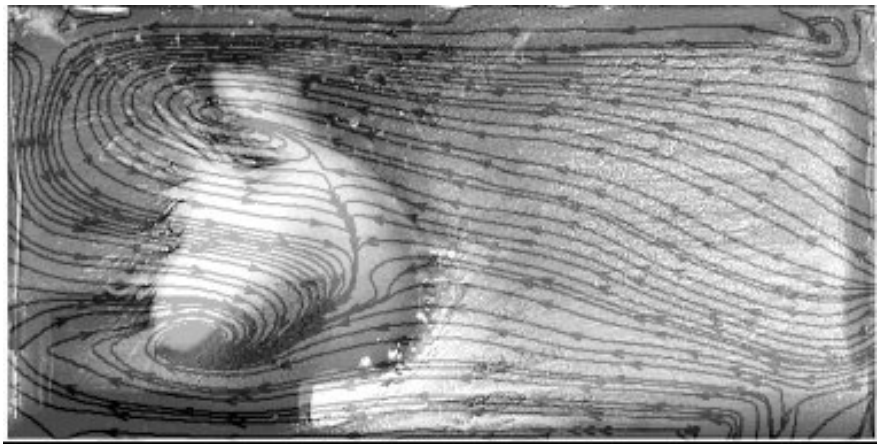

(b) Superimposed sectional streamlines on oil flow.

Figure 5.16: Comparison of surface oil flow against PIV data, $W/D = 2$, $y/D =$ -0.9; $U_\infty = 30$ m/s.

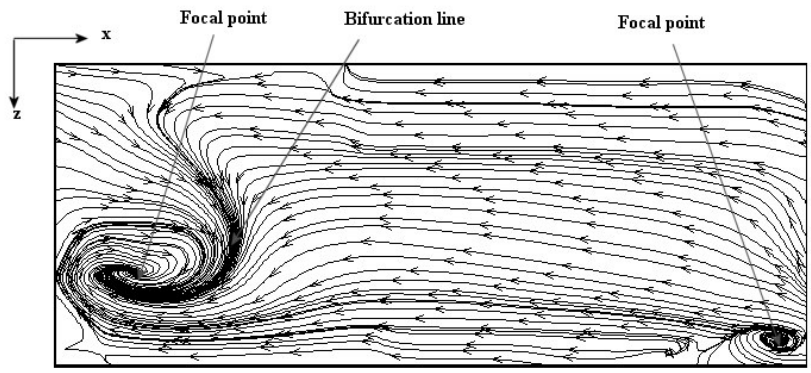

(a) Mean spanwise re-circulation from time-averaged PIV, $W/D = 1.5$, $y/D =$ -0.9; $U_\infty = 30$ m/s.

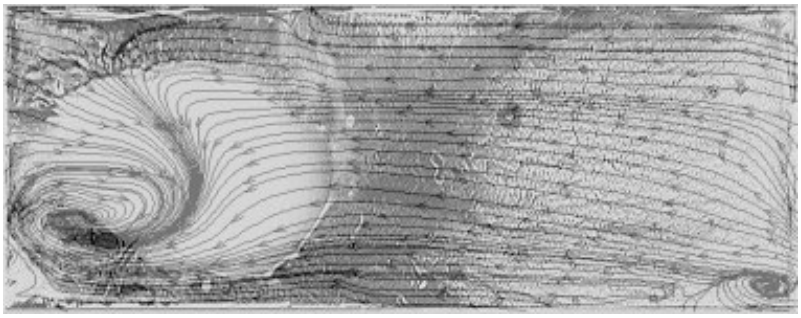

(b) Superimposed sectional streamlines on oil flow.

Figure 5.17: Comparison of surface oil flow against PIV data, $W/D = 1.5$, $y/D =$ -0.9; $U_\infty = 30$ m/s.

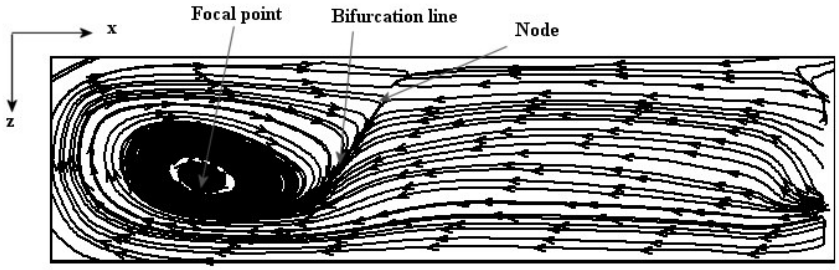

(a) Mean spanwise re-circulation from time-averaged PIV, $W/D = 1$, $y/D =$ -0.9; $U_\infty = 30$ m/s.

(b) Superimposed sectional streamlines on oil flow.

Figure 5.18: Comparison of surface oil flow against PIV data, $W/D = 1$, $y/D =$ -0.9; $U_\infty = 30$ m/s.

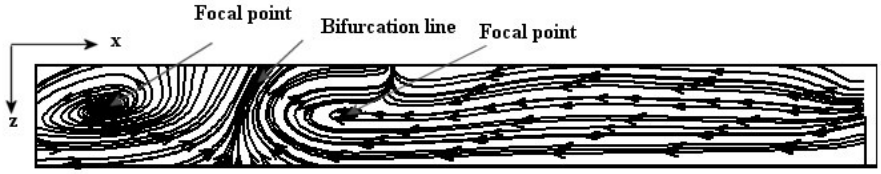

(a) Mean spanwise re-circulation from time-averaged PIV, $W/D = 0.5$, $y/D =$ -0.9; $U_\infty = 30$ m/s.

(b) Superimposed sectional streamlines on oil flow.

Figure 5.19: Comparison of surface oil flow against PIV data, $W/D = 0.5$, $y/D =$ -0.9; $U_\infty = 30$ m/s.

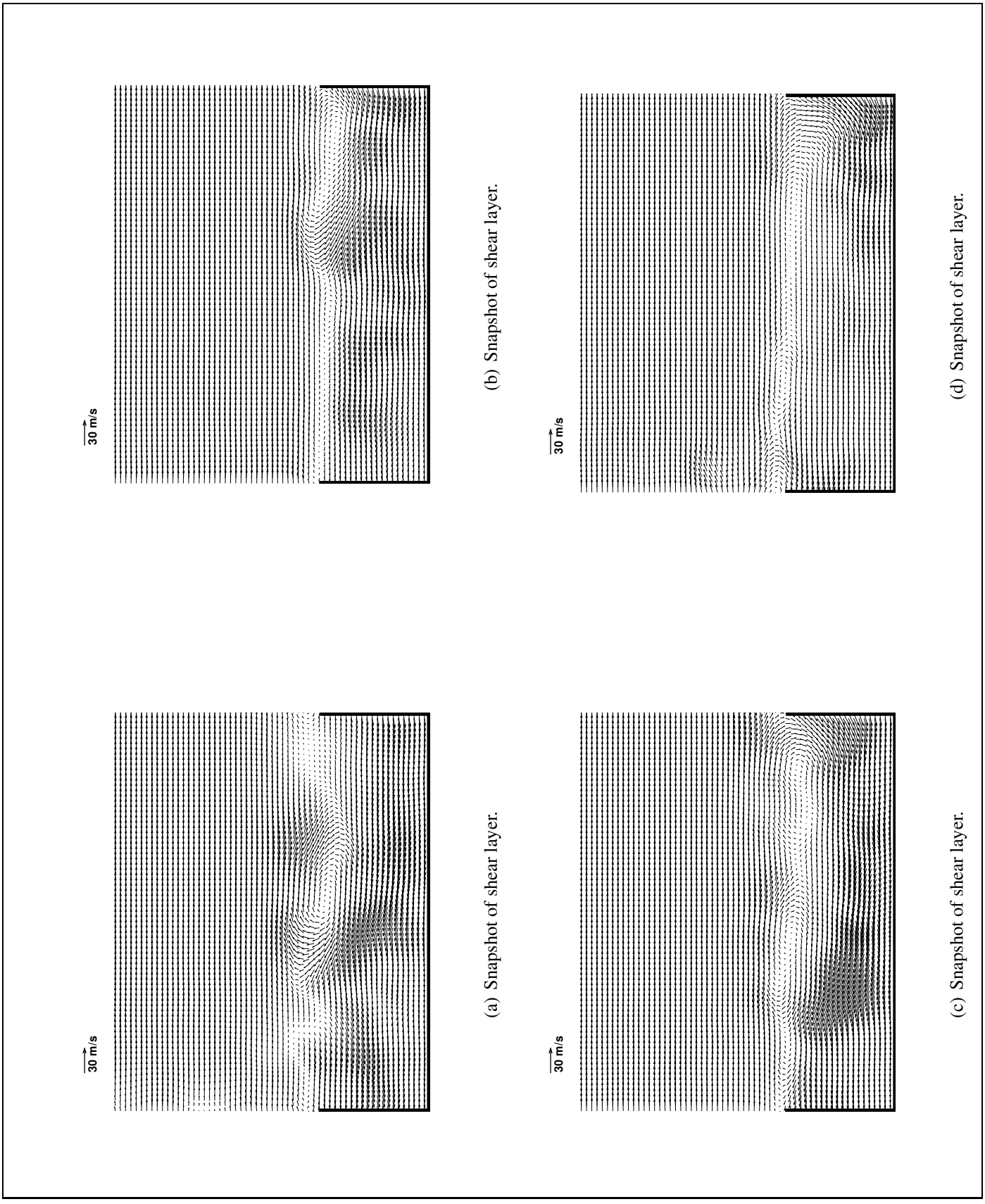

(a) Snapshot of shear layer.

(b) Snapshot of shear layer.

(c) Snapshot of shear layer.

(d) Snapshot of shear layer.

Figure 5.20: LES decomposition with Galilean transformation ($2D,\ W/D = 18,\ U_\infty = 30m/s$), Flow from Left to Right.

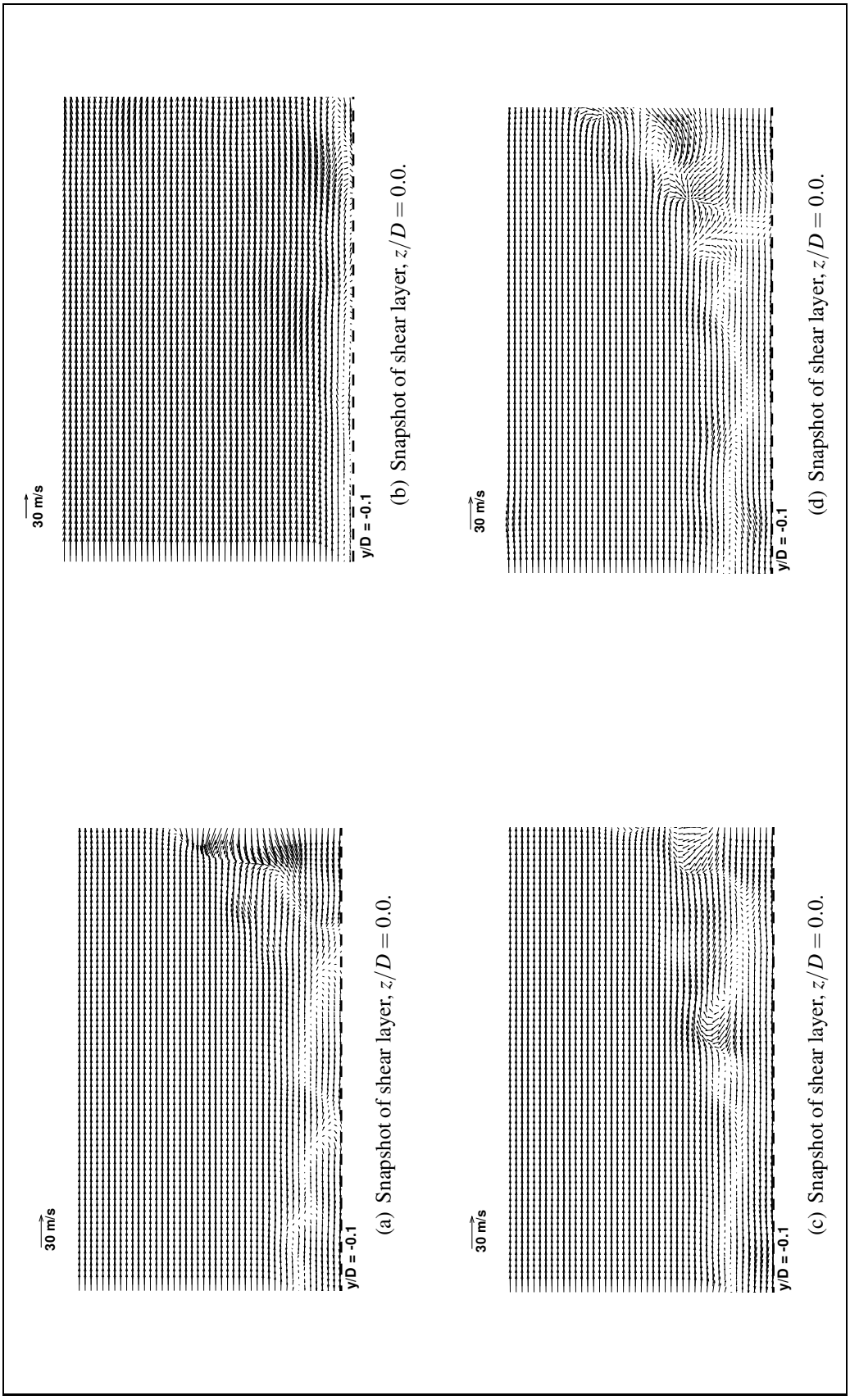

(a) Snapshot of shear layer, $z/D = 0.0$.

(b) Snapshot of shear layer, $z/D = 0.0$.

(c) Snapshot of shear layer, $z/D = 0.0$.

(d) Snapshot of shear layer, $z/D = 0.0$.

Figure 5.21: LES decomposition with Galilean transformation of the shear layer ($3D$, $W/D = 3$, $U_\infty = 30m/s$).

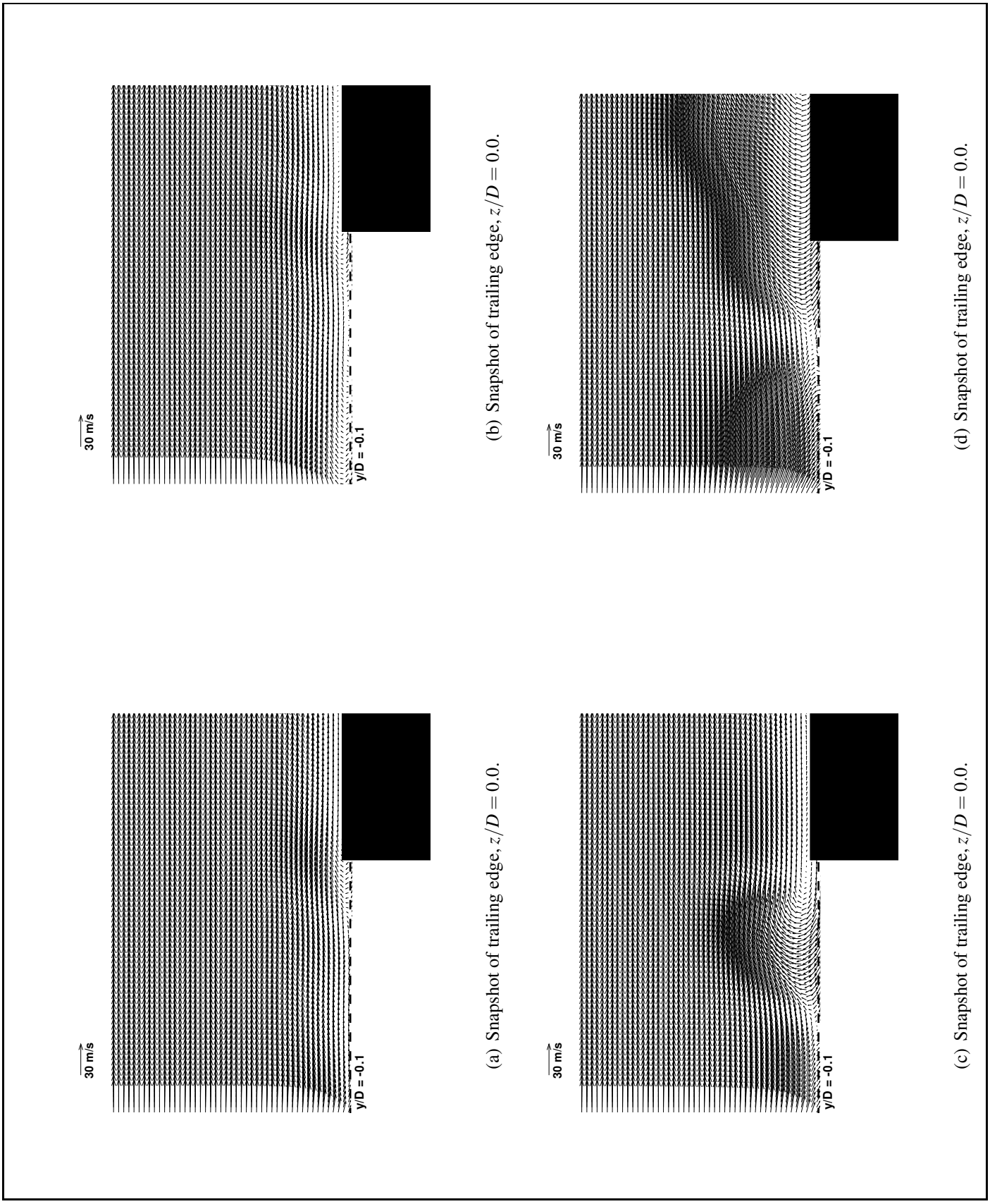

(a) Snapshot of trailing edge, $z/D = 0.0$.

(b) Snapshot of trailing edge, $z/D = 0.0$.

(c) Snapshot of trailing edge, $z/D = 0.0$.

(d) Snapshot of trailing edge, $z/D = 0.0$.

Figure 5.22: LES decomposition with Galilean transformation at the trailing edge ($3D$, $W/D = 3$, $U_\infty = 30m/s$).

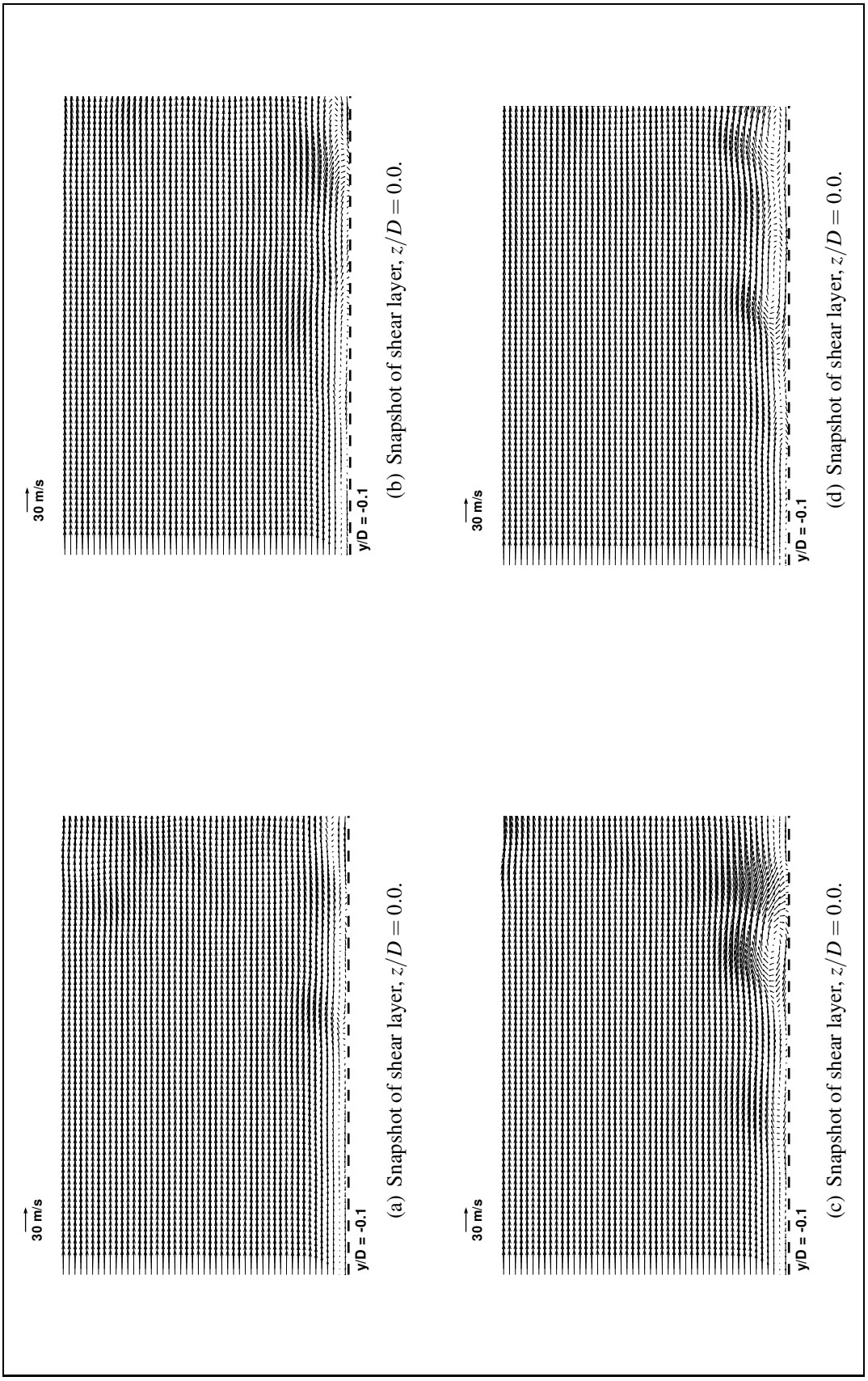

(a) Snapshot of shear layer, $z/D = 0.0$.

(b) Snapshot of shear layer, $z/D = 0.0$.

(c) Snapshot of shear layer, $z/D = 0.0$.

(d) Snapshot of shear layer, $z/D = 0.0$.

Figure 5.23: LES decomposition with Galilean transformation of the shear layer ($3D$, $W/D = 1$, $U_\infty = 30m/s$).

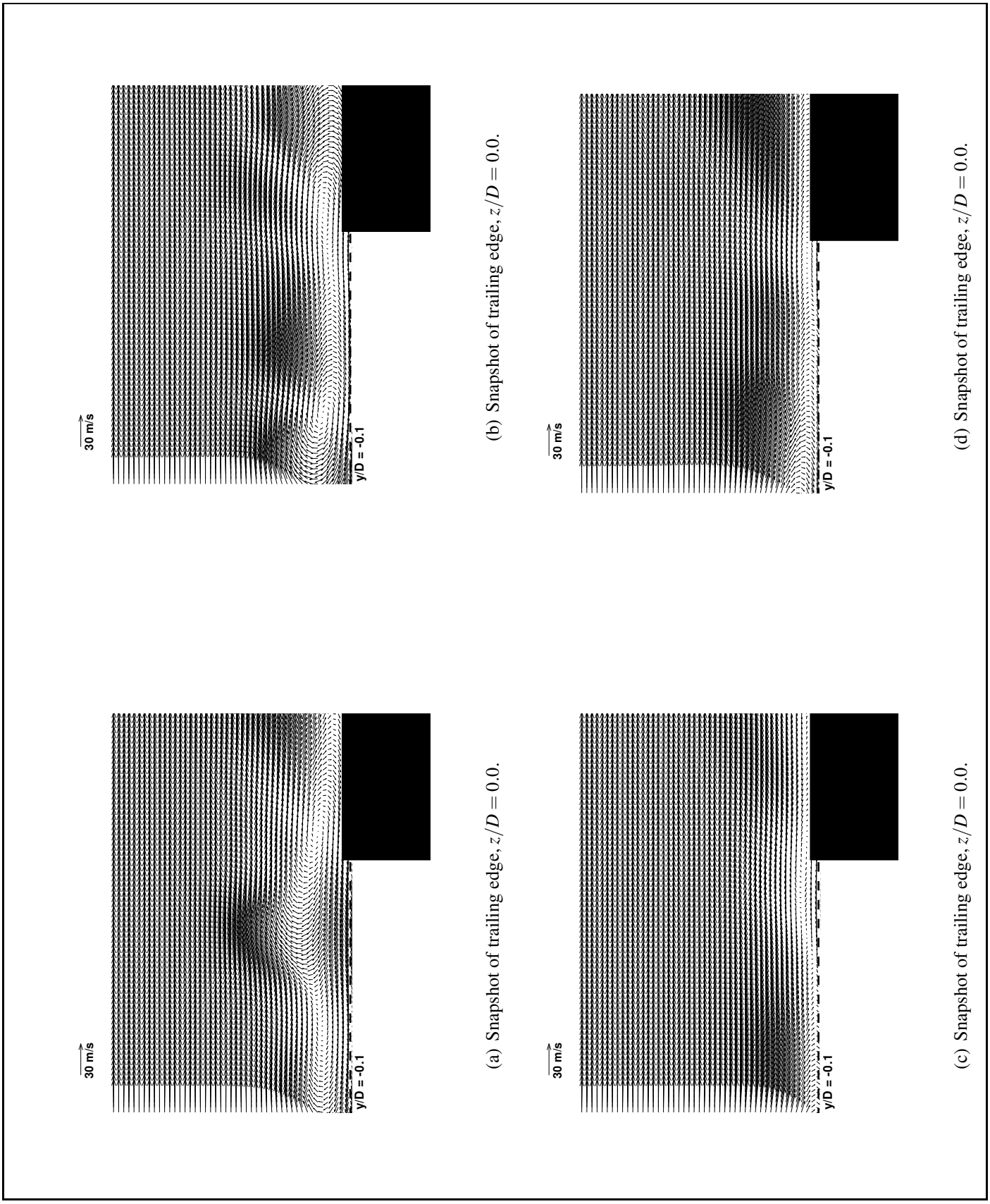

(a) Snapshot of trailing edge, $z/D = 0.0$.

(b) Snapshot of trailing edge, $z/D = 0.0$.

(c) Snapshot of trailing edge, $z/D = 0.0$.

(d) Snapshot of trailing edge, $z/D = 0.0$.

Figure 5.24: LES decomposition with Galilean transformation at the trailing edge ($3D$, $W/D = 1$, $U_\infty = 30m/s$).

Chapter 6

Three-Dimensional Cavity Flow Simulations

6.1 Overview

The purpose of this chapter is to present the results obtained in the simulation of a 3D cavity flow at a low Mach number. The geometry is representative of a rectangular cutout on a plane surface. The aim is to study the three-dimensionality incurred in such a case.

6.2 Introduction

Although 2D cavity flows models are useful in assessing the the aerodynamic and acoustic fields, three-dimensionality is an important factor that can have a significant effect on both. It has been shown in Chapter 5 that significant 3D effects occur in certain cavity flows. A degree of three-dimensionality was present in all cases studied in Chapter 5. These effects are noticeable in the aerodynamic field where spanwise oscillation modes of the shear layer have also been reported in recent works by Sagaut *et al* [92, 46]. In the

present investigation, the DES approach is used on a 3D cavity geometry. The high-order CAA code of Chapter 2 is used to compute the aerodynamic field as well as part of the acoustic near-field.

6.3 Geometry and Inflow Conditions

The model geometry is a 3D rectangular cavity which is cut into a flat surface. The geometry is characterised by the length-to-depth ratio and the width-to-depth ratio. The current geometry has a length-to-depth ratio of 2 and a width-to-depth ratio of 2. This choice of width-to-depth ratio gives a 3D flow as shown in Sections 6.5 and 6.6 later on.

The freestream Mach number is 0.4 and the Reynolds number based on the cavity depth, Re_D, is taken as 60,000 to match that of the $L/D = 2$ 2D cavity presented in Chapter 4. A turbulent boundary layer is imposed such that the boundary layer thickness $\delta \simeq 0.2D$ at the cavity leading edge. Here D denotes the cavity depth.

6.4 Computational Domain

Figure 6.1 shows the multi-block topology of the computational domain. The origin of the coordinates is at the leading edge of the cavity on the symmetry $(x-y)$ plane. Due to the limited computational resources available, it was decided to model just half of the cavity geometry by imposing a symmetry plane about the enclosure mid-span. This choice would have been better justified for a $L/D = 4$, $W/D = 3$ cavity that is known to develop two stable re-circulating cells at the lower speed of $U_\infty = 30$ m/s as shown in Figure 5.5. However, some symmetry was also observed at $W/D = 2$.

The streamwise extent of the domain is $20D$ and $10D$ in the vertical and spanwise directions respectively. The domain is divided into 34 blocks with 2.7 million grid points in total. In the present calculation, only half of the cavity geometry was simulated. A

symmetry boundary condition was applied on the plane corresponding to $z/D = 0$. The planes at the domain extremities were treated with a non-reflecting buffer zone boundary condition as implemented by Richards *et al* [79]. This ensures that outgoing acoustic waves are damped thus preventing numerical reflections back towards the enclosure. A non-slip boundary condition was applied on the solid walls. The flow solver was run in parallel on 34 Intel Pentium 4 processors. The computation lasted several months due to the limited computational resources available to the author.

6.5 3D Time-Averaged Flow Characteristics

The time-averaged flow characteristics inside the 3D cavity can be visualized and understood by examining the $(x-y)$ sectional planes at different spanwise positions. Figure 6.2 shows the sectional streamlines corresponding to four spanwise locations. Figure 6.2(a) corresponds to the symmetry plane along the cavity centerline. It can be observed that the flow is dominated by a main clockwise re-circulating flow region driven by the shear layer and a counter clockwise small re-circulation in the upstream cavity corner. The main clockwise re-circulating flow region dominates the flow pattern in the streamwise direction. This re-circulation is also present at the other spanwise locations, as shown in Figure 6.2(b) to 6.2(d). The most noticeable feature in Figure 6.2(b) to 6.2(d) is the variation of the position of the vortex-core. The vortex core in the case of a 3D flow is essentially a critical point in the flow topology called a focal point or a spiral. In Figure 6.2(a), the position of the focal point in the main re-circulating region is located at $x/D = 1.04$ and $y/D =$ -0.52, as determined using the same method as in Section 5.3.2. On the $z/D = 0.2$ plane, the focal point is at $x/D = 1.14$ and $y/D =$ -0.4, suggesting that the vortex core translates in the streamwise direction and in the upward direction between $z/D = 0$ and $z/D = 0.2$. A similar trend was observed in the experimental results described in Chapter 5. The upward drift in the position of the vortex core was a prominent feature. On the $z/D = 0.6$ plane, the dominant re-circulating region comprises of two repelling focal points. The first focal point is located at $x/D = 1.04$ and $y/D =$ -0.62. The

second is situated at $x/D = 1.62$ and $y/D =$ -0.44. A nodal point separates the two spirals and is situated at $x/D = 1.18$ and $y/D =$ -0.58. At $z/D = 0.95$, as shown in Figure 6.2(d), viscous forces now tend to dominate at the proximity of the cavity side wall at $z/D =$ 1.0. The main re-circulation region has two two focal points. In this case, the focal points are attractive spirals. The first point is located at $x/D = 0.88$ and $y/D =$ -0.7 and the second, closest to the aft cavity wall, is observed at $x/D = 1.62$ and $y/D =$ -0.56. The two focal points are separated by a non-orthogonal saddle point at $x/D = 1.26$ and $y/D =$ -0.54. The presence of a non-orthogonal saddle point indicates that in this region of the flow the rate of strain dominates over the rate of rotation. Thus the main re-circulating structure has bifurcated into two clockwise spirals of approximately the same dimension. The overall re-circulating flow is therefore clockwise. Figures 6.2(a) to 6.2(d) show that the position of the vortex core changes across the cavity span and indicates a warping of the vortex axis. The flow spiralling about the focal points indicates a spanwise vortex stretching.

Further information about the nature of the time-averaged flow is obtained through an examination of the pressure distribution along the cavity floor. The pressure distribution along the base of the cavity for each spanwise location discussed above is shown in Figure 6.3. Over the range $0 \leq z/D \leq 0.95$, the pressure distribution shows very little variation prior to the streamwise distance of $x/D = 0.6$ from the upstream cavity edge. The presence of a minimum and maximum in the static pressure distribution along the floor indicates the presence of a dominant re-circulating flow pattern inside the cavity. The re-circulating flow induces flow separation along the cavity floor and the separation points are dependent on the position of the re-circulating core. As previously seen in the sectional streamlines, the main re-circulating core is not fixed in position along the span, thus the minima and maxima in the pressure coefficient also change in location to account for this feature. Table 6.1 provides a summary of the location of the minimum and maximum in the C_p distribution corresponding to each spanwise position. A notable feature in the C_p plots is the pressure distribution for the spanwise locations of $z/D = 0.6$ and $z/D =$ 0.95. As seen in Figure 6.3, results at this spanwise location show the lowest and highest

peaks in the static pressure over the range $0 \leq z/D \leq 0.95$. At $z/D = 0.6$, it can be seen that the rise the in static pressure coefficient from $x/D = 1.0$ does not occur at a constant rate along the streamwise direction. There appears to be a small change in the gradient of the streamwise pressure distribution at $x/D = 1.4$. This is corresponds to the presence of the two focal points within the re-circulating flow pattern as shown in Figure 6.2(c). The highest peak in C_p occurs at the spanwise location of $z/D = 0.6$ and the position of this peak is given in Table 6.1. This is due to the fact that, at this location, the dominant re-circulating structure comprises of a very strong focal point close to the aft cavity edge, which tends to produce a high variation in the C_p. The pressure distribution follows very closely to that of an open cavity flow regime as reported by Plentovich *et al* [11].

The topological complexity of the flow cavity time-averaged flow pattern can be further elucidated through an examination of the flow pattern over a plane parallel to the cavity floor. The CFD data on the solid wall surfaces cannot be used to obtain a wall flow pattern, as non-slip boundary conditions are imposed on these surfaces. However, the flow can be visualized on a y-plane very close to the base. Specifically, the predictions from the $y = -0.99L$ plane are used. Thus, Figure 6.4 provides a representation of the flow pattern along the cavity floor. The cavity geometry was mirrored about the symmetry plane so as to represent a complete cavity geometry. Several noticeable features can be observed in this flow pattern. These are bifurcation lines and nodes. Close to the front cavity edge, a bifurcation line is observed at $x/D = 0.07$. This bifurcation line is the result of two counter rotating eddies close to the bottom front cavity corner. The two nodal points are formed by a pair of bifurcation lines on either side of the symmetry plane. These bifurcation lines are at $x/D = 0.7$ and are formed due to flow separation along the cavity floor. This separation is induced by the dominant re-circulating flow structure and the secondary structure close to the front cavity edge. The nodal points therefore correspond to the position of flow separation on the cavity floor at the symmetry plane. The pair of bifurcation lines aft of the nodes is a result of counter rotating eddies at the bottom rear corner of the cavity. The large region of reverse flow along the cavity floor aft of the nodal points therefore correspond to the region of the flow which is dominated by the large re-

circulation structures. It can be observed that the bifurcation lines are warped across the cavity span. This again corresponds to the fact that vortex stretching in the spanwise direction occurs. A clearer picture to explain the topological features of the cavity floor flow pattern is to examine the streamwise sectional streamlines in conjunction with the base flow patter as shown in Figure 6.5. In this figure it can be observed that the flow separation positions along the cavity floor on the $z/D = 0.95$ plane do indeed coincide with the positions of the bifurcation lines. The separation points are labelled in Figure 6.5.

6.6 Unsteady Flow Field

As in the 2D cases discussed in Chapter 4, the flow over the 3D cavity is dominated by the behaviour of the shear layer. To understand the physical nature of the predicted shear layer oscillation modes and the associated frequencies, the time-dependent static pressure on the cavity floor was monitored at $x/D = 1.0$ and $z/D = 0$. The spectral contents of the unsteady pressure signal were obtained through a discrete Fourier transform (DFT) using the same method as in Chapter 4.

The spectral content of the pressure signal obtained for the $L/D = 2$, $W/D = 2$ cavity is shown in Figure 6.6. The $\Delta St = 0.0012$ constant bandwidth spectrum is plotted in terms of the sound pressure level and the non-dimensional frequency. The Strouhal number was scaled with the cavity length as the characteristic physical dimension. The first sub-harmonic of the Rossiter mode 1 of oscillation is noticed at a Strouhal number of 0.2. The Rossiter mode 1 appears in the spectrum at a Strouhal number of 0.38. The amplitude of this broad peak is 139.2 dB. The peak at the Strouhal number of 0.58 corresponds to a non-integer multiple of the the first Rossiter mode. This arises due to the complex nature of the hydrodynamic interaction which occurs at the cavity trailing edge as explained by Rockwell and Knisely [34]. The amplitude of this peak is 3.2 dB lower than that of the first Rossiter mode. The second Rossiter mode occurs at a Strouhal number of 0.78 and its amplitude is much lower than the first mode one, with a peak of 106.2 dB. It can be

seen that higher frequency harmonics are also present but it is clear from the spectrum that the overall dominant mode is the Rossiter mode 1.

To visualize the unsteady flow features, the iso-contours of the Q-criterion at four instances of time over one period of oscillation are shown in Figure 6.7. The Q-criterion is defined as

$$Q = \frac{1}{2}(\Omega_{ij}\Omega_{ij} - S_{ij}S_{ij}) \tag{6.1}$$

where Ω_{ij} and S_{ij} are the anti-symmetric and symmetric components of the velocity gradient tensor. The definition for Ω_{ij} is given in equation (2.21) and $S_{ij} = \partial u_i/\partial x_j + \partial u_j/\partial x_i$. Regions of high Q values identify regions of the flow where vorticity dominates over strain rate. Thus a vortex is locally identified as the topological flow structure where the local rate of rotation is higher than the local rate of strain. The time dependent behaviour of the shear layer is very similar to the 2D cases studied in Chapter 4. The incoming boundary layer separates at the upstream cavity edge and leads to the formation of the shear layer. In the 2D cavity flow simulations, instabilities within the shear layer grow leading to the formation of large scale vortical structures. In the 3D case, these structures take the form of a tubular vortex that spans the entire cavity width. This feature is evident in Figure 6.7. The flow sequence in Figures 6.7(a) to 6.7(d) shows one characteristic cavity flow period of the Rossiter 1 Strouhal number. As the flow evolves downstream of the cavity, such structures interact with the cavity trailing edge generating disturbances that travel upstream to the leading edge. The feedback loop for self-sustained oscillation is thus closed. The warping of the vortex core axis as explained in Section 6.5 is now observed in Figure 6.7 as the large coherent structures evolve within the shear layer. This is a consequence of the side walls providing additional viscous stresses which retard the evolution of the vortical structures as they convect downstream.

The impingement of a vortical structure on the cavity trailing edge can be observed in Figure 6.7(a). At the same time, another such structure is formed within the shear layer.

Streamwise structures are also evident at the rear cavity corners where the flow exits the cavity opening. An examination of Figure 6.7 shows that at any instant in time, only one large scale structure is present in the shear layer. This corresponds to the dominant Rossiter mode 1 of the cavity flow oscillation. However, the pressure spectrum in Figure 6.6 indicated that there is a degree of low frequency modulation of the fundamental mode. This implies that the nature of the vortex-edge interaction is more complex than in the 2D cases. It can be observed that the incident vortex in Figure 6.7(a) escapes from the cavity largely undeformed in the vicinity of the mid span region. Close to the side walls, this structure no longer retains its original coherence and is severely distorted, where a portion is swept back inside the cavity and another portion entrained in the streamwise rotational flow observed at the rear corners. In the 3D case therefore, it is not possible to define the vortex-edge interaction as clearly as in the 2D case as the nature of the interaction varies strongly along the span of the cavity trailing edge.

6.6.1 Acoustic field

The 3D acoustic field is visualized through the instantaneous density perturbation contours in three planes. Figure 6.8 shows the acoustic radiation in the $x-y$ plane at $z/D = 0.0$. Consistent with the 2D cases, it displays a stronger radiation pattern in the upstream direction. This is also confirmed in Figure 6.9 which shows the radiation pattern in the horizontal $x-z$ plane at $y/D = 0.2$. In this figure, it can be seen that the radiation in the spanwise directions are much weaker than in the upstream direction. The acoustic radiation in the vertical $y-z$ plane is shown in Figure 6.10. It can be seen that, in this plane, the strongest radiation is directly above the cavity opening. In this figure, the spanwise distortion of the shear layer is also evident. This undulation, in most likelihood, can give rise to spanwise oscillation modes.

To predict the sound radiation pattern in the far-field, an integral surface solution of the FW-H equation is sought. Integration surfaces through $x-z$ planes at $y/D = 3.0$, 4.0 and 5.0 were employed. The spanwise extent of each surface was $2D$ and the streamwise ex-

tent was $10D$. The observers are placed in the far field at 200 cavity depths ($200D$) from the cavity mouth about $z/D = 0.0$. The cavity centre point is taken at the mid-length distance with angular measurements in the counter-clockwise direction going from 0 degrees from the aft corner to 180 degrees to the leading edge corner. The computed directivity pattern is shown in Figure 6.11. The FW-H computation is in general agreement with the near-field observation in regards to the directivity. The preferred directivity is in the upstream direction at a polar angle of 112.2 degrees. The radiation in the forward arc is much weaker, for instance, an amplitude of 80.2 dB is predicted at at a polar angle of 62.4 degrees. The three integration surfaces employed did not display much sensitivity to the y/D position. There is approximately 0.8 dB of discrepancy in the rear arc directivity observed from the integration surface located at $y/D = 3.0$ compared the one at $y/D = 5.0$. A small sensitivity of the integral solution to the location of the integration is to be expected due to the fact that the volume enclosed by each surface is slightly different and will account for marginally different volumetric source contributions.

In a previous investigation by Ashcroft [87], the observations in the far-field for the laminar case (for observer positions at $200D$ from the cavity) indicated that the preferred directivity corresponded to a polar angle of 120 degrees. This was due to the dominant Rossiter mode 2 of the shear layer oscillation. In the present study, the flow was computed as fully turbulent. The dominant mode of the shear layer oscillation was the Rossiter mode 1 and its contribution to the far-field is a possible cause for the lower directivity angle.

6.7 Summary

The flow over a 3D cavity of $L/D = 2$ was studied using a DES turbulence model. The time-averaged flow predictions displayed significant three-dimensionality with a topology indicating the presence of critical points which are inherently 3D features. There was a significant variation of the time-averaged flow pattern across the cavity span. The time-averaged flowfield is dominated by a large re-circulation structure as in the 2D cases. The

time-dependent flow was likewise dominated by the behaviour of the shear layer. It was found that the dominant mode of oscillation at the selected geometry and flow conditions was the Rossiter mode 1, although other modes were also present at significantly lower amplitudes. The existence of the cavity side walls introduced a warping of the main vortex axis along the span of the cavity. As a result, the nature of the vortex-edge interaction varies along the span of the cavity trailing edge. Streamwise structures were also observed at the cavity corners. The sound field radiation was shown in three planes where the strongest radiation were shown to be in the upstream and vertical directions. The radiation in the spanwise directions was seen to be the weakest. The predicted far-field directivity confirms the near-field observations that the upstream radiation is the preferred radiation direction.

z/D	$(C_p)_{min}$	$(C_p)_{max}$
0.0	$x/D = 1.32$	$x/D = 1.92$
0.2	$x/D = 1.26$	$x/D = 1.86$
0.6	$x/D = 1.00$	$x/D = 1.88$
0.95	$x/D = 1.04$	$x/D = 1.72$

Table 6.1: Maxima and minima of pressure coefficients for different spanwise locations

6.8 Chapter 6 Figures

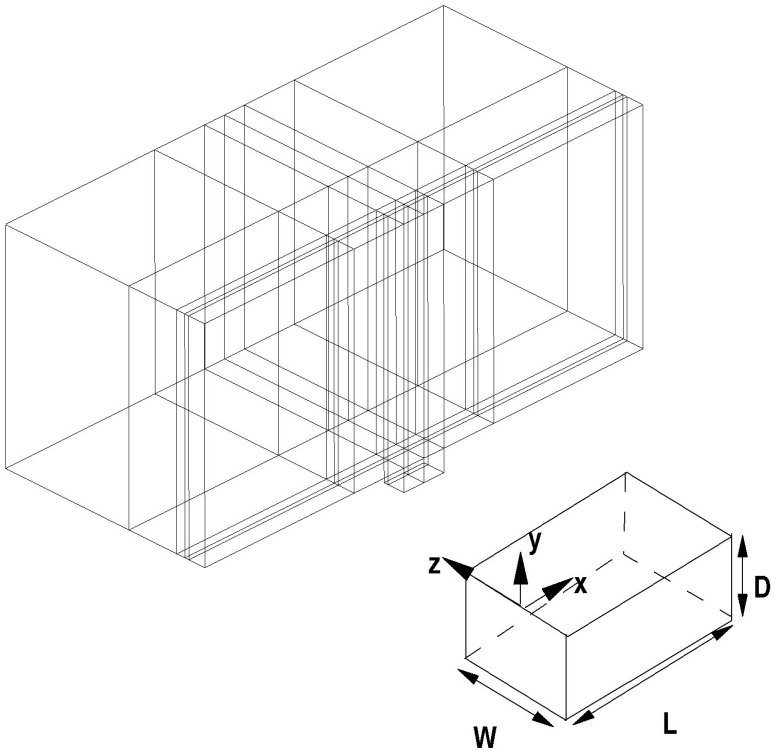

Figure 6.1: 3D cavity geometry.

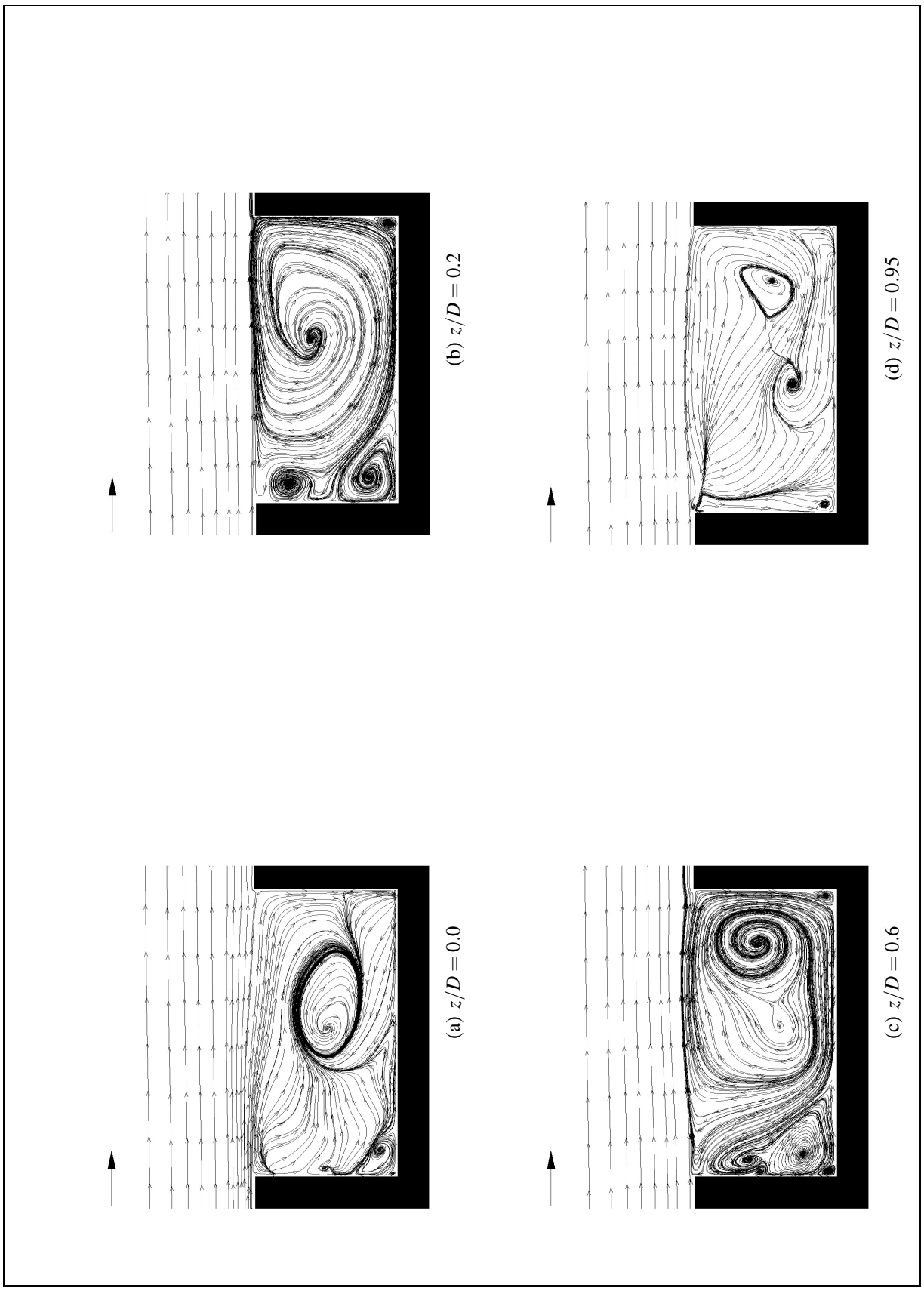

Figure 6.2: Time averaged sectional streamlines across the cavity span, flow from left to right.

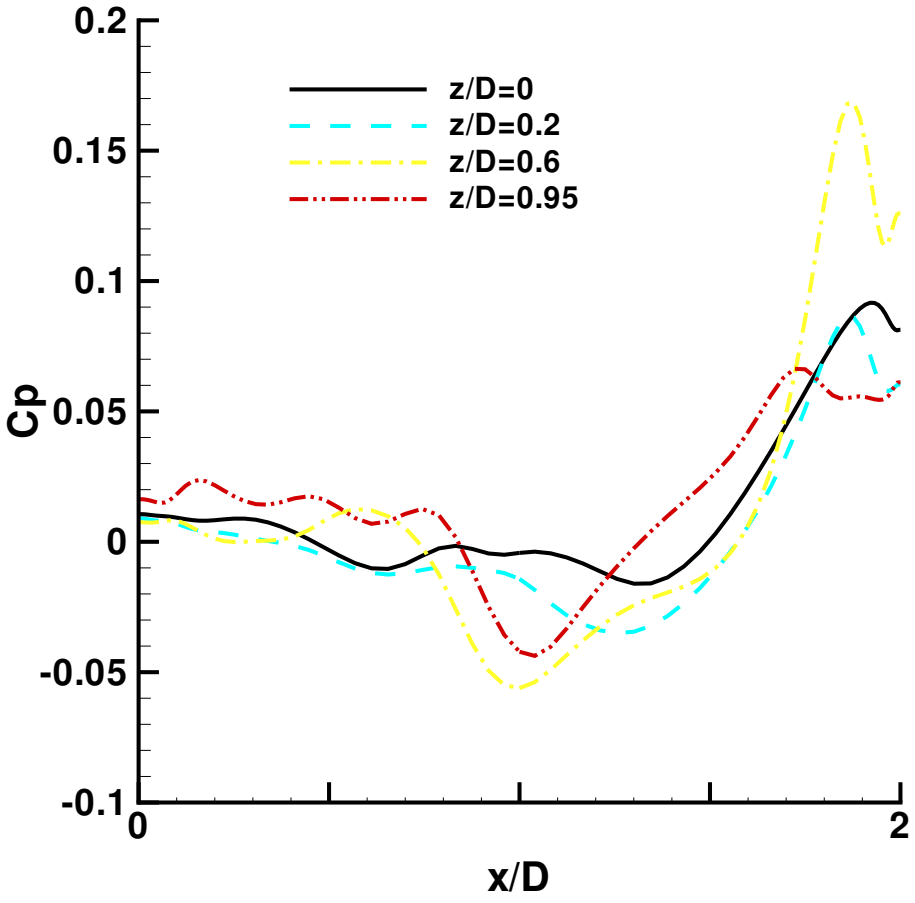

Figure 6.3: Static pressure distribution along the cavity floor at different spanwise locations.

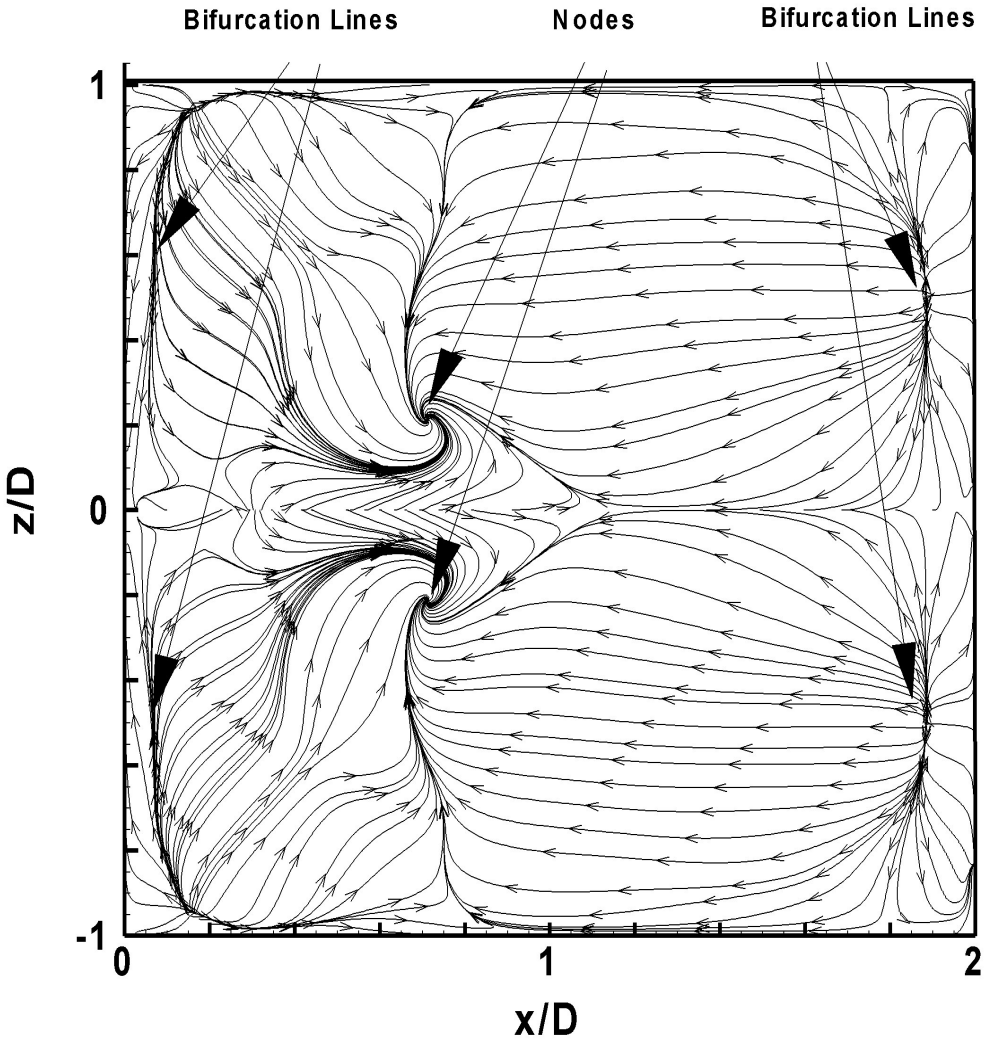

Figure 6.4: Flow pattern along the cavity floor, flow from left to right.

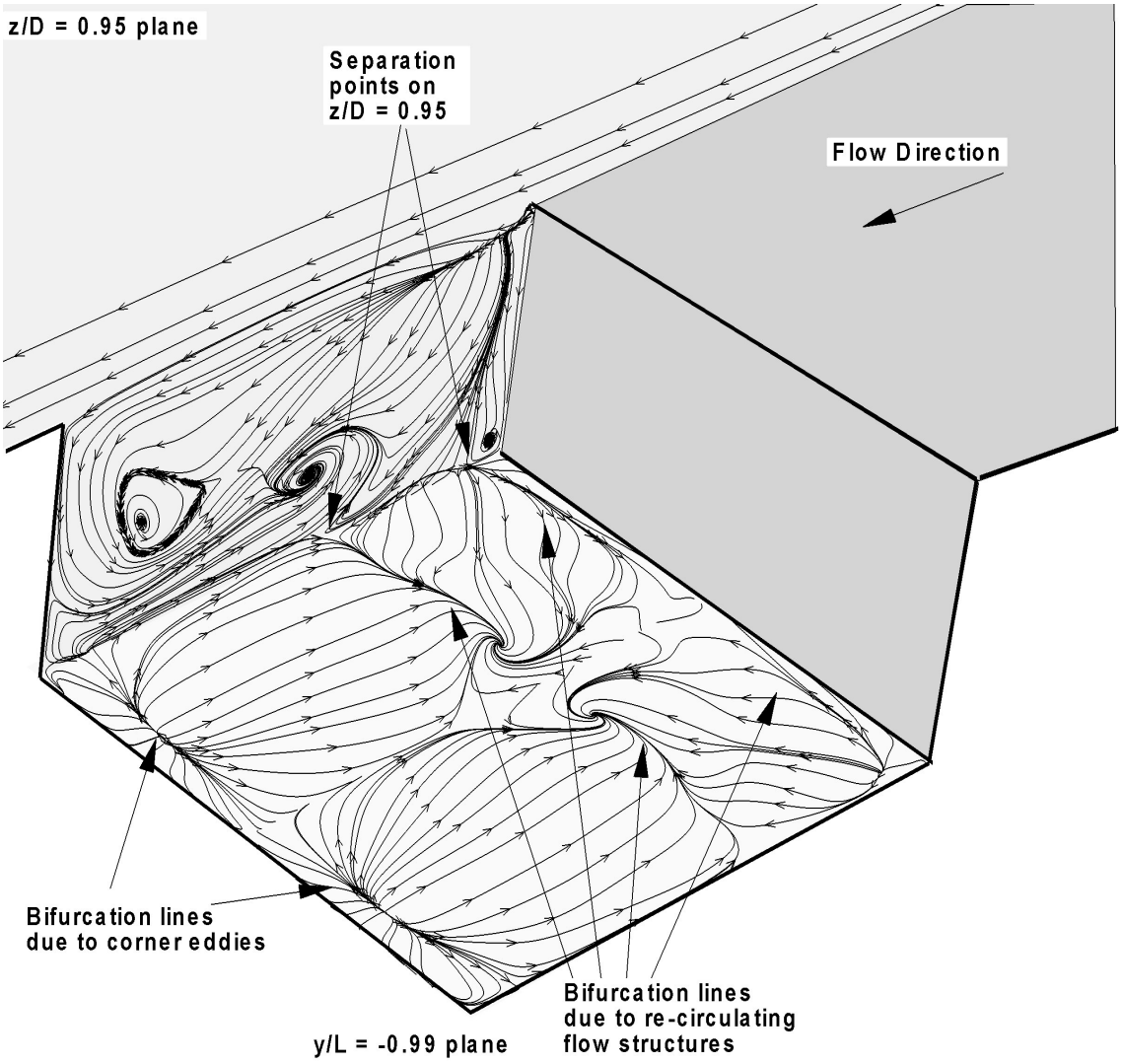

Figure 6.5: Flow visualization along the cavity floor and vertical plane corresponding to $z/D = 0.95$.

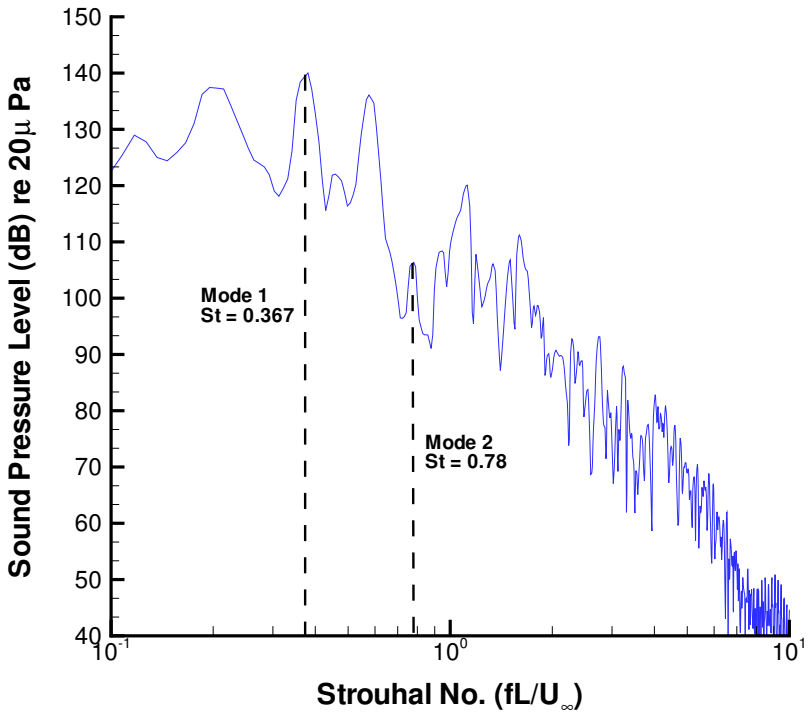

Figure 6.6: Sound Pressure Level in dB, $L/D = 2$, $W/D = 2$, $x/D = 1.0$, $\Delta St = 0.0012$.

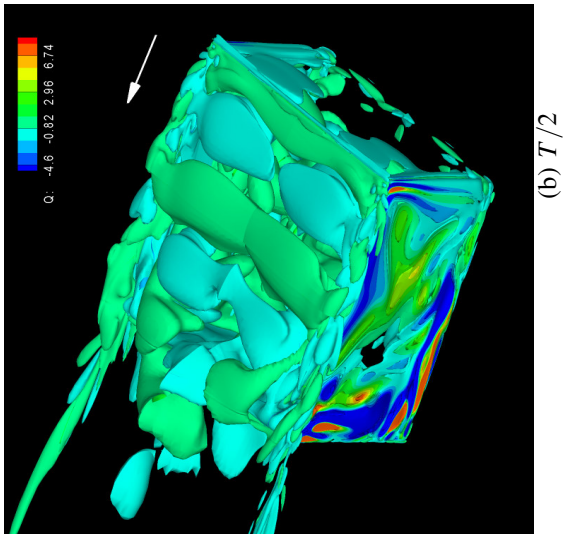

(b) $T/2$

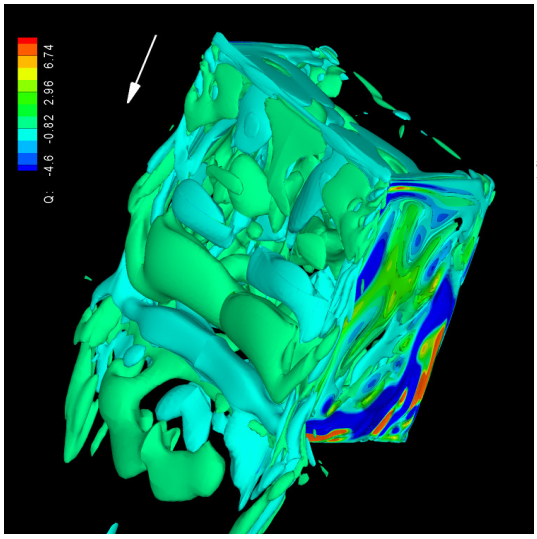

(d) T

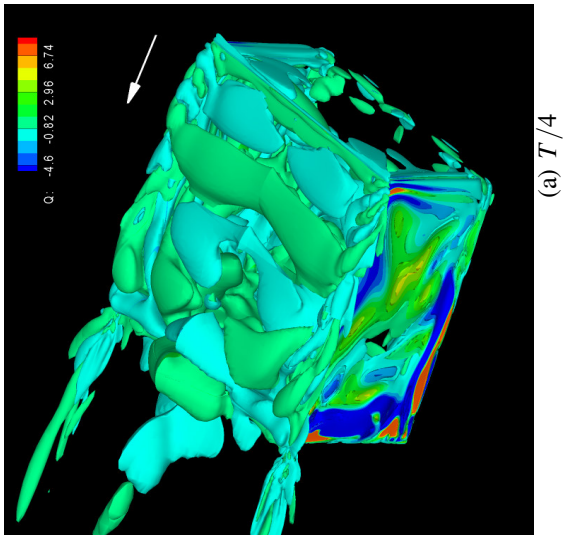

(a) $T/4$

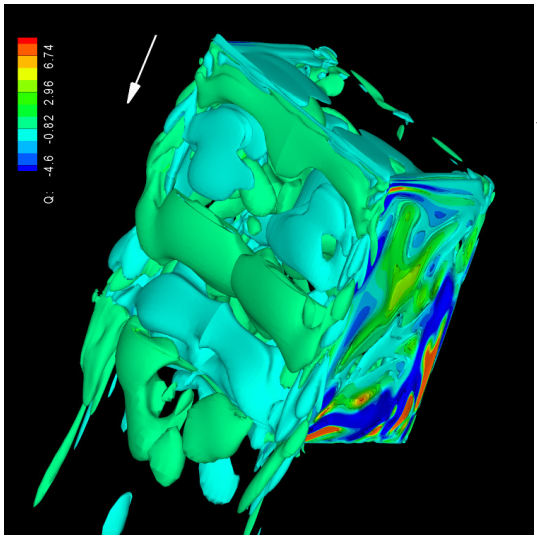

(c) $3T/4$

Figure 6.7: Q-criterion visualization describing three-dimensional cavity time-dependent flow ; $M_\infty = 0.4$.

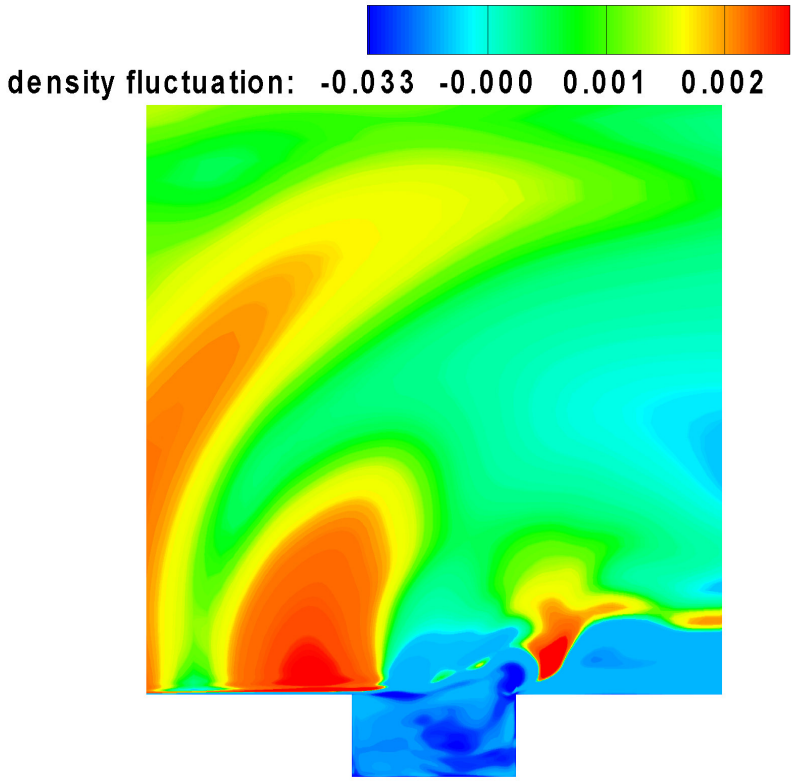

Figure 6.8: Instantaneous density fluctuation ($\rho/\rho_\infty - 1$): $x-y$ plane, $z/D = 0.0$.

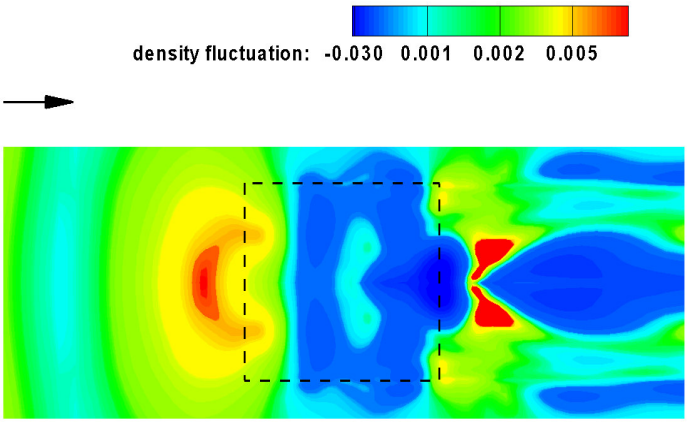

Figure 6.9: Instantaneous density fluctuation ($\rho/\rho_\infty - 1$): $x-z$ plane, $y/D = 0.2$.

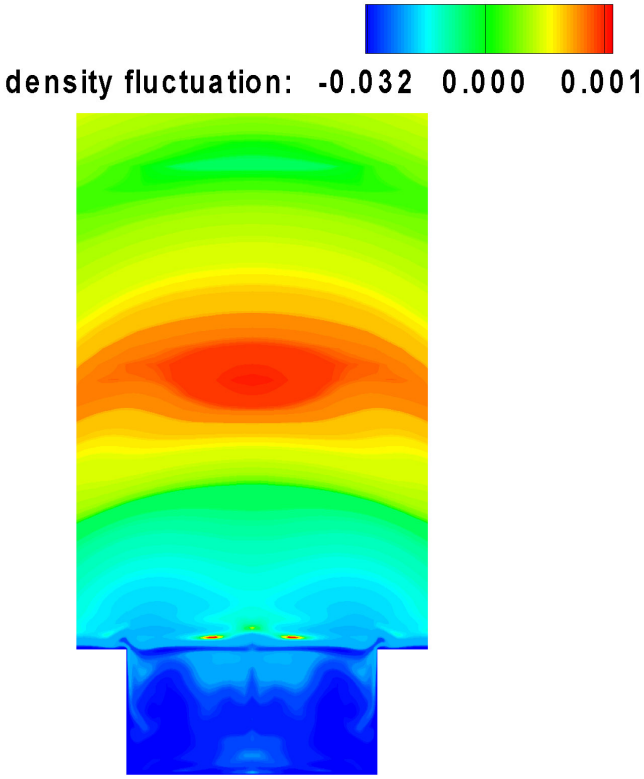

Figure 6.10: Instantaneous density fluctuation ($\rho/\rho_\infty - 1$): $y-z$ plane, $x/D = 1.0$.

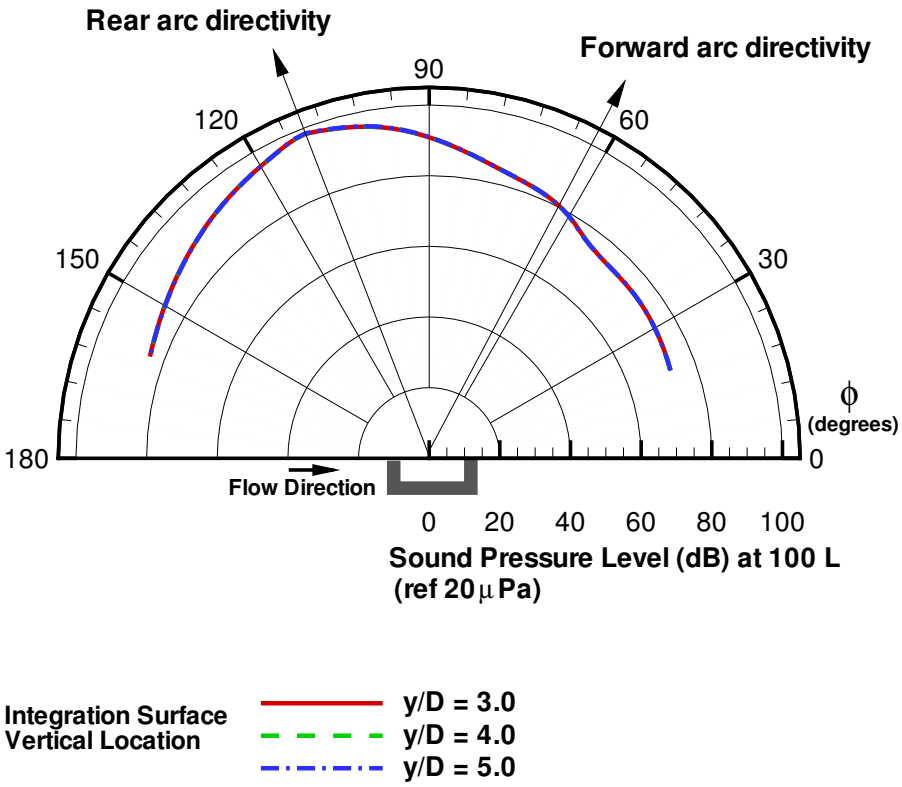

Figure 6.11: Acoustic field directivity at 100L in the $x-y$ plane about $z/D = 0.0$.

Chapter 7

Conclusions and Recommendations

7.1 Overview

Numerical and experimental studies of 2D and 3D cavities were performed using high-order CAA algorithms and non-intrusive measurement techniques. This final chapter draws conclusions on the basis of the main results predicted in Chapters 4 to 6. Recommendations for future research activities are also proposed.

7.2 Summary of Results

The aim of this research was to extend the knowledge on self-sustaining oscillatory cavity flows. The focus of this thesis was to explore the relation between the changes in geometrical parameters of the cavity, namely, L/D and W/D and the flow. The main results are summarized below.

7.2.1 Numerical aspects

The implementation of the Navier-Stokes equations was performed using an optimized high-order-accurate compact finite difference scheme and a high-order Runge-Kutta explicit time integration . A wavenumber based optimization procedure was applied by Ashcroft and Zhang [74] to extend the Hixon [73] scheme to a wider class of compact scheme. Non-reflecting buffer-zone boundary conditions were also employed to damp spurious numerical waves. The Spalart-Allmaras one-equation turbulence model was implemented to provide the eddy viscosity closure to the Favre averaged Navier-Stokes equations. Through a modification of the wall distance length scale, a DES method was implemented. A parallel implementation of the code was achieved through the Message Passing Interface. Code validation was performed against benchmark cases for laminar and turbulent boundary layers. The results provided confidence in the calculation of the viscous and Reynolds stresses in the Navier-Stokes equations.

7.2.2 Physical aspects

- Initial computations on cavity geometries were performed in the laminar flow regime to gain an understanding of the requirements for the computational grid and hence the computational effort necessary to achieve satisfactory results in the simulation of cavity flows. Therefore a 2D cavity of $L/D = 2$ was chosen for a grid sensitivity study. It was concluded that a mesh comprising of 576,000 nodes would be necessary to resolve the shear layer and maintain the points per wavelength required to propagate acoustic waves away from the cavity opening with and acceptable numerical dissipation and dispersion. This numerical experience also provided the basis for the construction of the computational grid for the final 3D simulation.

- A number of 2D cavities were subsequently studied. The same flow conditions were employed in all cases while the length-to-depth ratio was varied between 2 and 10. The flow regime was classified according to the characteristics of the time averaged surface pressures along the cavity floor. The flow regime varied from ‘open’, ‘tran-

sitional' to 'closed'. It was found that the computed oscillation tonal frequencies agree with the Rossiter model. The amplitudes of these modes were dependent on the nature of the vortex-edge interaction. The interaction varied from 'complete-clipping' for cavities of $L/D = 2$ and 4 and to 'partial-clipping' for $L/D = 5$. On the other hand, 'vortex-escape' was observed for $L/D = 8$ and 10. The directivity and amplitude of the sound field in the far-field was obtained through the integral solution of the FW-H equation. The directivity patterns seem to indicate that there is a direct relationship between the nature of the vortex-edge interaction and the preferred radiation angle of the cavity.

- Experimental measurements were performed to characterise the flow over 3D cavities. The different cases studied were cavities of $L/D = 4$ with different spanwise dimension of $W/D =$ 3, 2, 1.5 and 1. For this purpose, instantaneous velocity data were acquired non-intrusively through 2D PIV. Surface oil flow visualisation was also employed as a means to study the topology of the near-wall flow structure. Flow features observed through the surface oil visualisation confirmed the existence of significant three-dimensionality within the cavities. The cavities of $W/D = 3$ and 2 displayed a symmetrical behaviour about the cavity centreline with two cellular structures located in the leading portion of the cavity. The other cases displayed an asymmetrical flow pattern with only one cellular structure. The surface oil flow was in close agreement with velocity measurements performed in a horizontal plane close to the cavity floor. Time averaged flow patterns in vertical planes described large-scale re-circulating flow patterns that constituted the dominant flow feature in all the cases. The mean re-circulation centre positions were observed to change with spanwise distance. The time-resolved flow was analyzed through a Large Eddy decomposition followed by Galilean transformation of the velocity field. This provided a means to study the large-scale structures as they convect along the shear layer and also indicate the nature of the vortex-edge interaction that occur in the 3D cases. It was found that the vortex-edge interaction at $W/D = 1.0$ and 3.0 was highly irregular. This suggested that the 'vortex-jitter' regime occurred at the cavity trailing edge.

- A numerical investigation was conducted on a 3D cavity of $L/D = 2$ and $W/D = 2$ at a freestream Mach number was 0.4. From the experiments in Chapter 5, it was evident that a symmetrical flow behaviour existed for the cavity of $W/D = 2$. Therefore only half the cavity was simulated. The analysis of the time-resolved pressure monitored on the cavity floor provided an indication of the dominant oscillation modes of the cavity shear layer. The presence of the cavity side walls introduced a warping of the main vortex axis along the spanwise directions. Observations of the unsteady flow indicated that the nature of the vortex-edge interaction varied along the cavity span. Plots of the near-field density fluctuations depicted a 3D sound field. The sound radiated in the far-field was observed to follow a preferred directivity in the upstream direction.

7.3 Main Research Outcomes

- The current study combined the use of numerical methods and experimental techniques to study the flow over rectangular cavities. While it is difficult to point a specific contribution to the field of cavity flow physics in the present work, the main outcomes of the research are outlined herewith.

- The development of a 3D parallel computational tools using high-order numerical methods which allows the prediction of aerodynamic noise sources in the near-field. The main contribution is an understanding of the issues of relevance to CAA, such as non-reflecting boundary conditions, high-order finite difference method and high-order time integration schemes. The code is still in use and has been extended to other applications, such as high lift devices noise prediction.

- An attempt to link the near-field flow to the far-field sound for 2D cavities. It was found that the directivity of the radiated sound is directly dependent on the L/D of the cavity. The amplitude of the sound field was also found to be directly dependent on the L/D and the cavity flow regime. The amplitude of the sound was found to be highest when the cavity flow was in the transitional regime. The present study

therefore provides evidence that the sound field directivity and amplitude depends on the cavity flow regime.

- An exploration of 3D cavity flows using PIV and the implemented numerical tool. A number of 3D cavities with W/D in a range of 3 to 0.5 were studied. PIV showed that at large W/D, the time-averaged flow was symmetrical about the cavity mid-span. Oil flow visualisation revealed a complex flow near-wall flow structure. The time-resolved PIV showed a complex interaction of the shear layer with the cavity trailing edge, indicating that 'vortex-jitter' characterises the nature of the interactions. The numerical study attempted to link the near-field observations to the far-field sound. The predicted far-field directivity matched the near-field observations. The predictions also agreed with the trend observed in the open cavity flow regime in the $2D$ computations. The present study therefore provides an overview and furthers the understanding of three-dimensionality in cavity flows using both experiments and simulations.

7.4 Scope for Future Research

Several points have been identified in the present study that warrant further research.

- Any simulation code needs to undergo a rigorous validation procedure. In the present study, only a limited validation was carried out against time-averaged results for the viscous part of the Navier-Stokes equations. Future activities should aim at performing an extensive validation of the code against the available experimental databases. The experimental results in the present study could form a starting point to validate the near-field flow. For the unsteady physics, in particular the predicted unsteady pressure spectra, unsteady pressure tranducers could be employed in future investigations to compare the pressure spectra obtained using the code. The validation activities could also be performed on other test cases such as bluff body geometries.

- One interesting study would be to investigate the effect of W/D on the far-field sound. The directivity and intensity of the sound in the far-field could be affected by the change in W/D. A numerical investigation could be based around the experimental measurements already acquired in this study. It would provide a database against which to compare the near-field computations. The far-field analysis based on the FW-H formulation could then be obtained for the different cases. Once the experience on the baseline cavities has been achieved, studies on cavity flow control could be performed to study the effects on the flow features and far-field sound.

- The implementation of the DES method was based on the original formulation proposed by Sparlart [68]. However, DES has been subject to numerous debates about its accuracy and potential pitfalls associated with artificial separation due to ambiguous grid densities where the model cannot distinguish between an attached boundary layer and the separated flow [93]. This issue is particularly acute for problems involving thick boundary layers and near isotropic grid spacing parallel to the wall. To tackle this problem, Spalart *et al* [93] have proposed a modified version of the DES method, called Delayed DES (DDES). Other more sophisticated models such as hybrid RANS/LES methods with spectral enrichment have also been developed since the formulation of the original DES idea. It would be valuable to test these more advanced turbulence modeling strategies on a cavity flow problem to assess whether they give any predictive improvement of flowfield and acoustics. It has become evident that there is a need to define the suitability of turbulence modeling schemes for CAA applications and therefore such a parametric study would be extremely useful.

Bibliography

[1] J.E. Gibson. *An Analysis of Supersonic Cavity Flow*. Ms Thesis, MIT Dept. of Aeronautics and Astronautics, 1958.

[2] H.H. Hubbard. *Aeroacoustics of Flight Vehicles - Theory and Practice*, volume 1. Acoustical Society of America, 1995.

[3] H.H. Heller and W.M. Dobrzynski. Sound radiation by aircraft wheel well/landing gear configurations. *Journal of Aircraft*, 14(8):768–774, 1977.

[4] M.S. Howe. On the helmholtz resonator. *Journal of Sound and Vibration*, 76(4):427–440, 1976.

[5] P.A. Nelson, N.A. Halliwell, and P.E. Doak. Fluid dynamics of a flow excited resonance. *Journal of Sound and Vibration*, 91(3):375–402, 1983.

[6] M.E. Franke and D.L. Carr. Effect of geometry on open cavity flow induced pressure oscillations. AIAA Paper 75-0492, 1975.

[7] C.W. Rowley, T. Colonius, and A.J. Basu. On self-sustained oscillations in two-dimensional compressible flow over rectangular cavities. *Journal of Fluid Mechanics*, 455:315–346, 2002.

[8] C.W. Rowley, T. Colonius, and R.M. Murray. POD based models for self-sustained oscillations in the flow past an open cavity. AIAA Paper 2000-1969, 2000.

[9] A. Roshko. Some measurements of flow in a rectangular cutout. *NACA Tech. Note*, 3488, 1955.

[10] A.F. Charwat, J.N. Roos, F.C. Deweg Jr., F.C., and J.A. Hitz. An investigation of separated flows. *Journal of Aerospace Sciences*, 28(6,7):457–470, 1961.

[11] E.B. Plentovich, R.L. Stallings Jr., and M.B. Tracey. Experimental cavity pressure measurements at subsonic and transonic speeds. NASA TP 3358, 1993.

[12] D.J. Maull and L.F. East. Three dimensional cavities. *Journal of Fluid Mechanics*, 16:620–632, 1963.

[13] C.H. Kuo and S.H. Huang. Influence of flow path modification on oscillation of cavity shear layers. *Experiments in Fluids*, 31(2):162–178, 2001.

[14] M.B. Tracy and E.B. Plentovich. Characteriation of cavity flow fields using pressure data obtained in the langley 0.3 meter trasnsonic cryogenic tunnel. NASA TM 4436, 1993.

[15] V. Sarohia. Experimental oscillations in flows over shallow cavities. *AIAA Journal*, 15(7):984–991, 1977.

[16] K. Karamcheti. Acoustic radiation from two-dimensional rectangular cutouts in aerodynamic surfaces. NACA TR 3487, 1955.

[17] H.E. Plumblee, J.S. Gibson, and L.W. Lassiter. A theoretical and experimental investigation of the acoustic response of cavities in an aerodynamic flow. US Air Force Report WADD-TR-61-75, 1962.

[18] J.E. Rossiter. Wind tunnel experiments on the flow over rectangular cavities at subsonic and transonic speeds. *Aeronautical Research Council Reports and Memoranda*, 3438, 1964.

[19] L.F. East. Aerodynamically induced resonance in rectangular cavities. *Journal of Sound and Vibration*, 3:277–287, 1966.

[20] H.H. Heller, D.G. Holmes, and E.E Covert. Flow induced pressure oscillations in shallow cavities. *Journal of Sound and Vibration*, 18:545–553, 1971.

[21] A.J. Bilanin and E.E. Covert. Estimation of possible excitation frequencies for shallow rectangular cavities. *AIAA Journal*, 11:347–351, 1973.

[22] C.K.W. Tam and P.J.W. Block. On the tones and pressure oscillations induced by flow over rectangular cavities. *Journal of Fluid Mechanics*, 89(2):373–399, 1978.

[23] H.H. Heller and D.B. Bliss. The physical mechanism of flow induced pressure fluctuations in cavities and concepts for their suppression. AIAA Paper 75-491, 1975.

[24] M. Gharib and A. Roshko. The effect of flow oscillations on cavity drag. *Journal of Fluid Mechanics*, 177:501–530, 1987.

[25] V. Theofilis, P. W. Duck, and J. Owen. Viscous linear stability analysis of rectangular ducts and cavity flows. *Journal of Fluid Mechanics*, 505:249–286, 2004.

[26] E.B. Plentovich. Three dimensional cavity flow fields at subsonic and transonic speeds. NASA TM 4209, 1990.

[27] M.B. Tracy and E.B. Plentovich. Cavity unsteady pressure measurements at subsonic and transonic speeds. NASA TP 3669, 1997.

[28] K.K. Ahuja and J. Mendoza. Effects of cavity dimensions, boundary layer, and temperature in cavity noise with emphasis on benchmark data to validate compuational aeroacoustic codes. NASA CR 4653, 1995.

[29] J.C. Lin and D. Rockwell. Organised oscillations of initially turbulent flow past a cavity. *AIAA Journal*, 39(6):1139–1151, 2001.

[30] D. Rockwell and E. Naudascher. Self-sustained oscillations of impinging free shear layers. *Annual Review in Fluid Mechanics*, 11:67–94, 1979.

[31] A. Powell. On the edge tone. *Journal of the Acoustical Society of America*, 33(4):395–409, 1961.

[32] C. Rowley, D.R. Williams, T. Colonius, R.M. Murray, and D.G. Macmynowski. Linear models for control of cavity flow oscillations. *Journal of Fluid Mechanics*, 547:317–330, 2006.

[33] M.V. Morkovin and S.V. Paranjape. On acoustic excitation of shear layers. *Z. Flugwiss*, 8/9(2), 1971.

[34] D. Rockwell and C. Knisely. The organised nature of flow impingment upon a corner. *Journal of Fluid Mechanics*, 93:413–432, 1979.

[35] W.L. Hankey and J.S. Shang. Analyses of pressure fluctuations in an open cavity. *AIAA Journal*, 18(8):892–898, 1980.

[36] C.J. Tam, P.D. Orkwis, and P.J. Disimile. Comparison of Baldwin-Lomax turbulence model for two-dimensional open cavity computations. *AIAA Journal*, 34(3):2255–2260, 1995.

[37] S.A. Slimon, D.W. Davis, and C.A. Wagner. Far-field aeroacoustic computation of unsteady cavity flow. AIAA Paper 98-0285, 1998.

[38] D.P. Rizetta. Numerical simulation of supersonic flow over three dimensional cavity. *AIAA Journal*, 26(7):799–807, 1988.

[39] I. Kim and N. Chokani. Navier-Stokes simulation of unsteady supersonic cavity flow field with passive control. AIAA Paper 90-3101-CP, 1990.

[40] O. Baysal, G.W. Yen, and K. Fouladi. Navier-Stokes computations of cavity aeroacoustics with suppression devices. *14th AIAA/DGLR Aeroacoustics Conference, Aachen, Germany*, 2:940–948, 1992.

[41] X. Zhang, A. Rona, and J.A. Edwards. An observation of pressure waves around a shallow cavity. *Journal of Sound and Vibration*, 214(2):771–778, 1998.

[42] N. Sinha and L.S. Ukeiley. High fidelity simulation of weapons bay aeroacoustics and active flow contol. AIAA Paper 2000-1968, 2000.

[43] N. Sinha, S. Arunajatesan, and J.M. Seiner. High fidelity simulation and measurements of aircraft weapons bay dynamics. AIAA Paper 2001-2125, 2001.

[44] B.I. Soemarwoto and J.C. Kok. Computations of three dimensional unsteady cavity flow to study the effect of different downstream geometries. *AGARD RTO-AVT Symposium on Development in Computational Aero- and Hydroacoustics, Manchester, UK*, 2001.

[45] T. Kestens. *Êtude Numerique du Controle Adaptif Multivoies des Instabilites Aeroacoustique des Cavités*. Thèse de Doctorat, Institut National Polytechnique de Toulouse, 1999.

[46] O. Labbé, B. Troff, and P. Sagaut. Direct numerical simulation of flow in an open cavity. *4th ECCOMAS - Computational Fluid Dynamics Conference*, 1998.

[47] H.H. Heller and J. Delfs. Cavity pressure oscillations: The generating mechanism visualised. *Journal of Sound and Vibration*, 196(2):248–252, 1996.

[48] X. Zhang. Compressible cavity flow oscillations due to shear layer instabilities and pressure feedback. *AIAA Journal*, 33(8):1404–1411, 1995.

[49] X. Zhang and J.A. Edwards. Computational analysis of unsteady cavity flows driven by thick shear layers. *Aeronautical Journal*, 92(919):365–374, 1988.

[50] X. Zhang and J.A. Edwards. An investigation of supersonic oscillatory cavity flows driven by a thick shear layer. *Aeronautical Journal*, 94(940):355–364, 1990.

[51] X. Zhang and J.A. Edwards. Experimental investigation of supersonic flow over two cavities in tandem. *AIAA Journal*, 30(5):1182–1190, 1992.

[52] A. Rona and W. Dieudonné. A flow-resonant model of transonic laminar open cavity instability. AIAA Paper 2000-31123, 2000.

[53] A. Rona and E.J. Brooksbank. POD analysis of cavity flow instability. AIAA Paper 2003-178, 2003.

[54] A. Rona. Control of transonic cavity flow instability by streamwise air injection. AIAA Paper 2004-682, 2004.

[55] T. Colonius, A.J. Basu, and C.W. Rowley. Numerical investigation of flow past a cavity. AIAA Paper 99-1912, 1999.

[56] C.M. Shieh and P.J. Morris. Parallel numerical simulation of subsonic cavity noise. AIAA Paper 99-1891, 1999.

[57] T. Colonius, A.J. Basu, and C.W. Rowley. Computation of sound generation and flow/acoustic instabilities in the flow past an open cavity. FEDSM99-7228, 1999.

[58] C.M. Shieh and P.J. Morris. Parallel computational aeroacoustic simulation of turbulent subsonic cavity flow. AIAA Paper 2000-1914, 2000.

[59] G. Ashcroft, K. Takeda, and X. Zhang. Computational modeling of aeroacoustics of a door cavity flow oscillation. *7th International Congress on Sound and Vibration, Garmisch-Partenkirchen, Germany*, 2000.

[60] G. Ashcroft, K. Takeda, and X. Zhang. Computations of self-induced oscillatory flow in an automobile door cavity. *3rd Computational Aeroacoustics Workshop, Ohio, Cleveland*, 1999.

[61] B. Henderson. Automobile noise involving feedback- sound generation by low speed cavity flows. *3rd Computational Aeroacoustics Workshop, Ohio, Cleveland*, 1999.

[62] X. Gloerfelt, C. Bogey, C. Bailly, and D. Juve. Aerodynamic noise induced by laminar and turbulent boundary layers over rectangular cavities. AIAA Paper 2002-2476, 2002.

[63] L. Larchevêque, P. Sagaut, I. Mary, and O. Labbé. Large eddy simulation of a compressible flow past a deep cavity. *Physics of Fluids*, 15(1):193–210, 2003.

[64] L. Larchevêque, T.H. Le, and P. Sagaut. Large eddy simulations of flow in weapons bays. AIAA Paper 2003-778, 2003.

[65] J.E. Ffowcs Williams and D.L. Hawkings. Sound generation by turbulence and surfaces in arbitrary motion. *Philisophical Transactions of the Royal Society of London*, 264(1151):321–342, 1969.

[66] K.S. Brentner. A computer program incorporating realistic blade motions and advanced acoustic formulation. NASA TM 87721, 1986.

[67] P.R. Spalart and S.R. Allmaras. One equation turbulence model for aerodynamic flows. *La Recherche Aerospatiale*, 1:5–21, 1994.

[68] P.R. Spalart, W.H. Jou, M. Strelets, and S. Allmaras. Comments on the feasibility of LES for wings and on a hybrid RANS/LES approach. *In 1st AFOSR Int. Conf. on DNS/LES, Aug, 4-8, Huston, LA. In Advances in DNS/LES, C.Liu and Z.Liu, Eds., Greyden Press, Columbus, OH*, 1997.

[69] P.R. Spalart. Trends in turbulence treatments. AIAA Paper 2000-2306, 2000.

[70] J. Forsythe, K. Hoffman, and J.F. Dieteker. Detached-eddy simulation of a supersonic axisymmetric base flow with an unstructured flow solver. AIAA Paper 2000-2410, 2000.

[71] M. Strelets. Detached eddy simulation of massively separated flows. AIAA Paper 2001-0879, 2001.

[72] S.K. Lele. Compact finite difference schemes with spectral like resolution. *Journal of Computational Physics*, 103(11):16–42, 1992.

[73] R. Hixon. A new class of compact schemes. AIAA Paper 98-0367, 1998.

[74] G. Ashcroft and X. Zhang. Optimized prefactored compact schemes. *Journal of Computational Physics*, 190:459–477, 2003.

[75] R. Hixon and E. Turkel. Compact implicit maccormack-type schemes with high accuracy. *Journal of Computational Physics*, 158:51–70, 2000.

[76] R. Hixon. Prefactored small-stencil compact schemes. *Journal of Computational Physics*, 165:522–541, 2000.

[77] F.Q. Hu, M.Y. Hussaini, and J. Manthey. Low dissipation and dispersion Runge-Kutta schemes for computational aeroacoustics. *Journal of Computational Physics*, 124:177–191, 1996.

[78] B. Wasistho, B.J. Guerts, and J.G.M. Kuerten. Simulation technique for spatially evolving instabilitites in compressible flow over a flat plate. *Computers and Fluids*, 26(7):713–740, 1997.

[79] S.K. Richards, X. Zhang, X.X. Chen, and P.A. Nelson. The evaluation of buffer zone as a non-reflecting boundary condition for CAA. *Journal of Sound and Vibration*, 270:539–557, 2004.

[80] K.W. Thompson. Time-dependent boundary conditions for hyperbolic systems. *Journal of Computational Physics*, 68:1–24, 1987.

[81] M.B. Giles. Non-reflecting boundary conditons for euler equation calculations. *AIAA Journal*, 28:2050–2058, 1990.

[82] K. Stewartson. *The Theory of Laminar Boundary Layers in Compressible Fluids*. Oxford Mathematical Monographs, 1964.

[83] L.N. Cattafesta, S. Garg, and M. Choudhari. Active control of flow-induced cavity resonance. AIAA Paper 97-1804, 1997.

[84] T. Colonius. An overview of simulation, modeling and active control of flow/acoustic resonance in open cavities. AIAA Paper 2001-0076, 2001.

[85] D. Rockwell and C. Knisely. Vortex edge interaction: Mechanism for generating low frequency components. *Physics of Fluids*, 23(2):239–240, 1980.

[86] I. Proudman. The generation of noise by isotropic turbulence. *Proceedings of the Royal Society of London*, A 214:119–132, 1952.

[87] G.B. Ashcroft. *Computational and Experimental Investigation into the Aeroacoustics of Low Speed Flows*. PhD Thesis, University of Southampton, 2004.

[88] P. Bissessur, X.X. Chen, and X. Zhang. Numerical investigation of subsonic 2d/3d cavity flows. AIAA Paper 2004-0683, 2003.

[89] M.S. Chong, A.E. Perry, and B.J. Cantwell. A general classification of three-dimensional flow fields. *Topological Fluid Mechanics, Proceedings of the IUTAM Symposium, Cambridge, UK*, 1, 1989.

[90] A.E. Perry and M.S. Chong. *Flow Visualization: Techniques and Examples*. Imperial College Press, 2000.

[91] R.J. Adrian, K.T. Christensen, and Z.C. Liu. Analysis and interpretation of instantaneous turbulent velocity fields. *Experiments in Fluids*, 29:275–290, 2000.

[92] P. Sagaut, E. Labourasse, P. Quéméré, and M. Terracol. Multiscale approaches for unsteady aerodynamics and large eddy simulation. *4th Asian Computational Fluid Dynamics Conference, Mianyang (China), September*, 18-22, 2000.

[93] P.R. Spalart, S. Deck, M.L. Shur, K.D. Squires, M. Strelets, and A. Travin. A new version of detached eddy simulation, resistant to ambiguous grid densities. *Theoretical and Computational Fluid Dynamics*, 3:181–195, 2006.

[94] D.C. Wilcox. *Turbulence Modeling for CFD*. DCW Industries, Inc., California, second edition, 1994.

[95] M.J. Lighthill. On sound generated aerodynamically I. General theory. *Proceedings of the Royal Society of London*, A 211:564–587, 1954.

[96] M.J. Lighthill. On sound generated aerodynamically II. Turbulence as a source of sound. *Proceedings of the Royal Society of London*, A 222:1–32, 1954.

[97] F. Farassat. Theory of noise generation from moving bodies with an application to helicopter rotors. NASA TR R451, 1975.

Appendix A

Equations of Fluid Motion

A.1 Navier-Stokes Equations

The compressible Navier-Stokes equations are the flow governing equations derived from first principles from the conservation laws for mass, momentum and energy. In Cartesian tensor notation the equations for the conservative variables (ρ^*, $\rho^* u_i^*$, $\rho^* e_t^*$) are written as,

$$\begin{aligned}
\frac{\partial \rho^*}{\partial t^*} &= -\frac{\partial(\rho^* u_i^*)}{\partial x_i^*} \\
\frac{\partial(\rho^* u_i^*)}{\partial t^*} &= -\frac{\partial(\rho^* u_i^* u_j^* + p^* \delta_{ij})}{\partial x_j^*} + \frac{\partial \tau_{ij}^*}{\partial x_j^*} \\
\frac{\partial(\rho^* e_t^*)}{\partial t^*} &= -\frac{\partial[(\rho^* e_t^* + p^*) u_j^*]}{\partial x_j^*} - \frac{\partial q_j^*}{\partial x_j^*} + \frac{\partial(u_i^* \tau_{ij}^*)}{\partial x_j^*}
\end{aligned} \tag{A.1}$$

Where the $*$ superscript represents a dimensional quantity and (ρ^*, u_i^*, p^*) are the instantaneous density, velocity and the static pressure respectively. The specific total energy e_t^* is given by

$$e_t^* = e^* + \frac{u_i^* u_i^*}{2} \tag{A.2}$$

where e^* is the specific internal energy. The equations are re-written in non-dimensional terms using the following procedure,

$$\rho = \frac{\rho^*}{\rho_\infty^*}, \;\; u_i = \frac{u_i^*}{a_\infty^*}, \;\; p = \frac{p^*}{\rho_\infty^* a_\infty^{*2}}, \;\; T = \frac{T^*}{T_\infty^*}, \tag{A.3}$$

$$\mu = \frac{\mu^*}{\mu_\infty^*}, \;\; \tau_{ij} = \frac{\tau_{ij}^* L_{ref}}{\mu_\infty^* a_\infty^*}, \;\; x = \frac{x_i^*}{L_{ref}^*}, \;\; t = \frac{t^* a_\infty^*}{L_{ref}^*} \tag{A.4}$$

The subscript ∞ denotes freestream values and L_{ref} is the reference length scale. Thus a_∞^* and μ_∞^* are the freestream speed of sound and the freestream viscosity respectively. From this procedure the Reynolds number based on a reference length scale is

$$Re_{L_{ref}} = \frac{\rho_\infty^* u_\infty^* L_{ref}^*}{\mu_\infty^*} \tag{A.5}$$

The fluid is assumed to be a perfect gas (Newtonian fluid) obeying the equation of state $p^* = \rho^* R^* T^*$, or non-dimensionally, $p = (\gamma - 1)\rho e$. In non-dimensional form, the conservation equations are written as

$$\frac{\partial \rho}{\partial t} = -\frac{\partial (\rho u_i)}{\partial x_i} \tag{A.6}$$

$$\frac{\partial (\rho u_i)}{\partial t} = -\frac{\partial (\rho u_i u_j + p\delta_{ij})}{\partial x_j} + \frac{\partial \tau_{ij}}{\partial x_j} \tag{A.7}$$

$$\frac{\partial (\rho e_t)}{\partial t} = -\frac{\partial [(\rho e_t + p) u_j]}{\partial x_j} - \frac{\partial q_j}{\partial x_j} + \frac{\partial (u_i \tau_{ij})}{\partial x_j} \tag{A.8}$$

Since the fluid is assumed to be Newtonian, the constitutive relation for the stress tensor is

$$\tau_{ij} = \frac{M_\infty}{Re_{L_{ref}}} \left[\mu \left(\frac{\partial u_i}{\partial x_j} + \frac{\partial u_j}{\partial x_i} \right) + \mu_B \frac{\partial u_k}{\partial x_k} \delta_{ij} \right], \tag{A.9}$$

where μ is the molecular viscosity and μ_B is the bulk viscosity and $\mu_B = -\frac{2}{3}\mu$. The heat flux vector q_i is obtained using Fourier's law for heat conduction $q_j^* = -k^* \partial T^* / \partial x_j$, with k^* being the thermal conductivity. In non-dimensional form,

$$q_j = -\frac{1}{\gamma - 1} \frac{M_\infty}{Re_{L_{ref}}} \frac{\mu}{Pr_L} \left(\frac{\partial T}{\partial x_j} \right), \tag{A.10}$$

Where Pr_L is the laminar Prandtl number ($Pr_L = c_p^* \mu_\infty^* / k^*$), and is taken as 0.72.

The viscosity is assumed to follow Sutherland's law,

$$\mu^* = C_1 \frac{T^{*3/2}}{T^* + C_2} \tag{A.11}$$

where C_1 and C_2 are constants for a given gas. For air, they are $1.456 \times 10^{-6} kg/(ms\sqrt{K})$ and $110.4K$ respectively.

A.2 Reynolds Averaging and Favre Averaging

This category of statistical modelling proposed by Reynolds in 1880 is based on a decomposition of turbulent flow quantities into the mean and the fluctuating parts. Denoting a particular field quantity by ϕ, the flow properties are decomposed as:

$$\phi = \overline{\phi} + \phi' \tag{A.12}$$

In equation (A.12), $\overline{\phi}$ is the time averaged field and ϕ' is the fluctuation about the mean. For incompressible flows this averaging procedure is directly applied to the Navier Stokes

equation, but to avoid the appearance of source terms in the averaged continuity equation, Favre averaging is introduced by which the mean is weighed by the density:

$$\tilde{\phi} = \frac{\overline{\rho\phi}}{\overline{\rho}} \tag{A.13}$$

and

$$\phi = \tilde{\phi},\ \overline{\phi'} \neq 0,\ \overline{\rho\phi'} = 0 \tag{A.14}$$

This enables the Favre averaged equations for both compressible and incompressible flows to be written in the same form, defining:

$$\rho = \overline{\rho} + \rho',\ \overline{\rho'} = 0,\ p = \overline{p} + p',\ \overline{p'} = 0,$$

$$u_i = \tilde{u}_i + u_i',\ \overline{\rho u_i'} = 0,\ i = 1,2,3$$

$$e_t = \tilde{e}_t + e_t',\ \overline{\rho e_t'} = 0;\ T = \tilde{T} + T';\ \overline{\rho T'} = 0$$

using the ergodicity hypothesis, the temporal mean is defined as

$$\overline{\phi} = \frac{1}{T}\int_{t_0}^{t_0+T} \phi dt \tag{A.15}$$

where T is a time scale which is much larger than the smallest time scale of the flow. The fluctuating part has the important property of $\overline{\rho\phi'} = 0$, but for non linear terms $\overline{\rho\phi'\psi'} \neq 0$.

A.2.1 Averaged equations of motion

The application of the averaging procedure to equations (A.1) gives a similar system. However,in the viscous stress tensors we have extra terms called the Reynolds stress tensor which arises due to the nonlinear interactions in the convective terms of the Navier-Stokes equations;

$$Reynolds\ Stresses = -\overline{\rho u_i' u_j'} \tag{A.16}$$

This is a symmetric tensor and its trace is equal to the turbulent kinetic energy, i.e. $\tilde{k} = \frac{1}{2}\overline{u_i' u_i'}$. Here lies the fundamental problem of turbulence modeling in which there is a need to model the Reynolds stresses accurately. Note also that the Reynolds stresses appear only in the viscous stress terms in the averaged Navier Stokes equations. More details of what has been outlined above can be found in the book by Wilcox [94]. There are various ways to model the averaged equations and these classify in the broad topic of RANS modeling. Typical turbulence models can be categorized as:

- Algebraic models
- One equation models
- Two equation models
- Reynolds Stress models (RSM)

However, it is beyond the scope of this present study to detail all the possible turbulence models available, for this purpose the reader should consult [94]. One equation models based on the transport of the turbulent kinetic energy are incomplete as a length scale needs to be prescribed. On the other hand, one equation and two equation models in which the eddy viscosity transport equation is solved are termed as complete as the length scale is self prescribed.

Appendix B

Code Description and Parallel Implementation

The code for solving the various transport equations detailed in Chapter 2 was developed in the Fortran 90 programming language. A modular approach was employed in the development of the viscous flow solver. For instance, each spatial difference scheme was self-contained within a complete subroutine. Similarly, boundary conditions were developed in a modular fashion. The turbulence model can be switched on at will before the execution of the code. However, a 'zonal' modeling capability, where specific laminar/turbulent regions can be imposed, has not yet been implemented. Various other numerical parameters, such as numerical filters and number of time steps, can be specified in the input file.

To solve problems which invariably require a large number of grid points, a multi-block domain decomposition method was employed to facilitate 'parallelisation' of the numerical computation. The Message Passing Interface (MPI) libraries were used to 'parallelise' the code. MPI is a portable collection of libraries to promote the development of programs for parallel applications. Using this approach, large computational efforts are shared among a number of processors, where the load would ideally be evenly distributed across the platform.

The computational blocks are evenly allocated to the number of processors that is required to execute the code. An example of a parallel multi-block formulation that is representative of the one employed in the code is shown in Figure B.1. In this schematic, the domain is divided into four blocks and distributed over four processors. In the distributed memory machines employed in the current work, memory is allocated for each block only on the processor to which it has been assigned. For the multi-block formulation, block interface information is necessary for the spatial derivatives to be continuous. Therefore, the 'ghost cells' of say Block 1 will contain data from its neighbor, Block 2 and vice-versa. The information transfer is performed using the appropriate MPI function call. Such a procedure is repeated across the entire domain wherever a block interface is encountered (e.g. between Block 2 and Block 3 and between Block 2 and Block 4).

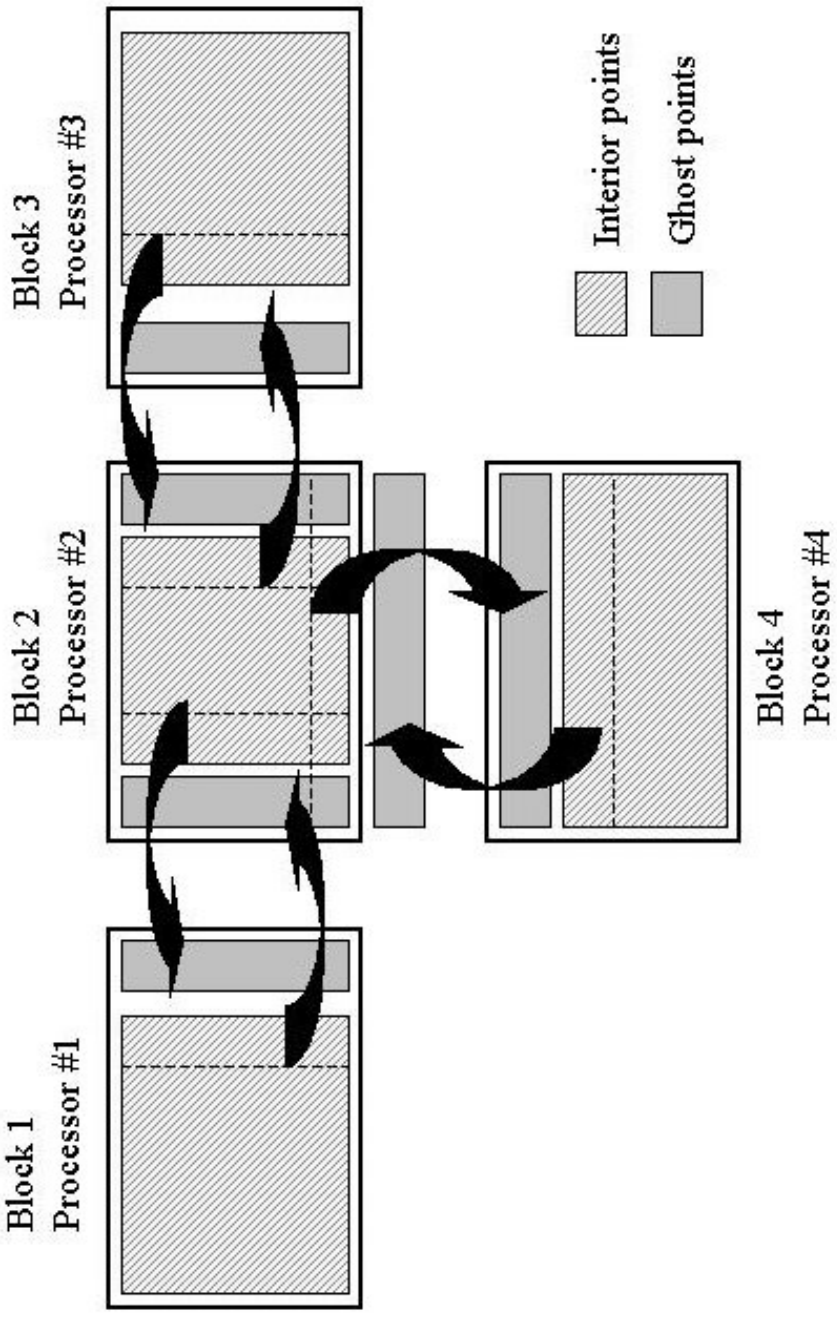

Figure B.1: Multi-block domain decomposition.

Appendix C

Ffowcs Williams and Hawkings Acoustic Analogy

C.1 Overview

This appendix presents the theoretical formulation and the numerical implementation of the Ffowcs-Williams and Hawkings (FW-H) acoustic analogy for the calculation of the acoustic fields at an arbitrary far field observer positions.

C.2 The Analogy

The Ffowcs Williams and Hawkings equation [65] is an exact formulation for the computation of the acoustic field when solid boundaries and a uniform freestream velocity play a direct role in the generation and propagation of sound. It is obtained through a re-arrangement of the Navier-Stokes equations. It is in fact a generalization of Lighthill's acoustic analogy [95, 96], to incorporate the effect of solid boundaries and of acoustic source motion in an aerodynamic field. The solution of the FW-H equation is obtained

through the integration of volume and surface source terms and it can be used to predict far field acoustic signals based on near field aerodynamic data. The method is typically applied with the integration surface coincident with the solid boundaries, but it can also be applied off solid boundaries, provided the integration surface is permeable.

C.3 The FW-H Equation

The FW-H equation is derived by embedding the exterior flow problem in unbounded space by using generalized functions to describe the flow field. Consider a moving body, whose surface S is described by $f_s(\mathbf{x},t) = 0$. The surface $f_s = 0$ is defined such that $\nabla f_s = \hat{n}_i$, where $\hat{n}_i$ is a unit normal to the surface pointing into the fluid. Inside $f_s = 0$, the generalized flow variables are defined as having free-stream values. Thus for $f_s < 0$, the flow variables are $(p = p_0, \rho = \rho_0, u_i = 0)$. Thus the governing equations of fluid motion are now valid for all space through the use of the Heaviside function $H(f_s)$. Using the Lighthill approach, an inhomogeneous wave equation valid through all space is obtained. In differential form, the FW-H equation may be written as

$$\left(\frac{1}{c_0^2}\frac{\partial^2}{\partial t^2} - \frac{\partial^2}{\partial x_i^2}\right)\left(c_0^2(\rho-\rho_0)H(f_s)\right) = \frac{\partial^2}{\partial x_i \partial x_j}\left(T_{ij}H(f_s)\right) - \frac{\partial}{\partial x_i}\left(L_i\delta(f_s)\right) + \frac{\partial}{\partial t}\left(U_n\delta(f_s)\right) \tag{C.1}$$

where the source terms are expressed as

$$T_{ij} = \rho u_i u_j - \tau_{ij} + [(p-p_0) - c_0^2(\rho-\rho_0)]\delta_{ij} \tag{C.2}$$

$$L_i = L_{ij}\hat{n}_j = [\rho u_i(u_j - v_j) + p'_{ij}]\hat{n}_j \tag{C.3}$$

$$U_n = U_i\hat{n}_i = [\rho(u_i - v_i) + \rho_0 v_i]\hat{n}_i \tag{C.4}$$

The three source terms have a physical meaning, which is helpful in understanding the noise generation. The quadrupole source term (C.2) accounts for non linear effects such

as variation in local sound speed, vorticity and turbulence. This term is also known as the Lighthill stress tensor. The loading noise (surface dipole) in Equation (C.3) is related to the forces that act on the fluid as a result of the presence of the body. The first term of Equation (C.3) relates to the flux of momentum across the surface S, while the second term $p'_{ij} = (p - p_o)\delta_{ij} - \tau_{ij}$ is the force per unit area applied over S . The thickness noise (monopole) in Equation (C.4) is a consequence of both the geometry of the body and the flow on it. The monopole term is composed of two components, namely, the mass flux through the surface, while the the second is equivalent to the mass flux due to the surface motion.

C.4 Retarded Time Formulation

Away from the source region, Equation (C.1) reduces to the homogeneous wave equation and the term $c_0^2(\rho - \rho_0)$ becomes the acoustic pressure. An integral formulation expressing the solution of Equation (C.1) may be obtained by employing a Green's function $G(\mathbf{x},t|\mathbf{y},\tau)$ which satisfies the following equation

$$\left(\frac{1}{c_0^2}\frac{\partial^2}{\partial t^2} - \frac{\partial^2}{\partial x_i^2}\right) G(\mathbf{x},t|\mathbf{y},\tau) = \delta(\mathbf{x}-\mathbf{y})\delta(t-\tau) \tag{C.5}$$

for an impulsive point source. The Green's function $G(\mathbf{x},t|\mathbf{y},\tau)$ may be thought of as representing the response at $\mathbf{x}$ and time t due to an impulsive forcing at the point $\mathbf{y}$ and time τ. The solution is formed by multiplying Equation (C.5) by the right hand side of Equation (C.1) at point $\mathbf{y}$ and time τ and integrating over all space and time, including the volume exterior to S. Exploiting the sifting property of the Dirac delta functions in Equation (C.5), an integral equation for the acoustic pressure p' at time t and position $\mathbf{x}$ may be written

$$p'(\mathbf{x},t) = \int_{-\infty}^{\infty}\int_{V}\left[G\frac{\partial^2}{\partial y_i \partial y_j}\left(T_{ij}H(f_s)\right)\right]dV(\mathbf{y})d\tau$$
$$-\int_{-\infty}^{\infty}\int_{V}\left[G\frac{\partial}{\partial y_i}\left(L_i\delta(f_s)\right) - G\frac{\partial}{\partial \tau}\left(U_n\delta(f_s)\right)\right]dV(\mathbf{y})d\tau \tag{C.6}$$

Assuming the volume sources are limited to a finite region of space, the spatial and temporal derivatives may be moved from the source terms to the Green's function using partial integration to obtain

$$p'(\mathbf{x},t) = \int_{-\infty}^{\infty}\int_{V(\tau)} T_{ij}\frac{\partial^2 G}{\partial y_i \partial y_j}dV(\mathbf{y})d\tau + \int_{-\infty}^{\infty}\int_{S(\tau)} L_i\frac{\partial G}{\partial y_i}dS(\mathbf{y})d\tau$$
$$-\int_{-\infty}^{\infty}\int_{S(\tau)} U_n\frac{\partial G}{\partial \tau}dS(\mathbf{y})d\tau \tag{C.7}$$

where the properties of the Heaviside function have been used to limit the first volume integral to the region external to S, and the shifting property of the Dirac delta functions has been used to reduce the remaining volume integrals to the surface integrals. Equation (C.7) is the fundamental equation governing the generation of sound in the presence of solid boundaries and uniform freestream convection. It is exact and applies to any region which is bounded by the permeable surfaces in arbitrary motion. When the right hand side of this equation is known, the pressure fluctuations in the sound field can be calculated. Substitution of a Green's function appropriate to the particular problem considered completes the solution. The three-dimensional free space Green's function is defined as

$$G_0(\mathbf{x},t|\mathbf{y},\tau) = \frac{\delta(g)}{4\pi r} \tag{C.8}$$

where $g = \tau - t + r/c_0$ and $r = |\mathbf{x}-\mathbf{y}|$ is the distance between the observer and source. To obtain the specific formulation of the FW-H equation implemented numerically (see

Ashcroft [87]), first recall the elementary properties of the free space Green's function

$$\frac{\partial G_0}{\partial t} = -\frac{\partial G_0}{\partial \tau} \quad and \quad \frac{\partial G_0}{\partial x_i} = -\frac{\partial G_0}{\partial y_i}$$

Using these properties the spatial and temporal derivatives of G_0 with respect to source coordinate $\mathbf{y}$ and time τ are replaced by the derivatives with respect to the observer coordinates $\mathbf{x}$ and time t. Then, as the integration is performed on the source coordinate $\mathbf{y}$ and time τ, the spatial and temporal derivatives may be moved out of the integrals to obtain

$$p'(\mathbf{x},t) = \frac{\partial^2}{\partial x_i \partial x_j}\int_{-\infty}^{\infty}\int_{V(\tau)} T_{ij}\frac{\delta(g)}{4\pi r}dV(\mathbf{y})d\tau + \frac{1}{c_o}\frac{\partial}{\partial t}\int_{-\infty}^{\infty}\int_{S(\tau)} L_i\hat{r}_i\frac{\delta(g)}{4\pi r}dS(\mathbf{y})d\tau + \int_{-\infty}^{\infty}\int_{S(\tau)} L_i\hat{r}_i\frac{\delta(g)}{4\pi r^2}dS(\mathbf{y})d\tau + \int_{-\infty}^{\infty}\int_{S(\tau)} U_n\frac{\delta(g)}{4\pi r}dS(\mathbf{y})d\tau \quad \text{(C.9)}$$

where the identity [97]

$$\frac{\partial}{\partial x_i}\left(\frac{\delta(g)}{4\pi r}\right) = -\frac{1}{c_o}\frac{\partial}{\partial t}\left(\frac{\hat{r}_i\delta(g)}{4\pi r}\right) - \frac{\hat{r}_i\delta(g)}{4\pi r} \quad \text{(C.10)}$$

has been used to eliminate the spatial derivative in the second source term. To evaluate the integrals over the delta functions it is convenient to introduce a coordinate system in which the surface $S(\tau)$ is stationary. In general, the surface may move arbitrarily and it would be appropriate to introduce a Lagrangian coordinate $\zeta_L(\mathbf{y},\tau)$. However here, the surface is rigid and only a Cartesian coordinate that simply translated with velocity $\mathbf{U_s}$ is considered. The Jacobian of the transformation between the two Cartesian coordinates is taken to be unity, as is the ratio of the area elements $dS(\zeta_L)/dS(\mathbf{y})$. In the translating coordinate system ζ_L the volume and surface integrals are independent of τ. Therefore, the order of integration may be interchanged and the integration with respect to τ can be

carried out to obtain the FW-H equation in source fixed coordinates

$$p'(\mathbf{x},t) = \frac{\partial^2}{\partial x_i \partial x_j}\int_V \left[\frac{T_{ij}}{r|1-M_r|}\right]_{\tau^*} dV(\zeta_L) + \int_S \left[\frac{L_r}{r^2|1-M_r|}\right]_{\tau^*} dS(\zeta_L) + \frac{1}{c_o}\frac{\partial}{\partial t}\int_S \left[\frac{U_n + L_r}{r|1-M_r|}\right]_{\tau^*} dS(\zeta_L) \tag{C.11}$$

where $M_r = M_i r_i$ is the projection of the local surface Mach number $M_i = v_i/c_o$ in the radiation direction, $L_r = L_i \hat{r}_i$, and the notation $\left[\ \right]_{\tau^*}$ indicates the quantity enclosed within the brackets is to be evaluated at position ζ_L and the retarded time $\tau^* = t - |\mathbf{x} - \mathbf{y}(\zeta_L, \tau^*)|/c_o$. To complete the derivation, note that as $r = |\mathbf{x} - \mathbf{y}(\zeta_L, \tau)|$ is a function of τ, the relation for retarded time $g = \tau - t + r/c_o$ may also be used to show

$$\left.\frac{\partial}{\partial t}\right|_{\mathbf{x}} = \left[\frac{1}{1-M_r}\left.\frac{\partial}{\partial \tau}\right|_{\mathbf{x}}\right] \tag{C.12}$$

which enables the time derivative to be taken inside the final integral, and evaluated analytically to obtain

$$\begin{aligned} p'(\mathbf{x},t) = {} & \frac{\partial^2}{\partial x_i \partial x_j}\int_V \left[\frac{T_{ij}}{r|1-M_r|}\right]_{\tau^*} dV(\zeta_L) + \int_S \left[\frac{\dot{U}_n + U_{\dot{n}}}{r(1-M_r)^2}\right]_{\tau^*} dS(\zeta_L) \\ & + \frac{1}{c_o}\int_S \left[\frac{\dot{L}_r}{r(1-M_r)^2}\right]_{\tau^*} dS(\zeta_L) + \int_S \left[\frac{L_r - L_M}{r^2(1-M_r)^2}\right]_{\tau^*} dS(\zeta_L) \\ & + \frac{1}{c_o}\int_S \left[\frac{L_r(r\dot{M}_r + c_o M_r - c_o M^2)}{r^2(1-M_r)^3}\right]_{\tau^*} dS(\zeta_L) \\ & + \int_S \left[\frac{U_n(r\dot{M}_r + c_o M_r - c_o M^2)}{r^2(1-M_r)^3}\right]_{\tau^*} dS(\zeta_L) \end{aligned} \tag{C.13}$$

where a dot indicates differentiation with respect to τ. Equation (C.13), with the volume quadrupole term neglected, is known as formulation 1A of Farassat [66]. Apart from the neglection of the quadrupole term, this equation is exact and therefore valid both in the near and far field. The method is generally called the retarded time method. The far field

acoustic pressure is evaluated at a particular time t (reception time) through the summation of all the perturbations reaching the observer at the reception time t. These perturbations are emitted at different retarded times to reach the same reception time. As the method uses data at all time levels in one calculation, time records of perturbations have to be stored for post-processing. For non-periodic flow phenomena, this method requires a long time history and therefore large storage space. For the numerical implementation of the method, see Ashcroft [87].